Experimental and numerical CPFEM-based determination of FLD using biaxial and Nakajima tests: industrial application to deep drawing simulation for FCC and BCC metals

Mohammad Mianroodi

UNIVERSITE DE STRASBOURG

École Doctorale 269 Mathématiques, Sciences de l'Information et de l'Ingénieur

THÈSE

Présentée par :

Mohammad MIANROODI

Soutenue le :02/12/2021

Pour l'obtention du grade de **Docteur de l'Université de Strasbourg**

Spécialité : Mécanique des Matériaux

Experimental and numerical CPFEM-based determination of FLD using biaxial and Nakajima tests: industrial application to deep drawing simulation for FCC and BCC metals

Membres du Jury:

Directeur de thèse:	Dr. Siham TOUCHAL, Université de Strasbourg
Co-encadrant :	Dr. Guillaume ALTMEYER, Université de Tours
Rapporteur externe:	Pr. Stéphane MEO, Université de Tours
Rapporteur externe:	Dr. Rodrigue MATADI-BOUMBIMBA, Université de Lorraine
Examinateur externe:	Pr. Hamid GARMESTANI, Georgia Institute of Technology, Atlanta, USA
Examinateur interne:	Pr. Said AHZI, Université de Strasbourg
Invité :	Dr. Majid BANNIASADI, Université de Téhéran, Iran
Invité :	M. Nooraldin BANAEINEJAD, CanHood Home Appliances company, Téhéran, Iran

To my parents,

To my love

Résumé

Cette thèse porte sur la détermination expérimentale et numérique des Courbes Limites Formage (CLF). Les matériaux utilisés sont l'alliage d'aluminium Al6061 (CFC) et l'acier doux St14 (CC). Un modèle de type Marciniak and Kuczynski (1967) est utilisé pour obtenir les CLF à la fois expérimentalement et numériquement en utilisant deux types de tests.
La première approche est basée sur la simulation EF d'un test biaxial où la tôle comporte un défaut initial, une réduction d'épaisseur de type Marciniak and Kuczynski (M-K). La seconde approche est basée sur la modélisation EF de l'essai Nakajima. Dans cet essai, plusieurs éprouvettes de largeur différentes sont utilisées pour reproduire plusieurs trajets de déformation afin d'obtenir une CLF complète. Les CLF obtenues permettent ensuite l'étude d'une application industrielle : l'emboutissage des tôles minces. Un modèle de type CPFEM est également implémenté dans le code Abaqus et appliqué aux tests biaxiaux avec un défaut initial de type M-K. Les simulations montrent que les textures prédites dépendent à la fois du trajet de déformations, de la structure cristallographique ainsi que de la localisation dans la tôle (zone saine vs zone défectueuse).
Afin de valider le travail numérique, une partie expérimentale a été réalisée durant ce travail de thèse en Iran, dans l'entreprise partenaire, CanHood et à l'université des Sciences et Technologie d'Iran. Les essais expérimentaux réalisés sont des essais de traction uniaxiale, des essais biaxiaux ainsi que des essais Nakajima. Une méthode de corrélation d'images numérique est utilisée pour la mesure des déformations. Les textures expérimentales sont mesurées à l'aide la méthode de diffraction aux rayons X pour plusieurs trajets de déformations.
Finalement, les résultats expérimentaux sont en accord avec les résultats numériques et la littérature pour les deux matériaux étudiés.

Abstract

This thesis deals with the numerical and experimental determination of Forming Limit Diagram (FLD) for FCC (Aluminum Al6106) and BCC (St14 mild steel) materials. A Marciniak and Kuczynski (1967) model is used to obtain the FLD using two kinds of tests.
The first one is based on the Marciniak-Kuczynski (M-K) model implemented in a FEM modeling of biaxial test including an initial band with reduced thickness. The second approach is based on a FEM simulation of the Nakajima test. In the Nakajima test, different strain paths can be obtained by stretching different width size specimens in order to build complete FLD. The predicted FLD is then applied to an industrial case: the deep drawing simulation. CPFEM simulation for the M-K biaxial traction test is also performed. Simulations show that the predicted textures depend on the crystallographic structures, strain path and the localization in the metal sheet (safe zone versus defect zone).
Several experimental tests were conducted in order to validate the predicted numerical results in Iran (CanHood Home Appliances Company and University of Tehran). Uniaxial, biaxial and Nakajima tests for FCC and BCC are done. The DIC technique is used for strain measurement. The development of crystallographic texture evolution during the tests is captured with XRD technique for several strain paths.
A relative good correlation between literature, numerical and experimental tests for FCC and BCC materials is obtained.

Acknowledgment

First of all, I would like to express my gratitude and appreciation to my supervisor, Dr. Siham TOUCHAL, who guided me throughout this project. She supported me every moment of this long way.

A very special thank you to Dr. Guillaume Altmeyer for his advice and for helping to find the best way to continue my research way in this subject.

I would like to thank the jury members of my thesis for participating in my defense.

I would like to acknowledge my colleagues from the Icube laboratory for their superb collaboration, friendship and support during my research career.

I would also like to thank my friends who supported me and offered deep insight into the study.

I would also like to thank CanHood Home Appliances company for funding my thesis. I'd like to especially thank Dr. Hashemi, Iran University of Science and Technology, and the University of Tehran for their collaboration.

In addition, I would like to thank my parents for their consultation. You are always behind me to encourage me in this career.

Finally, I would like to thank my partner Sahar for her energy, her patience and her love. The words are not enough for her.

Publications and scientific contributions:

[Journal] Mianroodi, Mohammad, Altmeyer, Guillaume, Touchal, Siham
Experimental and numerical FEM-based determinations of forming limit diagrams of St14 mild steel based on Marciniak-Kuczynski model, Journal of Mechanical Engineering and Sciences, Vol. 13, pp. 5818-5831, 2019.
DOI: 10.15282/jmes.13.4.2019.08.0464

[Conference] Mianroodi, Mohammad, Touchal, Siham, Altmeyer, Guillaume
Comparison of Forming Limit Diagrams for FCC and BCC materials using Taylor and Marciniak-Kuczynski models, International conference with proceedings ICSET 2019 International conference on science, engineering & Technology, Toronto, Canada, February 2019.

[Conference] Altmeyer, Guillaume, Touchal, Siham, Mianroodi, Mohammad
Coupling of micromechanical phi-model and plastic instability Marciniak-Kuczynski model for Forming Limit Diagrams predictions, 3rd International conference on computational plasticity, Barcelona, September 2017.

[Conference] Mianroodi, Mohammad, Touchal, Siham, Altmeyer, Guillaume
Numerical Prediction of Forming Limit Diagrams using Marciniak-Kuczynski instabilities criteria and texture evaluation of roll forming process, International congress of interdisciplinary studies in science and engineering, Tehran, Iran, July 2017.

[Conference] Touchal, Siham, Mianroodi, Mohammad, Altmeyer, Guillaume, Ahzi, Said
Prediction of Forming Limit Diagrams using the phi-model and the Marciniak-Kuczynski model, First International Conference and Workshop on Mechanical Engineering Research Research Trends in Mechanical Engineering 2016, RTME 2016, University of Aveiro, Portugal, 11-13 July 2016.

[Poster] Numerical simulation of sheet metal forming processes for polycrystalline materials withM-K approach, Journée de la mécanique, France, 2017.

[Poster] Micromechanical modeling of polycrystalline materials Application to sheet metal forming processes, Journée doctorale MSII, France, 2016.

Plan

Introduction

Les opérations de mise en forme par déformation plastique sont très répandues dans l'industrie métallurgique. Ces opérations sont limitées par l'apparition de défauts tels que la striction diffuse ou localisée. Les Courbes Limites Formage (**CLF**) restent très populaires et encore largement utilisées pour définir la formabilité des tôles métalliques. Cette thèse porte donc sur la détermination expérimentale et numérique des CLF. Les matériaux utilisés dans ce travail sont l'alliage d'aluminium Al6061 (CFC) et l'acier doux St14 (CC). Un modèle de type Marciniak and Kuczynski (1967) est utilisé pour obtenir les CLF à la fois expérimentalement et numériquement en utilisant deux types de tests :

- **Détermination numérique des CLF en utilisant un test biaxial**

La première approche est basée sur la simulation Eléments-Finis (EF) d'un test biaxial où la tôle comporte un défaut initial, une réduction d'épaisseur de type Marciniak and Kuczynski (M-K), voir figure 1.

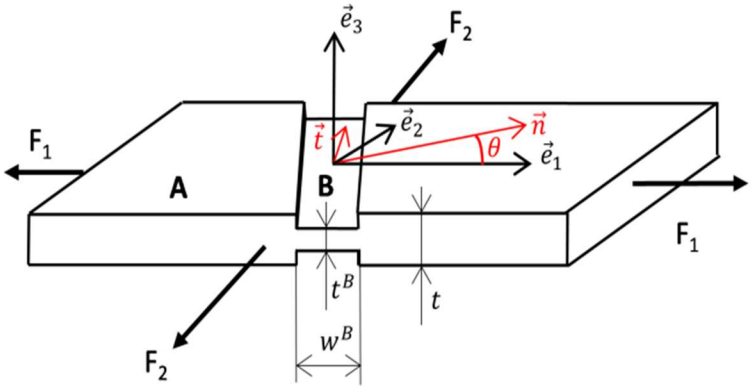

Figure 1. Modèle multizone de Marciniak and Kuczynski

Durant le chargement, une localisation de la déformation va se produire dans la bande d'épaisseur réduite (Zone B). Dans le modèle M-K, le paramètre $f_0 = t^B/t$ traduit cette réduction d'épaisseur entre la zone A (zone saine) et la zone B (zone défectueuse). Des simulations EF sont réalisées sur des tôles de 180x180 mm avec une épaisseur de 1 mm en concordance avec les essais

expérimentaux. Ces tôles présentent un défaut de type réduction d'épaisseur. Les tôles sont sollicitées en traction biaxiale avec 11 valeurs pour le rapport $\alpha = F_2/F_1$ (entre 0 et 1) (voir figure 1). Une étude paramétrique portant sur l'influence du rapport des épaisseurs f_0 (0.90, 0.95 and 0.99) ainsi que de la valeur de l'orientation de l'angle θ (0°, 20°, 40°) de la bande défectueuse sur les CLF est réalisée, voir figures 2 et 3.

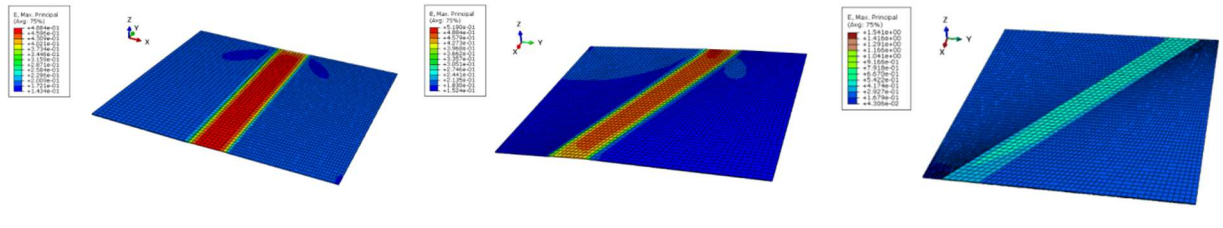

a) **b)** **c)**

Figure 2. Déformation principale maxi pour l'acier doux St14 (α=0.5, f0=0.90)

(a) θ = 0°, (b) θ =20°, (c) θ =40°

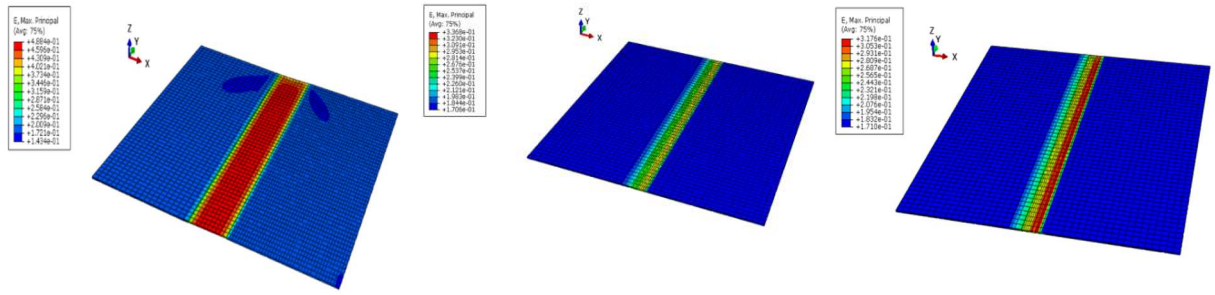

a) **(b)** **(c)**

Figure 3. Déformation principale maxi pour l'acier doux St14 (α=0.5, θ = 0°)
(a) f0=0.90 , (b) f0=0.95 (c) f0=0.99

Une analyse de la valeur des déformations dans la zone A et la zone B permet l'obtention des CLF en utilisant un critère basé sur les déformations dans l'épaisseur selon le critère $S_{MK} = \epsilon_{33}^{A}/\epsilon_{33}^{B}$ (Evangelista et al. 2002). Lorsque S_{MK} atteint une valeur prédéfinie, les simulations sont stoppées et les déformations extraites permettent la construction des CLF, voir figure 4.

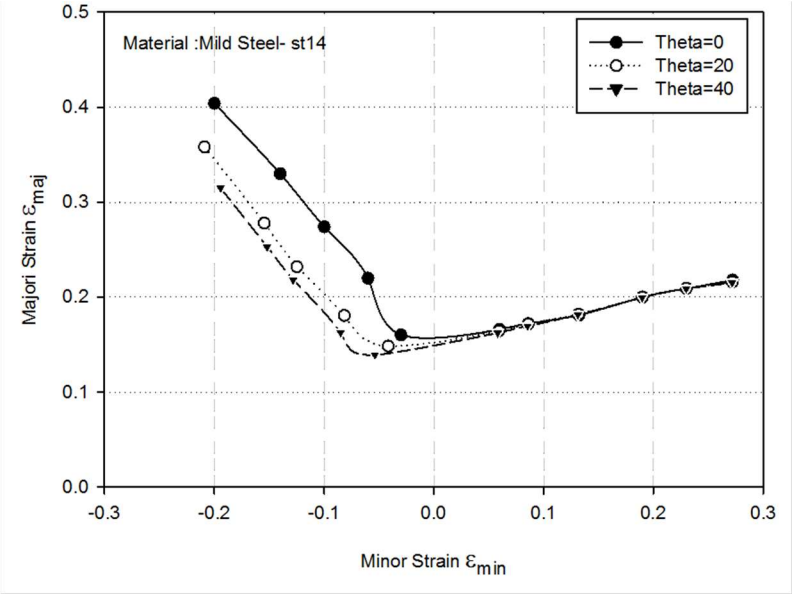

Figure 4. CLF prédites par EF, essai de traction biaxial pour l'acier doux St14

- **<u>Détermination numérique des CLF en utilisant l'essai Nakajima</u>**

La seconde approche utilisée pour déterminer les CLF est basée sur la modélisation EF de l'essai Nakajima, voir Figure 5. Dans cet essai, plusieurs éprouvettes de largeur différentes sont utilisées pour reproduire plusieurs trajets de déformation afin d'obtenir une CLF complète, voir figure 6. L'option de type M-K « damage factor » disponible sous Abaqus est utilisée pour la construction des CLF.

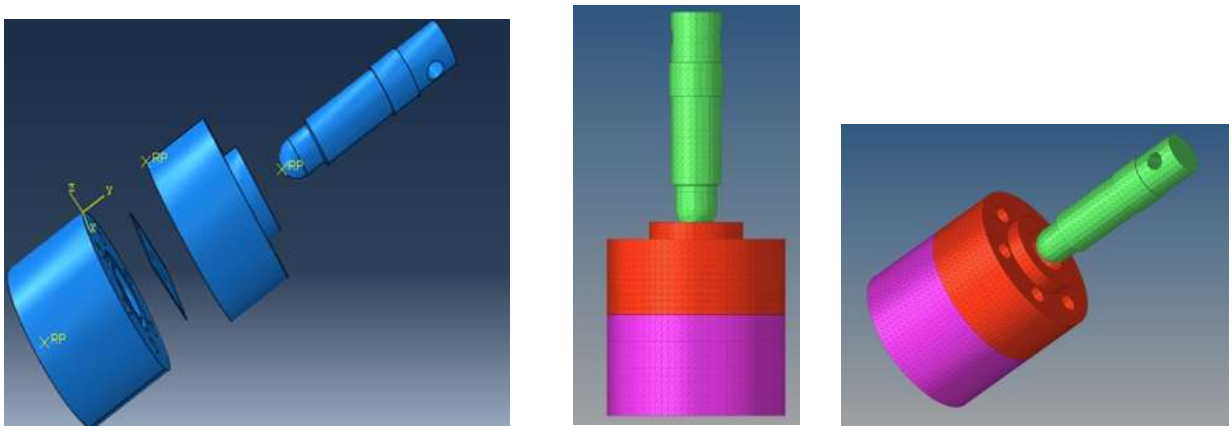

Figure 5. Modèle EF de l'essai Nakajima

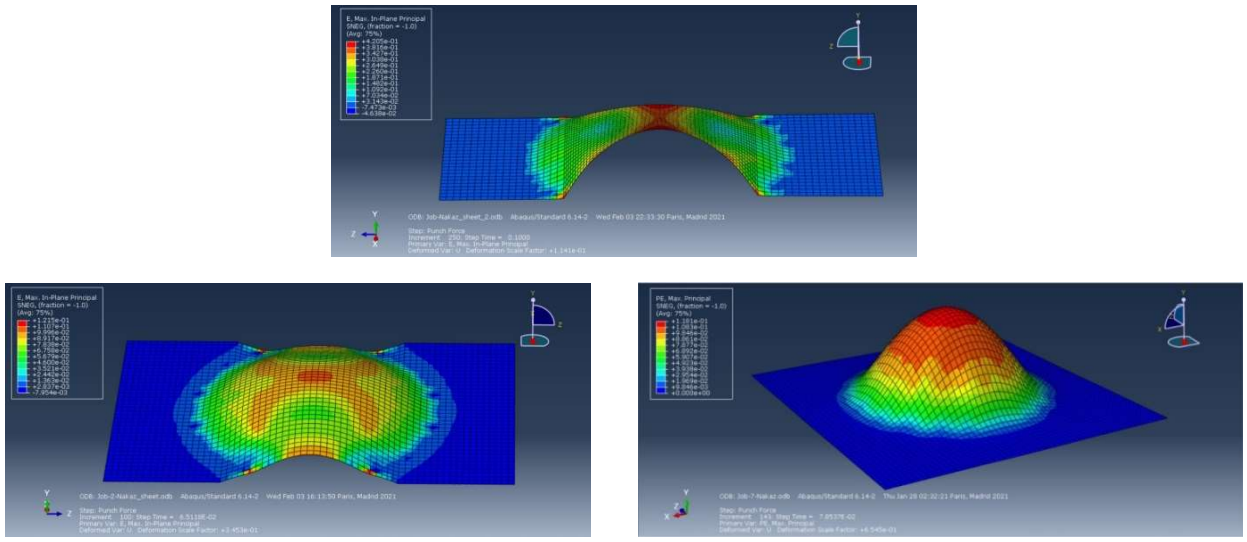

Figure 6. Distribution de la déformation, essai Nakajima, acier doux St14

Nous montrons que la formabilité de l'acier doux est supérieure à la formabilité de l'alliage d'aluminium, ce qui est en accord avec la littérature (Motamedi et al., 2017). Les CLF obtenues permettent ensuite l'étude d'une application industrielle très répandue : l'emboutissage des tôles minces (voir Figure7).

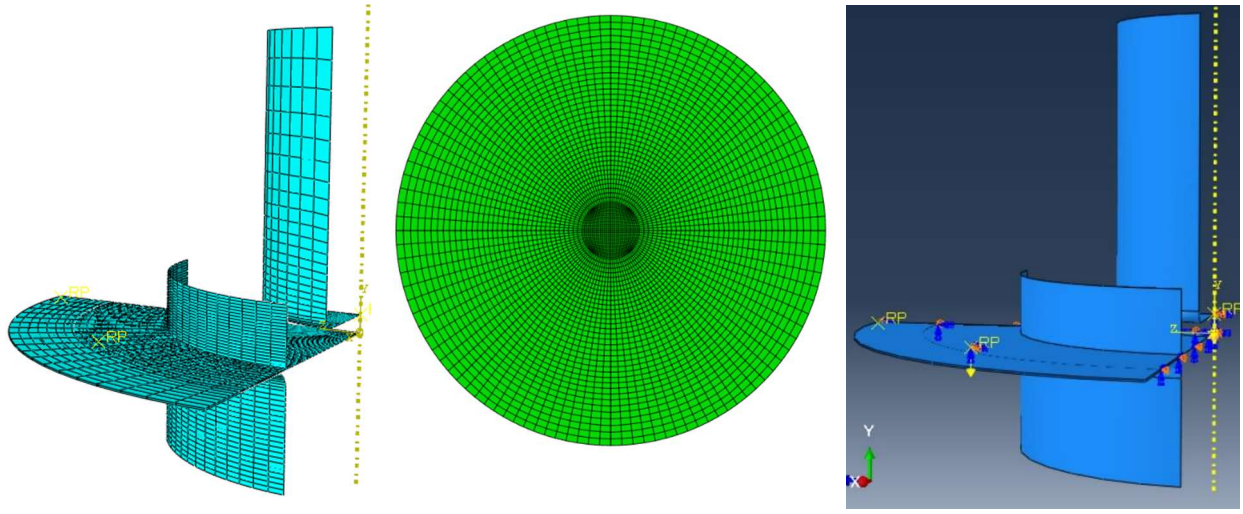

(a) maillage des outils (b) maillage de la tôle (c) conditions aux limites

Figure 7. Modèle EF - emboutissage des tôles minces

- **<u>CPFEM simulation de l'essai biaxial avec un défaut initial de type M-K</u>**

Puisque une déformation plastique induit une modification de la microstructure des métaux, dans cette thèse, une analyse de l'évolution des textures cristallographiques est réalisée pour les tests biaxiaux avec un défaut initial de type M-K. Un modèle de type CPFEM est implémenté dans le code Abaqus. Il utilise le modèle de plasticité des cristaux de Taylor. Le but est d'améliorer les prédictions des CLF.

Les textures prédites sont analysées en considérant différents trajets de déformation, deux structures cristallographiques (CFC et CC). Les simulations montrent que les textures prédites dépendent à la fois du trajet de déformations, de la structure cristallographique ainsi que de la localisation dans la tôle (zone saine vs zone défectueuse). Pour l'acier doux, la figure 8 représente les textures prédites pour l'acier doux St14.

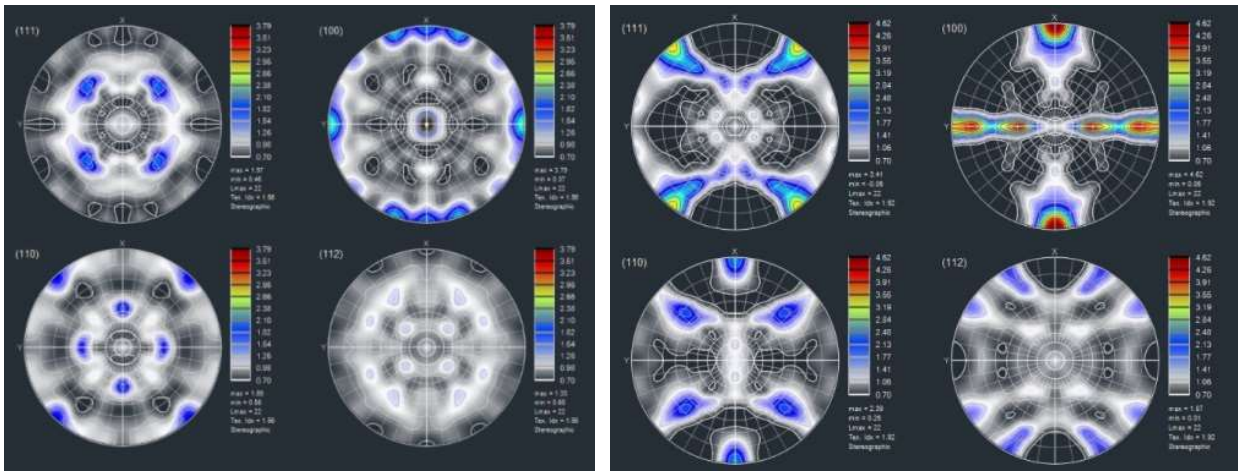

a) **b)**

Figure 8. Pole figures pour l'essai biaxial, $\alpha = F_2/F_1 = 0.9$
(a) Zone A, (b) Zone B, acier doux St14

- **<u>Partie expérimentale et validation</u>**

Afin de valider le travail numérique, une partie expérimentale a été réalisée durant ce travail de thèse. Tous les essais ont été réalisés en Iran, soit dans l'entreprise partenaire, CANHOOD ou bien à l'université des Sciences et Technologie d'Iran (University of Science and Technology).

Les essais expérimentaux réalisés sont des essais de traction uniaxiale, des essais biaxiaux (acier doux St14) ainsi que des essais Nakajima (acier doux St14 et alliage d'aluminium Al6106). Une méthode de corrélation d'images numérique est utilisée pour la mesure des déformations. La figure ci-dessous, représente les points expérimentaux (CLF) pour deux valeurs de taille de défaut initiales pour l'acier doux St14. Les textures expérimentales sont mesurées à l'aide la méthode de diffraction aux rayons X pour plusieurs trajets de déformations.

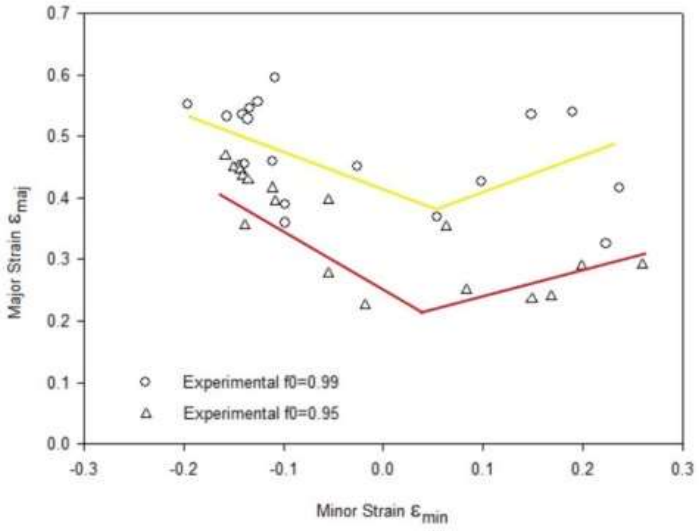

Figure 9. CLF expérimentale pour l'acier doux St14 et pour un essai biaxial

La figure 10 représente les différents emboutis obtenus lors des essais Nakajima pour l'alliage d'aluminium Al6061 et l'acier doux St14. Enfin, la figure 11 représente les CLF obtenues expérimentalement pour les deux matériaux étudiés.

(a) **(b)**

Figure 10. Essai Nakajima, emboutis pour l'Al6061 (a) et l'acier doux St14(b)

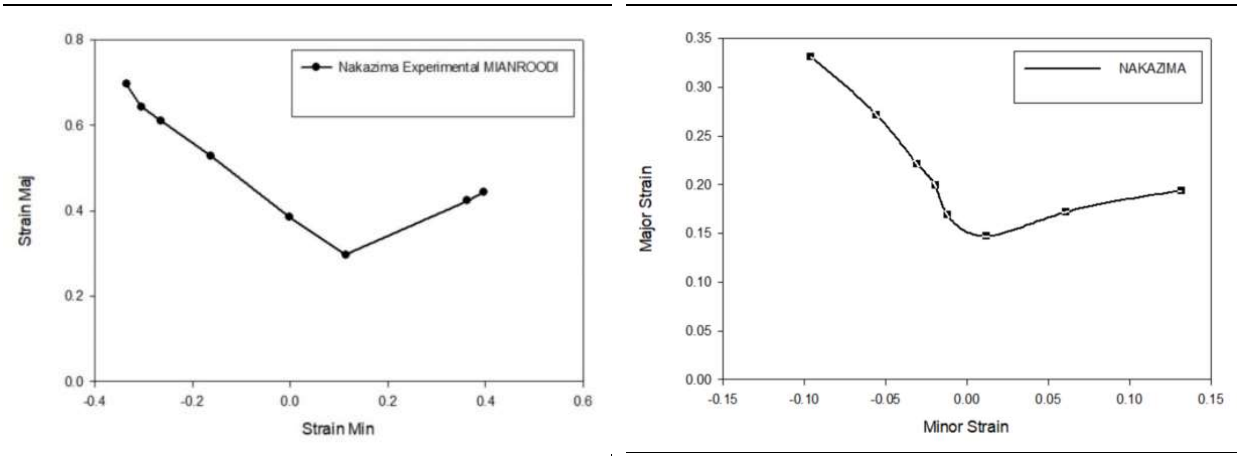

a) **b)**

Figure 11. CLF obtenues expérimentales pour l'Al6061 (a) et l'acier doux St14(b)

Enfin, les figures 12 et 13 représentent les pole figures mesurées pour les deux matériaux étudiés. Les mesures confirment bien que les textures dépendent de la structure cristallographiques et du trajet de déformations.

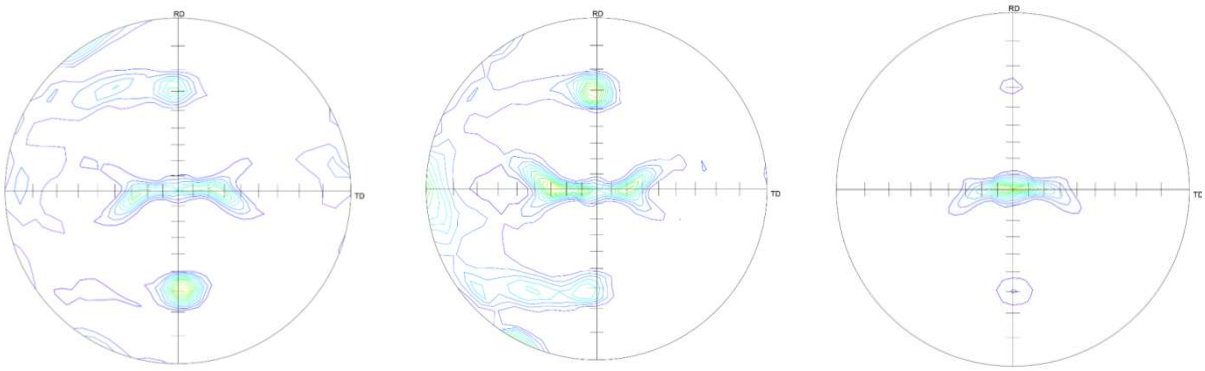

(a) Uniaxial point **(b) Plane strain point** **(c) Equibiaxial point**

Figure 12. Experimental (220) pole figures for Al6061 (CFC)

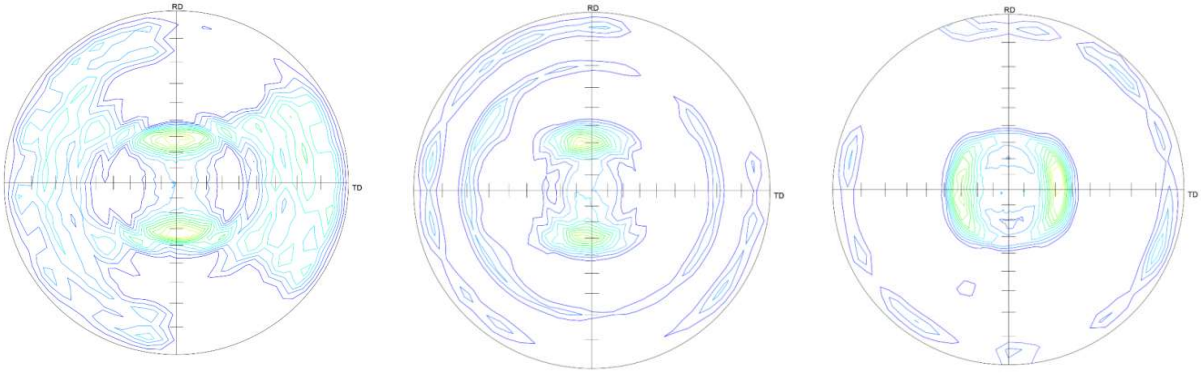

a) Uniaxial point **(b) Plane strain point** **(c) Equibiaxial point**

Figure 13. Experimental pole figures (220) for St-14 (CC)

Finalement, les résultats expérimentaux sont en accord avec les résultats numériques et la littérature pour les deux matériaux étudiés.

- **Liste des travaux**

[Journal] Mianroodi, Mohammad, Altmeyer, Guillaume, Touchal, Siham
Experimental and numerical FEM-based determinations of forming limit diagrams of St14 mild steel based on Marciniak-Kuczynski model, Journal of Mechanical Engineering and Sciences, Vol. 13, pp. 5818-5831, 2019, DOI : 10.15282/jmes.13.4.2019.08.0464

[Conférence] Mianroodi, Mohammad, Touchal, Siham, Altmeyer, Guillaume
Comparison of Forming Limit Diagrams for FCC and BCC materials using Taylor and Marciniak-Kuczynski models
International conference with proceedings ICSET 2019
International conference on science, engineering & Technonolgy, Toronto, Canada, février 2019

[Conférence] Altmeyer, Guillaume, Touchal, Siham, Mianroodi, Mohammad
Coupling of micromechanical phi-model and plastic instability Marciniak-Kuczynski model for Forming Limit Diagrams predictions
3rd International conference on computational plasticity, Barcelona, septembre 2017

[Conférence] Mianroodi, Mohammad, Touchal, Siham, Altmeyer, Guillaume
Numerical Prediction of Forming Limit Diagrams using Marciniak-Kuczynski instabilities criteria and texture evaluation of roll forming process
International congress of interdisciplinary studies in science and engineering, juillet 2017

[Conférence] Touchal, Siham, Mianroodi, Mohammad, Altmeyer, Guillaume, Ahzi, Said
Prediction of Forming Limit Diagrams using the phi-model and the Marciniak-Kuczynski model
First International Conference and Workshop on Mechanical Engineering Research
Research Trends in Mechanical Engineering 2016, RTME 2016, University of Aveiro, Portugal, 11-13 July 2016

[Poster] Numerical simulation of sheet metal forming processes for polycrystalline materials with M-K approach, Journée de la mécanique, France, 2017.

[Poster] Micromechanical modeling of polycrystalline materials Application to sheet metal forming processes, Journée doctorale MSII, France, 2016.

Introduction

Diffuse or strain localization usually limits the formability of metal sheets during many industrial processes. Therefore, for industrials, numerical tools are necessary in order to quantify the formability of sheets as well as a deep understanding of the mechanism of necking. In this way, the forming processes can then be optimized which will lead in time-saving, reduction of cost and a better quality of the products.

Forming Limit Diagram (FLD) constitutes a good tool for the estimation of the formability of metal sheets.

This concept of forming limit curves is not new and was first given in 1946 by Gansamer (Gansamer, 1946). Then, FLD was developed in 1965 by Keeler (Keeler, 1965) from many experimental studies. Later, Marciniak (Marciniak, 1956) and Marciniak and Kuczynski (Marciniak and Kuczynski, 1965) developed a forming limit prediction model for strain localization. Marciniak in 1965 did a lot of experimental tests and by investigating the results and showed that strain localization cause of geometrical or structural nonhomogeneity (Marciniak, 1965; Banabic et al., 2010). In 1968, Marciniak developed a deep analysis on the right side of FLD and published the new model to cover both sides of this diagram (Marciniak, 1968).

Until now, FLD is still very popular and there is still a strong interest for the development of both experimental and theoretical approaches. Different approaches have been developed during the last decades to draw FLD.

Experimental procedures have been developed until now to study sheet metal formability. They are well controlled and procure interesting results for a wide range of alloys. They are however really time-consuming and expensive and, what is more, they do not allow optimization of sheet metal forming parameters. Complementary analytical or numerical procedures are then necessary to avoid these limitations. Most of them have been elaborated in an elasto-plastic framework and are based on four modeling approaches.

The maximum force principle relates diffuse plastic instability with the maximum of the load during a tensile test. This principle has then been extended to multiaxial loading cases and to localized necking (Swift, 1952; Hill, 1952; Hora et al. 1996). Bifurcation analysis relates diffuse and localized necking with the loss of unicity of the solution of equilibrium problem associated with various modes (Hill, 1958; Rudnicki and Rice, 1975; Ito et al. 2000). This approach is limited to elasto-plastic models. To overcome this limitation, one may follow the multi zones method

(Marciniak and Kuczynski, 1967). According to this method, localization occurs in an initially defective zone of the metal sheet. Linear stability based on the perturbation approach was later developed (Dudzinski and Molinari, 1991; Boudeau and Gelin, 1994; Benallal, 2000).

Some limitations of the previous approach have also been enlightened. They are mostly related to insufficient consideration of the physical mechanism of plastic deformation. It seems then necessary to consider the coupling of plastic instability criteria to polycrystalline plasticity models to improve FLD predictions.

Plastic deformation usually involves microstructure changes. During forming processes of metals, a large strain is usually required. In single crystals, the plastic deformation can be activated by several mechanisms such as crystallographic slip and twinning and implies a texture evolution of heterogeneous metallic materials. The crystallographic texture is an important source of anisotropy in polycrystals. The macroscopic mechanical behavior cannot be well predicted if the texture is not taken into account. It is therefore important to predict anisotropy effects due to texture evolution as they are present in many industrial processes.

The formulation of metallic polycrystals plasticity has been the subject of many studies and different approaches have been proposed. These homogenization techniques span from the classical bounds Taylor (Asaro and Needleman, 1985; Taylor, 1938) and Sachs (Leffers and Ray, 2009; Sachs, 1928) models to the more sophisticated self-consistent approaches (Lebensohn and Tomé, 1993; Molinari et al., 1987; Ahzi and Mguil 2008).

In order to improve the prediction of FLDs, several authors attempt to include crystal plasticity framework in instability criteria (Lademo et al., 2005; Neil et al., 2009; Kim et al., 2013; Pedersen et al., 2008; Signorelli et al., 2009; Lévesque et al., 2016).

In order to present the numerical and experimental results of the determination of FLD, the manuscript is divided in 5 chapters.

Chapter 1. Sheet metal forming background

Chapter 1 constitutes the general introduction of the study. The presentation of common sheet metal forming processes is given.

Sheet metal forming is limited by various kinds of defects occurring during the mechanical processes. The problem of defects occurring during sheet metal forming is pointed out with particular attention to necking since its prediction and strain localization is the aim of the study.
The general concept of forming limit diagram is presented as well as their experimental and theoretical determination. The theory of the Marciniak and Kuczynski criterion is given in this introducing chapter.

Chapter 2. Material modeling and crystal plasticity background

In chapter 2, on may recover general details about polycrystalline materials such as the different crystallographic structures and materials defects. Different methods for texture representation are explained. The measurement of experimental textures using the X-ray diffraction (XRD) method is also presented in this chapter.
The theoretical and modeling aspects of the work are also given. The mechanical behavior at the microscale and at the macroscopic scale is presented. Main crystal plasticity models are presented in this chapter with particular attention to the Taylor (or upper-bound) model since it is used in this thesis for CPFEM simulations.

Chapter 3. Numerical FLD determination using biaxial and Nakajima tests for FCC and BCC metals: application to deep drawing simulation

This third chapter deals with the numerical investigation of strain localization and the numerical prediction of FLD.
Two numerical approaches are used in this work in order to predict localized necking. First, the Marciniak-Kuczynski (M-K) model is used in a FEM modeling of biaxial test including an initial band with reduced thickness.
The second approach is based on a FEM simulation of the Nakajima test. Fundamental differences between these models are discussed and FLD obtained with these approaches is compared. Special attention is paid to the effect of the value of the initial thickness ratio, f_0 and the orientation bands θ in the M-K model. Both FCC (Al6061 commercial aluminum) and BCC (St-14 mild steel) crystallographic structures are studied and compared.
In last, the predicted FLD is applied to an industrial case: the deep drawing simulation.

Chapter 4. CPFEM simulation of biaxial traction test with MK-approach

In this fourth chapter, Crystal Plasticity Finite Element Method (CPFEM) simulations for the M-K biaxial traction test are performed. The CPFEM has been implemented in the commercial code Abaqus software using an UMAT subroutine. The classical Taylor model is used since it allows such CPFEM simulations including the prediction of crystallographic texture evolution during plastic deformation. The evolution of the grain's orientation is investigated during the biaxial traction including the M-K criterion test for BCC and FCC crystallographic structures and analyzed in the safe zone as well as in the defect zone for different strain paths.

In the last part, some aspects about the calculation time of simulations are given since FEM run time is very important.

Chapter 5. Experimental test and validation

The last chapter presents several experimental tests performed during this thesis. The experimental results are used to validate the obtained numerical results.

The biaxial test for flat sheet for BCC (St14 mild steel) materials and the Nakajima test for FCC (Aluminum Al6106) and BCC metals are done.

The digital image correlation method is used for the measurements of strains and experimental FLD is then drawn. For both experimental tests (biaxial and Nakajima), the crystallographic textures of both specimens are investigated by XRD. Different zones and different strain paths are considered. A comparison between obtained numerical FLD, experimental FLD and FLD from literature is done.

Chapter 6. General conclusion

The last chapter constitutes the general conclusion of this work and gives a summary of the main obtained results.

Chapter 1

Sheet metal forming background

1.1 Introduction

Sheet metal forming processes are the most common manufacturing practices in industries. During the forming process, engineers cannot deform the metal sheet regardless of the sheet ductility and formability. The possibility of tearing, wrinkling, necking and other sheet material defects is very high during the mechanical process. A good formability of the metal sheet is thus very important for the forming process. Therefore, a criterion must be used to determine metal sheet formability. One of the best tools to predict the formability of the metal during forming processes is the Forming Limit Diagram (FLD). This diagram shows the critical minor and major strains at the onset of sheet metal necking.

In this chapter, the first part presents the different types of forming processes usually used in industries. The FLD background is also presented in this chapter 1. FLD can be predicted analytically and experimentally. The common analytical methods for the FLD determination are briefly presented. In this thesis, the determination of FLD is based on Marciniak and Kuczynski criterion which is extensively described in this chapter. In the last part, the experimental methods of the FLD determination are presented.

1.2 Sheet metal forming processes

The sheet metal forming processes are widely used in several industries to produce structural elements and different parts. The sheet metal forming process is a procedure to deform the sheet metals into different geometries. Several important types of forming processes such as deep drawing, roll forming, hydroforming, warm forming and age forming are presented in the following part.

1.2.1. Presentation of different sheet metal forming processes

- Hydroforming process

This type of forming process used high-pressure fluid to expand the metal sheet. The process continues until it matches the mold. For changing the shapes, the internal high-pressure fluid is used (Dohmann and Hartl, 1997). For complex geometries and brittle metals, hydroforming is chosen. The schematic of this process is shown in Figure 1 for tube hydroforming. The forming machine has two axial forces to fix the metal during the process. The fluid enters inside the case and the metal deforms (Liu et al., 1998). The process has 3 different steps. First, the tubes filled

with fluid. In the second phase, the pressure inside the tube is increased and during the last step, the metal shape is formed onto the inside geometry of the die.

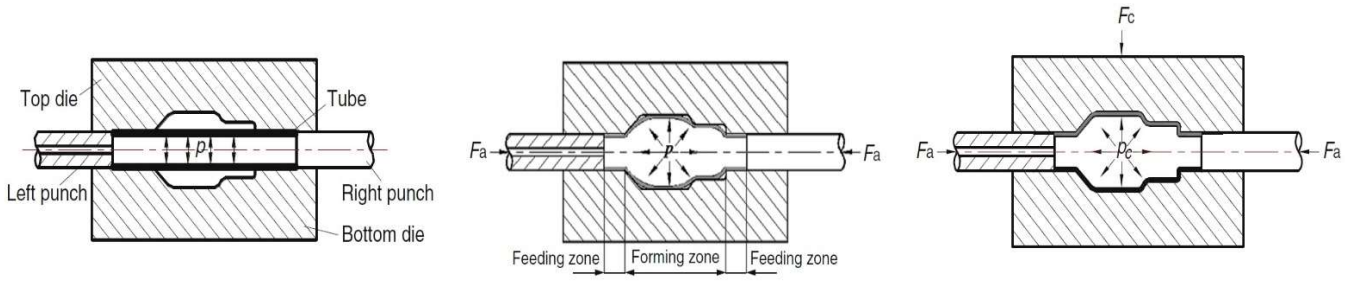

Figure 1. Tube hydroforming process (Yuan and Liu, 2014)

- Hot forming process

Temperature is one of the important parameters during this forming process. This type of process is one of the most applicable processes for forming metal sheets. The advantages of this process are shaping the complex geometries, improving the formability of metal sheets at high temperatures and decrease production time (Lange, 1985). One of the key problems in automotive industries is using a low mass material with high formability and strength (Polak et al., 2017).

By warming alloys to recrystallization temperature, changing shapes is easier than normal temperature for several types of alloys. It is well known that the sheet formability greatly improved by increasing temperature (Afshin and Kadkhodayan, 2015). By increasing the temperature of the punch and blank holder can achieve a better result. The main issue during warm forming is to keep the mechanical properties constant (Shamanian et al., 2017). Figure 2 shows the electrical heater increases the temperature of the die and sheet holder and metal sheet. Therefore, the punch can easily change the shape of the metal sheet.

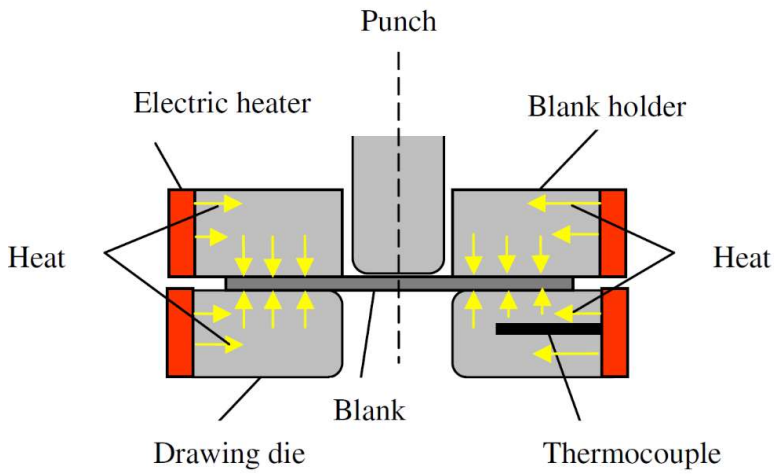

Figure 2. Warm forming (Kadkhodayan et al., 2015)

- Age forming process

The age forming process is a special type of forming process. This type of forming process is usually used for forming aluminum panels (Ribeiro and Marinho, 2010). This study is started to develop in the 1980s by Textron (Ribeiro et al., 2010). Age forming is one of a special type of forming process for airplane wings and airfoils. Figure 3 shows the different steps of this process. In the first step, sheets are given an aging treatment while simultaneously being subjected to mechanical shaping loads. In the second step, the pressure and heat are applied. It is used mainly for large parts that have to be imparted a curvature. The part shape is obtained due to the creep that occurs at the aging temperatures.

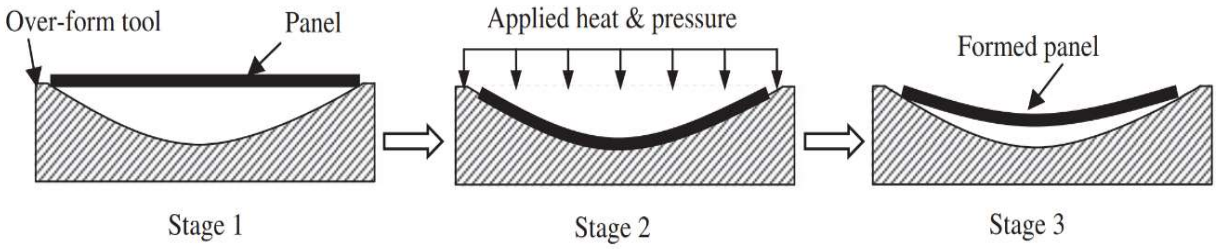

Figure 3. Age forming (Shercliff and Ashby, 1990)

1.2.2 Hot and cold rolling

Hot and cold rolling is one of the most important types of forming processes in industries. In this process, the thickness of metal sheets is reduced by passing between rollers (Radhi and Jabur, 2018). The rolling process has several types such as flat rolling, ring rolling, roll bending, roll forming, etc. Studying the temperature, this process is divided into two different types: hot and cold rolling. For cold rolling more force is needed by comparison with hot rolling so a heavier roller is needed or more rollers should be added (Kolahdooz and Aminian, 2018). Some advantages of cold rolling are high rates of production, good finish, dimensional accuracy and disadvantages are deformations limited to small reductions, limited to only a few shapes and equipment's high cost. In hot rolling, the production cost is lower than cold rolling but the shape can be changed after the process so sometimes there is another process to refine the shape. In hot rolling, the surface may be oxidized of the products and the dimensions of products are not compressed (Bagheripoor and Bisadi, 2014). Figure 4 shows different parts of the cold roll forming process.

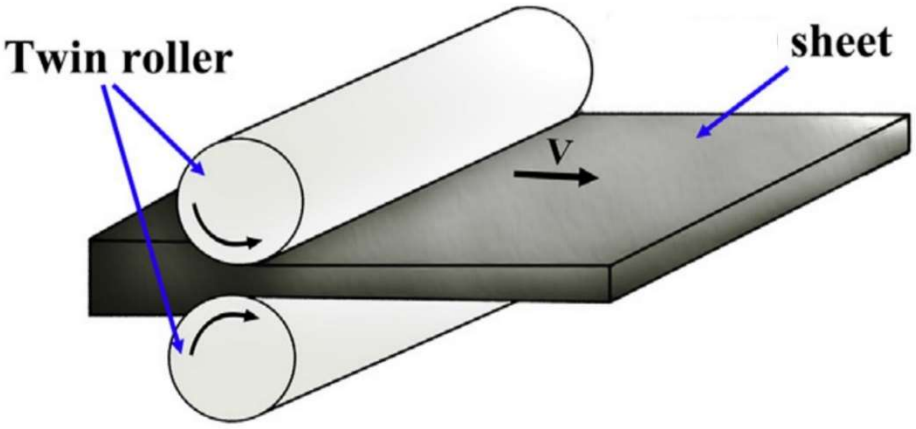

Figure 4. Rolling (Wang et al., 2019)

One of the important parameters in the rolling process is rollers. The effect of rollers size in finite element simulations is investigated by Devarajan (Devarajan et al., 2012). Flat rolling is the most popular type of rolling. 40-60% of industries use this type of rolling process (Murthy et al., 2016). Figure 5 shows the different types of cold rolling process. The rollers are important equipment for increasing the quality of cold rolling (Mander et al., 1997). In this process, adding more rollers can

change output parameters. The different types of cold rolling such as cluster mill rolling, two high mills rolling, angular mills rolling and planetary mill are presented below in figure 5.

The roller numbers and roller forces depend on input and output parameters such as materials, process time and thickness reduction. Milenin (Milenin et al., 2004) works on rolling with several steps. The rolling with 6 steps is simulated by Milenin. Soszynski (Soszyński and Studnicka, 2012) works on the best ways to increase the quality of cold rolling.

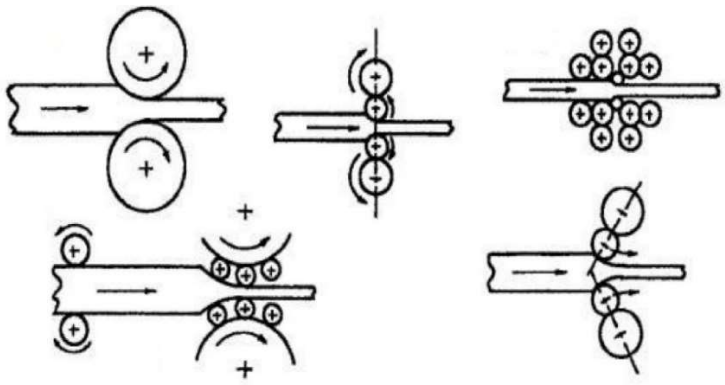

Figure 5. Common types of cold rolling (Kolahdooz and Aminian, 2018)

In recent years, industries need various metals with high strength, low density and high ductility. Therefore, multilayer metals and composites have been developed (Chen et al., 2007). This method is presented below.

- ARB process

In recent years for manufacturing high strain metals sheets, Accumulative Roll Bonding (ARB) is used. ARB is a rolling process with two or more layers of metal sheets (Karimi et al., 2018). The ARB is not only a method of plastic deformation but also a bonding process. This process has a great effect on grain strengthening and refinement on metals such as aluminum, copper, and steel (Son et al., 2016). The most widely used composites from this process are Al/Cu, Al/Zn, Al/Mg, Ti/Al, etc (Dehsorkhi et al., 2012). Aluminum/steel composite sheets properly combine the properties of the aluminum surface layer such as low weight, high specific modulus, heat expansion coefficient and low corrosion resistance properties with the good mechanical strength of the substrate steel. This composite is widely used in aerospace and automotive companies (Manesh and Karimi Taheri, 2003). In ARB, for each layer, we can use different materials (Chen

et al., 2007; Eizadjou et al., 2008). ARB process can create different types of alloys with various mechanical properties. The various metal layers can be used to create different composites. By increasing the ARB cycles, the grain refinement can be achieved. The ARB process has two main steps, the first step is to create a multi-layer sandwich model by air drying and after that by using the roller make a composite of the metals (Saito et al., 1999). The ARB process steps are shown below. Compared to other composite production methods, this method has advantages. This method does not require expensive equipment and devices and can produce continuous products at an industrial scale. The ARB process has a high productivity rate. This method can produce nanocrystalline and fine-grained composites.

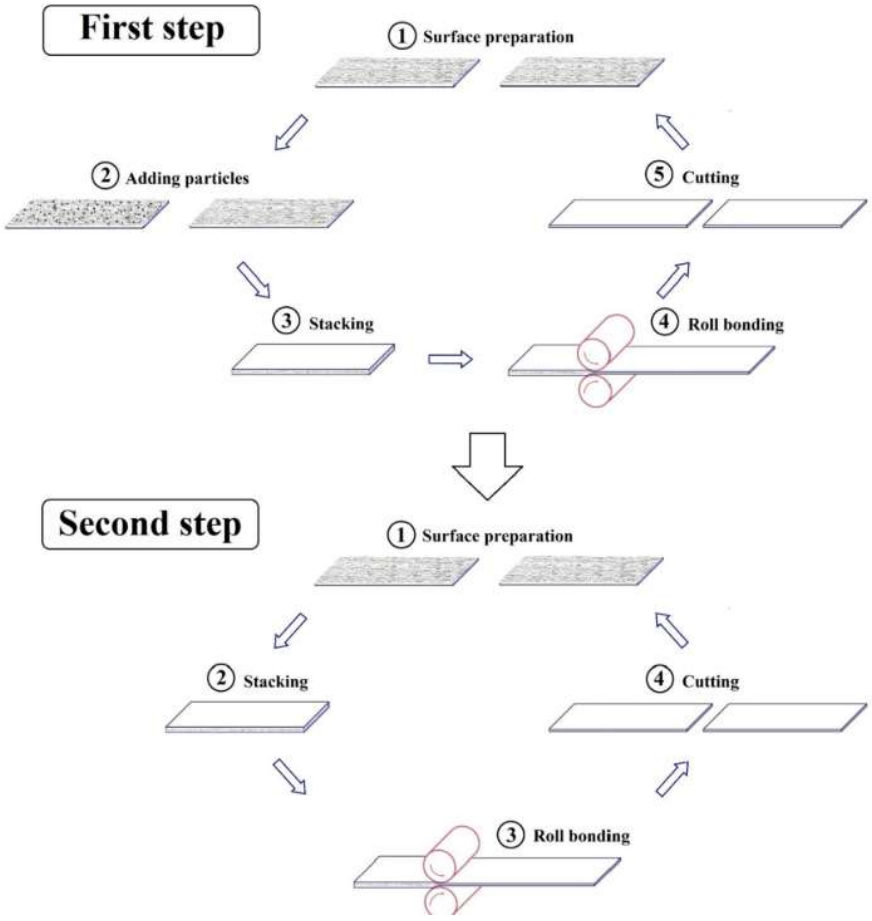

Figure 6. Schematic of the ARB process (Karimi et al., 2018)

This process is repeated 2-3 times. The thickness of the sample is decreased after n cycles:

$$t = \frac{t_0}{2^n} \quad (1.1)$$

In this equation, t_0 is the initial thickness of the model and all of the thickness reduction, r_t, after n cycles is calculated such as :

$$r_t = 1 - \frac{1}{2^n} \quad (1.2)$$

The plastic strain is calculated by equation below (Karimi et al., 2018):

$$\varepsilon = \left\{\frac{2}{\sqrt{3}} \ln\left(\frac{1}{2}\right)\right\} \times n = 0.80n \quad (1.3)$$

1.2.3 Deep drawing

Today with the development of technology and increasing competitive market, most sheet metal parts manufacturing industries produce better quality products with less time and cost. The deep drawing process is widely used in various industries for sheet metal forming. Deep drawing is a very important type of metal forming process. Deep drawing is the process of cold forming flat sheet metal into a matrix (die) without wrinkling or failure of the sheet (Kawka et al., 2001). Deep drawing is the process of turning a sheet into a shell under stress. In this mechanism, the blank sheet is controlled by the blank holder when the punch applies a normal force (Jeswiet et al., 2008). The deep drawing process is shown in Figure 7.

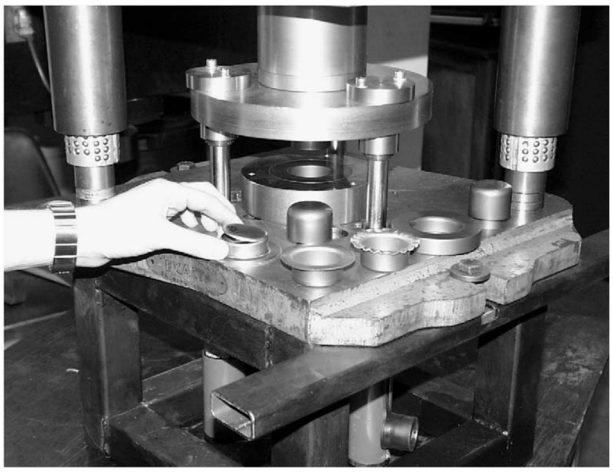

Figure 7. Deep drawing experimental machine (Colgan and Monaghan, 2003)

During the deep drawing process, many factors including material properties, tensile ratio, anisotropy of material, geometry of the punch and the die are effective. Therefore, the quality of

the products depends on the experience, skill and knowledge of the designer, which relies on trial and error. This method is expensive and time consuming.

During the deep drawing process, the blank sheet is stretched between the blank holder and the die. In deep drawing, the necking will occur on drawing part of sheet metal and the sheet mechanical properties are an important factor to control the failure. The important material parameters during this process are the density of sheet metal, fracture toughness, metal friction, etc. (Kakandikar and Nandedkar, 2002; Vishtal and Retulainen, 2012). One of the important parts of a deep-drawing machine is the punch. The shape of the metal sheet after the process depends on the punch shape. For deep drawing process the thickness of metal sheet should not be 3 times bigger than punch diameter. The main reason for wrinkling and cracking is punch force (Vishtal and Retulainen, 2012). The wrinkling can be controlled by blank holder pressure. Wrinkling is not taken into account in this study. This pressure can be calculated by the equation below (Vishtal and Retulainen, 2012):

$$P_{BH} = 10^{-3} C \left[(\beta - 1)^3 + \frac{0.005 d_0}{S_0} \right] S_u \quad (1.4)$$

$$\beta = \ln\left(\frac{d_0}{d_1}\right) \quad (1.5)$$

In these equations, d_0 is punch diameter, d_1 is sheet diameter, P_{BH} is the blank holder pressure, C is a clearance coefficient between the punch and die, S_0 a sheet parameter and S_u a load parameter. The β is correction factor to compensate for forming difficulty due to cross section shape.

Today for decreasing the production cost and time, several researchers use FE analysis of deep drawing process. In this analysis, the parameters such as the thickness of the sheet, density, and coefficient of friction and punch velocity are considered (Mansourinejad et al., 2010; Rana et al., 2020).

1.3 Formability of sheet metal

The formability of sheet metal is its capacity to withstand plastic deformation during forming processes without necking or breaking. The formability depends on several material parameters such as anisotropy ratio, strain hardening coefficient, strain rate sensitivity and on several process parameters such as strain rate, stress rate, type of forming process, temperature, etc. (Slota, 2005).

One of the major problems during the forming process is strain localization or necking (Wu et al., 2005). One of the useful tools for predicting the formability is Forming Limit Diagram (FLD).

1.3.1 Forming Limit Diagram (FLD)

Sheet metal forming is limited by failure and localized necking. The formability of sheet metals means the ability to change the shape of metal sheets to different shapes without necking. For more than 50 years, the Forming Limit Diagram (FLD) is used to predict the formability of the sheet metal. The first generation of FLD was suggested by Keeler (1963) and the second generation was published by Goodwing (1968). Keeler developed the left side for negative minor strain of FLD and Goodwin developed the right side for positive minor stain. Different theoretical models may be used to predict FLD. A FLD is a diagram of forming limit strain in the plane of principal strains. This diagram is based on major (maximum) and minor (minimum) strain in the principal plane. In this diagram, the vertical axis shows the major strain and the horizontal axis shows the minor strain. The schematic of FLD is shown below.

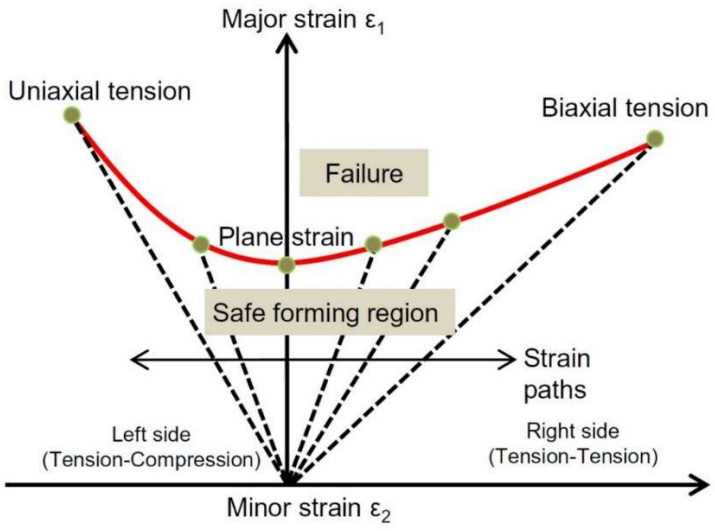

Figure 8. Schematic of Forming Limit Diagram (Shao et al., 2016)

In this figure, Forming Limit Curve shows limit strain at the starting of necking. The FLC is plotted from different strain paths, β, such as uniaxial tension point, plane strain point (FLD_0) and biaxial tension point. The diagram is divided into two different zones. The zone under FLC shows the safe forming zone and the zone upper FLC shows the necking or failure zone. The FLC shape and level depend on the material and strain path (Da Rocha et al., 1985).

The damage initiation criterion can be calculated for any major and minor strain. From this curve, the damage initiation criterion (Kolasangiani et al., 2015) is calculated below. Point A shows an example of the deformation state on FLD, see Figure 9.

$$D = \frac{AH}{BH} \tag{1.6}$$

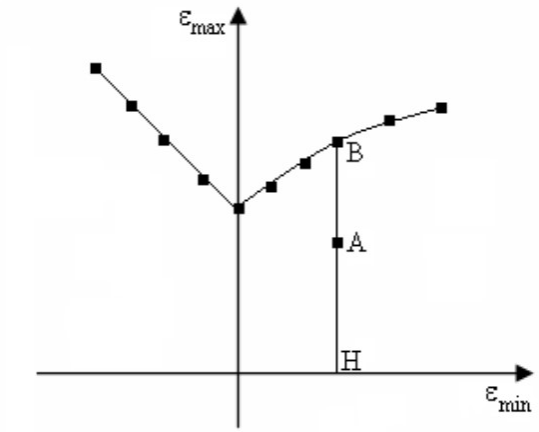

Figure 9. Forming Limit Diagram (Kolasangiani et al., 2015)

The influence of the deformation path on FLD is proposed by Müschenborn (Müschenborn and Sonne, 1975). In this method, the second force (horizontal force) is calculated as a maximum force (first force) multiplied by the α coefficient. This coefficient can be changed from 0 to 1. This method is used in Abaqus for predicting FLD.

$$F_2 = F_{max} \times \alpha \tag{1.7}$$

In recent years, forming limit stress diagrams (FLSD) are a representation of formability limits in a stress space, used for example by (Arrieux, 1995; Zhao et al., 1996; Zimniak, 2000). They are considered being less sensitive to strain path than FLD. During the experimental tests or industrial processes, the strain path uses to be non-linear, leading to difficulties in using FLD. FLDS may be used to overcome FLD limitations.

1.3.2 Analytical determination of FLD

Several analytical models have been developed to determine FLD. These models predict the formability of sheet metals. The models are divided into 3 different categories: basic models based on bifurcation theory, continuum damage mechanics and geometrical imperfection model.

1.3.2.1 Presentation of different analytical necking criteria for FLD determination

Some of the analytical models for the determination of FLD are shown below, inspired from (Zhang et al., 2018).

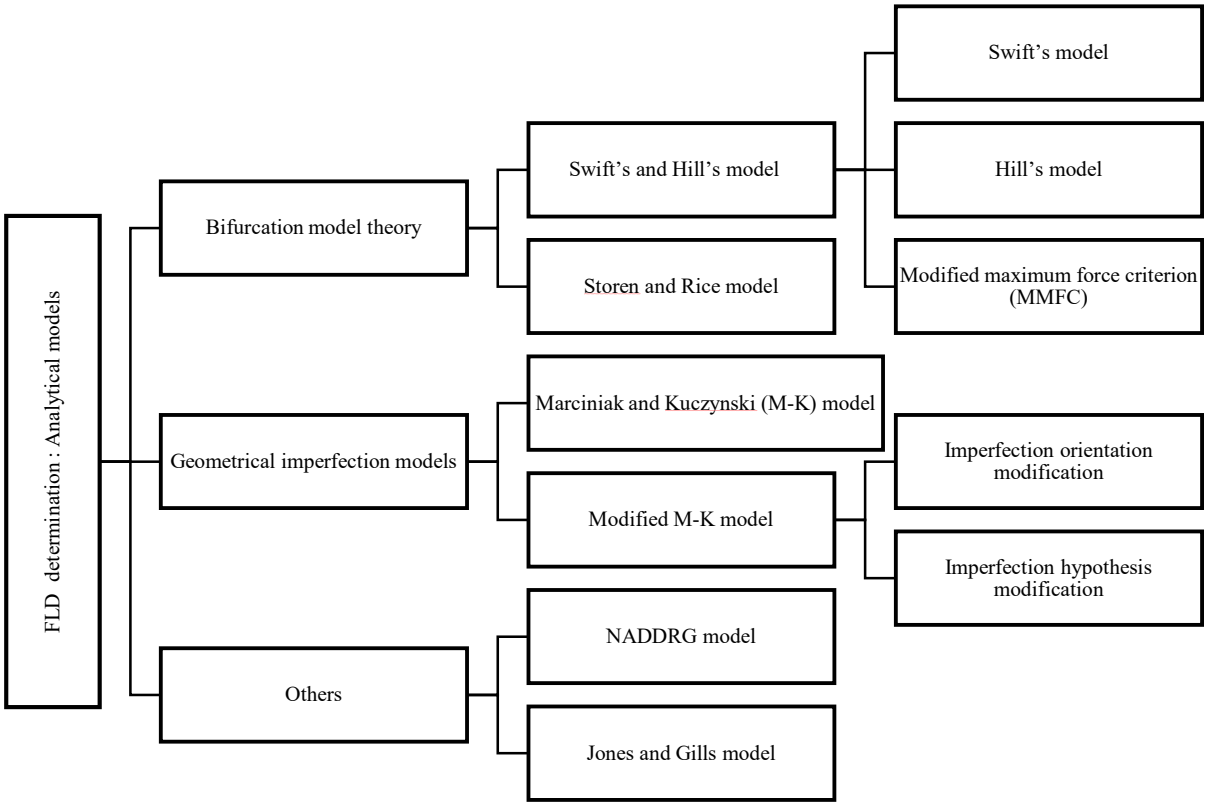

Figure 10. Analytical model for the determination of FLD

The analytical models are divided into 3 main categories. The bifurcation model and NADDRG model, J-G model are presented briefly in this part.

- Hill's criterion

One of the oldest formability prediction models is Hill's model (Hill, 1952). In this model, the metal sheet is homogeneous.

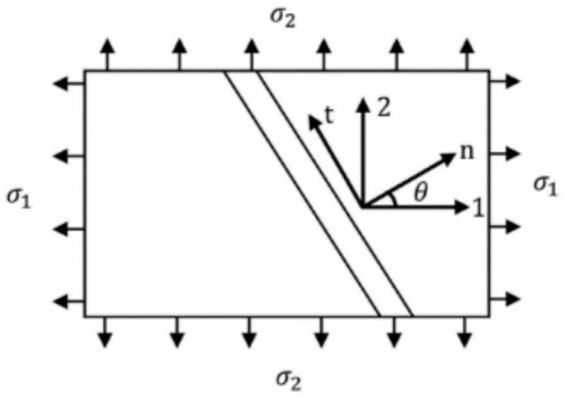

Figure 11. Hill's model (Zhang et al., 2018)

This model predicts the necking for thin metal sheets. The localization of necking happens when the maximum load is reached to the zero-extension. Hill's model can predict only the left side of FLD. In Hill's model, θ represents the angle between zero-extension direction and minor strain. The equation below shows θ:

$$\theta = \tan^{-1}\sqrt{-\beta} \tag{1.8}$$

In this equation, β represents the strain path. The equation below shows β.

$$\beta = \frac{\varepsilon_2}{\varepsilon_1} \tag{1.9}$$

In this equation, ε_1 is major strain and ε_2 is minor strain.

The localization of necking occurs when:

$$\frac{d\sigma_1}{d\varepsilon_1} = \sigma_1(1+\beta) \tag{1.10}$$

In this equation, σ_1 is the major stress. The Hill's model can predict the limit minor and major strain when the necking starts. The equations below show minor and major strain at this moment.

$$\varepsilon_1^* = \frac{\frac{\partial Y}{\partial \sigma_1}}{\frac{\partial Y}{\partial \sigma_1}+\frac{\partial Y}{\partial \sigma_2}}\,\mathrm{n} \tag{1.11}$$

$$\varepsilon_2^* = \frac{\frac{\partial Y}{\partial \sigma_2}}{\frac{\partial Y}{\partial \sigma_1}+\frac{\partial Y}{\partial \sigma_2}}\,\mathrm{n} \tag{1.12}$$

In this equation ε_1^* is the major limit strain, ε_2^* is the minor limit strain, n is the strain hardening exponent and Y is a yield function (Banabic, 2010)

- Swift's criterion

In the Swift model (Swift, 1952), the diffuse necking occurs when proportional loading equals to the maximum value. The equation below shows this assumption.

$$\frac{d\sigma_1}{d\varepsilon_1} = \sigma_1 \tag{1.13}$$

The limit minor and major strains at necking are equal to:

$$\varepsilon_1^* = \frac{\sigma_1\left(\frac{\partial Y}{\partial \sigma_1}\right)^2 + \sigma_2\left(\frac{\partial Y}{\partial \sigma_2}\right)\left(\frac{\partial Y}{\partial \sigma_1}\right)}{\sigma_1\left(\frac{\partial Y}{\partial \sigma_1}\right)^2 + \sigma_2\left(\frac{\partial Y}{\partial \sigma_2}\right)^2}\,\mathrm{n} \tag{1.14}$$

$$\varepsilon_2^* = \frac{\sigma_2\left(\frac{\partial Y}{\partial \sigma_1}\right)^2 + \sigma_1\left(\frac{\partial Y}{\partial \sigma_1}\right)\left(\frac{\partial Y}{\partial \sigma_2}\right)}{\sigma_1\left(\frac{\partial Y}{\partial \sigma_1}\right)^2 + \sigma_2\left(\frac{\partial Y}{\partial \sigma_2}\right)^2}\,\mathrm{n} \tag{1.15}$$

This criterion can predict the limit strains on positive minor strain (right side of FLD).

- Modified maximum force criterion (MMFC)

This model is developed by Hora (Hora et al., 2013). The MMFC model is an analytical model to determine FLD. This model is based on the Swift model by considering the effect of strain ratio. In this model, if the stress state transforms into a plane strain state then necking will start. The equation below shows the necking limit strain.

$$\frac{\partial \sigma_1}{\partial \epsilon_1} + \frac{\partial \sigma_1}{\partial \beta}.\frac{\partial \beta}{\partial \epsilon_1} = \sigma_1 \tag{1.16}$$

In this equation, $\frac{\partial \sigma_1}{\partial \epsilon_1}$ represents strain hardening effect and $\frac{\partial \sigma_1}{\partial \beta}.\frac{\partial \beta}{\partial \epsilon_1}$ represents an extra hardening effect. Hora added the effect of hardening and yield loci coupled with the effect of sheet thickness and sample curvature (Hora and Tong, 2008). The equation below presents the enhanced model of MMFC.

$$\frac{\partial \sigma_1}{\partial \varepsilon_1}\left[1 + \frac{t}{2\rho} + e(E,t)\right] + \frac{\partial \sigma_1}{\partial \beta}\frac{\partial \beta}{\partial \varepsilon_1} = \sigma_1 \tag{1.17}$$

In this equation, t is the thickness of the sheet metal and ρ is the sheet curvature radius. $e(E,t)$ is described below:

$$e(E,t) = E_0 \left(\frac{t}{t_0}\right)^k \tag{1.18}$$

In this equation, E_0 and k are material constants and t_0 is the initial thickness

- NADDRG model

This model is developed by Keeler (Keeler et al., 1977). In this model, FLD is a combination of two lines through the major principal strain ε_0 in the plane strain state. On the left side of FLD, the line has a 45° angle with the major strain axis and on the right side has a 20° angle with the major strain axis. An example of NADDRG FLD is shown below. This figure shows the NADDRG FLD is higher than Hill and Swift criteria. All the experimental points are under the NADDRG Forming Limit Curve.

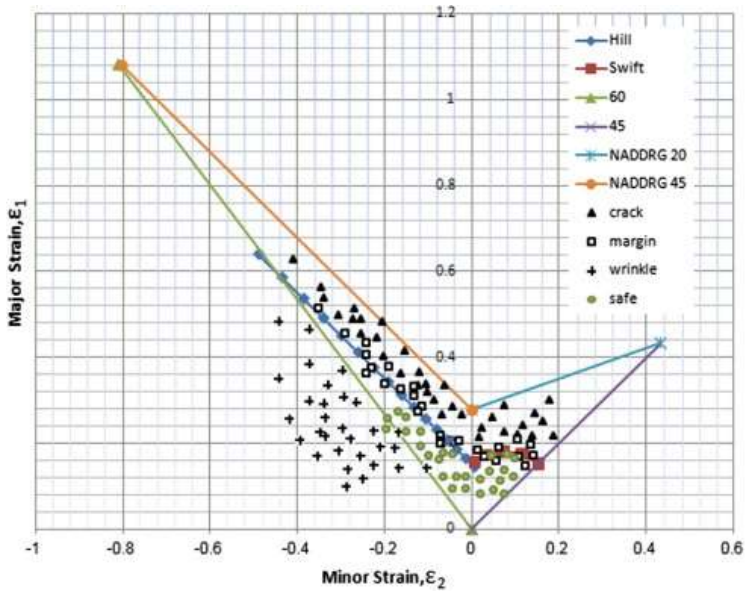

Figure 12. NADDRG FLD comparison with other models (Djavanroodi and Derogar, 2010)

The major strain in the plane strain state is calculated by the equation below:

$$\varepsilon_0 = \frac{(23.3+14.13\ _0)n}{0.21} \tag{1.19}$$

In this equation, t_0 is the initial sheet thickness and n is the material strain exponent.

- Jones and Gills model

This model is an analytical model to predict limit strain at necking. Each deformation process is divided into three steps. The first step is starting the test until maximum loading, the second step is maximum loading and the third step is necking for uniaxial traction test. Figure 13 shows the samples for this model.

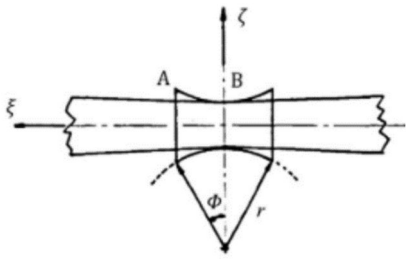

Figure 13. The sample geometry used in the J-G model (Choi et al., 1989)

This model can predict the limit strain on the right side of FLD. The right side of FLD is calculated by Jones (Jones and Gillis, 1984) for AA1100. The right side of FLD by using this model and the experimental test is shown in Figure 14.

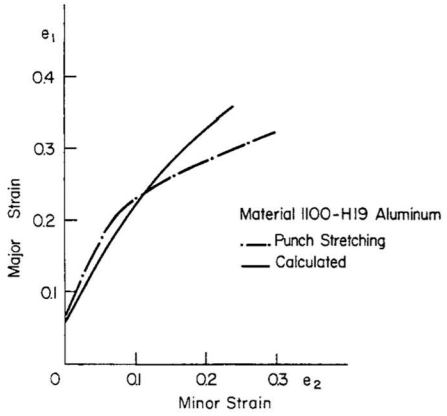

Figure 14. Comparison of J-G model FLD with experimental FLD for AA1100 (Jones and Gillis, 1984)

1.3.2.2. Marciniak and Kuczynski criteria for FLD determination

This model is based on a geometrical imperfection before deformation. This model was introduced by Marciniak and Kuczynski (Marciniak and Kuczyński, 1967) with the groove perpendicular to the principal force F_1. After that, Hutchinson (Hutchinson, 1970) extended the M-K model to the

negative strain paths based on a groove inclined at an angle θ. In this model, the limit strain depends on geometrical parameters. Figure 15 shows a schematic of the M-K model.

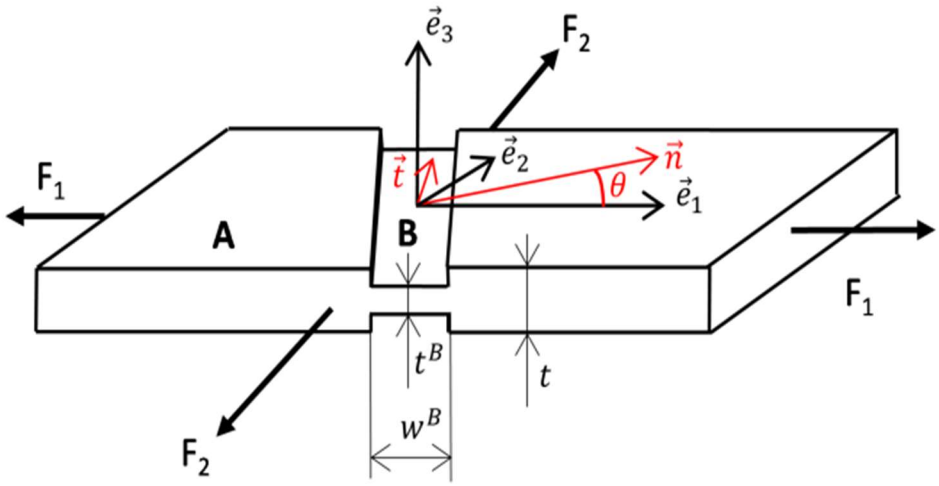

Figure 15. Schematic of the M-K model (Altmeyer et al., 2010)

This parameter physically introduces the thickness of the defect zone and the failure will occur in this zone. This small thickness defect can be compared with the real defect zone in the materials or structures. This parameter is often defined by the user, despite experimental studies have been carried out in order to quantify the influence of surface defects (Hiroi and Nishimura, 1997). The initial thickness ratio is represented by f_0:

$$f_0 = \frac{t^B}{t} \tag{1.20}$$

In this equation, t^B is the thickness of the defect zone and t is the initial thickness of the perfect zone. The force equilibrium is characterized in both zones by the equation below:

$$\sigma_{nn} t = \sigma_{nn}^B t^B, \sigma_{nt} t = \sigma_{nt}^B t^B \tag{1.21}$$

The θ angle evolution between the major main loading direction and the normal of the defect zone can be calculated from geometrical methods depending on the kinematic problem in the defect zone. During the plastic deformation, the groove orientation is updated using the equation below. The first method to calculate the groove angle is presented below (Butuc et al., 2002).

$$\tan(\theta + \Delta\theta) = \frac{1+\Delta\varepsilon_{11}}{1+\Delta\varepsilon_{11}^B} \tan\theta \tag{1.22}$$

The second method to determine the groove angle can link the value of the initial angle to the value of angle during deformation. This method is used for angle determination for the linear load case. In this method, the value of the angle is calculated by equation below (Cao et al., 2000).

$$\tan(\theta) = \exp\left(\varepsilon_1^A - \varepsilon_2^A\right) \tan(\theta_0) \qquad (1.23)$$

The influence of different initial groove orientations is calculated by Altmeyer (Altmeyer, 2011). The figure below shows the influence of initial groove orientation on FLD. FLC are sensible to the initial groove orientation. The right side of FLD is not sensible to the initial groove orientation but the left side is changed by this parameter. The critical orientation angles will happen from 30˚ to 45˚. This figure shows an example of the initial groove orientation on FLC. The lower FLC is calculated for θ=30° in this example so the critical groove orientation in this example is 30°.

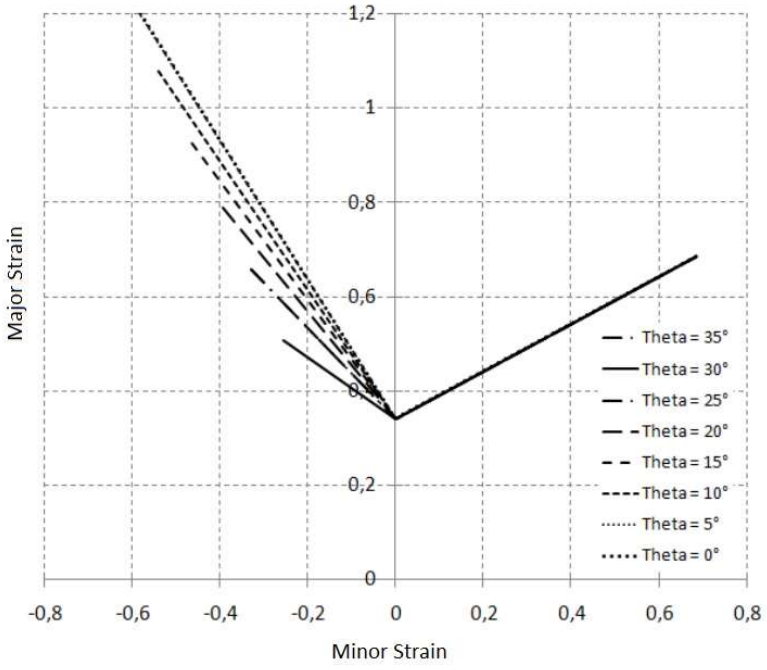

Figure 16. Example of the initial groove orientation influence on the critical localized strains for uniaxial tension, plane tension and equibiaxial tension paths (Altmeyer, 2011)

The mechanical state within the geometrically affected area is then determined from the conditions of equilibrium and compatibility of the deformations at the band. The compatibility condition of the deformation in the defect zone is:

$$D_{tt}^{B} = D_{tt} \tag{1.24}$$

In this case, the three conditions of the forces cross the defect zone are represented as below:

$$(n_1\sigma_{11}^{B} + n_2\sigma_{21}^{B})t^{B} = (n_1\sigma_{11} + n_2\sigma_{21})t \tag{1.25}$$

$$(n_1\sigma_{12}^{B} + n_2\sigma_{22}^{B})t^{B} = (n_1\sigma_{12} + n_2\sigma_{22})t \tag{1.26}$$

$$(n_1\sigma_{13}^{B} + n_2\sigma_{23}^{B})t^{B} = (n_1\sigma_{13} + n_2\sigma_{23})t \tag{1.27}$$

The imperfection parameter *f* is represented by:

$$f = \frac{t^{B}}{t^{A}} = f_0 \exp(\varepsilon_{33}^{B} - \varepsilon_{33}^{A}) \tag{1.28}$$

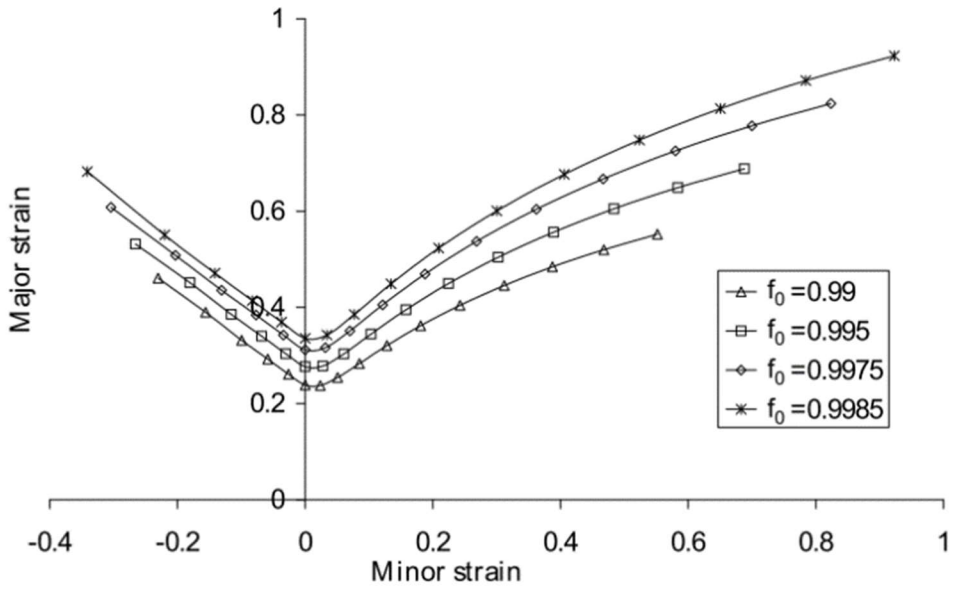

Figure 17. Effect of initial imperfection f_0 on FLD (Zhang et al., 2010)

β represents the linear strain ratio in the perfect zone (zone A).

$$\beta = \frac{\Delta\varepsilon_{22}^{A}}{\Delta\varepsilon_{11}^{A}} \tag{1.29}$$

Form β the strain increment in zone B can be determined. Necking will happen in zone B after several loading increments. The whole of FLD can be obtained by joining points obtained for different loading paths. Figure 17 shows that the FLD are sensitive to the value of the initial

thickness ratio (Zhang et al., 2008). Increasing the value of the initial thickness ratio leads to higher formability predictions.

For predicting the stop criterion on the M-K model, the strain and stress are evaluated in the safe and defect zone. Deformation occurs in the defect zone. Also in numerical simulation, the deformation acceleration in the defect zone is higher than the perfect zone. The prediction of the localization can then be made from the comparison of certain relevant mechanical quantities during loading (Altmeyer, 2011). Different localization indicators may then be constructed to predict localization. In this part, the out-of-plane strain rate ratio is used as a strain localization measurement. Localization is predicted when this ratio exceeds a user-predefined value S_{MK} proposed by Evangelista et al. (2002):

$$S_{MK} = \frac{\epsilon_{33}^{A}}{\epsilon_{33}^{B}} \tag{1.30}$$

In previous equation, ϵ_{33}^{B} and ϵ_{33}^{A} represent the deformation in the thickness in zone B and the thickness in zone A, respectively. When S_{MK} is decreasing less than 0.8, the simulation is stoped and minor and major strains for this loading ratio are stored.

Figure 18 shows the effect of different analytical models on FLD. The FLD with different analytical models has a big difference. The left side of FLD is very sensible to the different analytical models (Zhang et al., 2008) but the right side is changed slower than the left side. On the left side, the higher value is for the M-K model. On the right side, the higher value is for the NADDRG model.

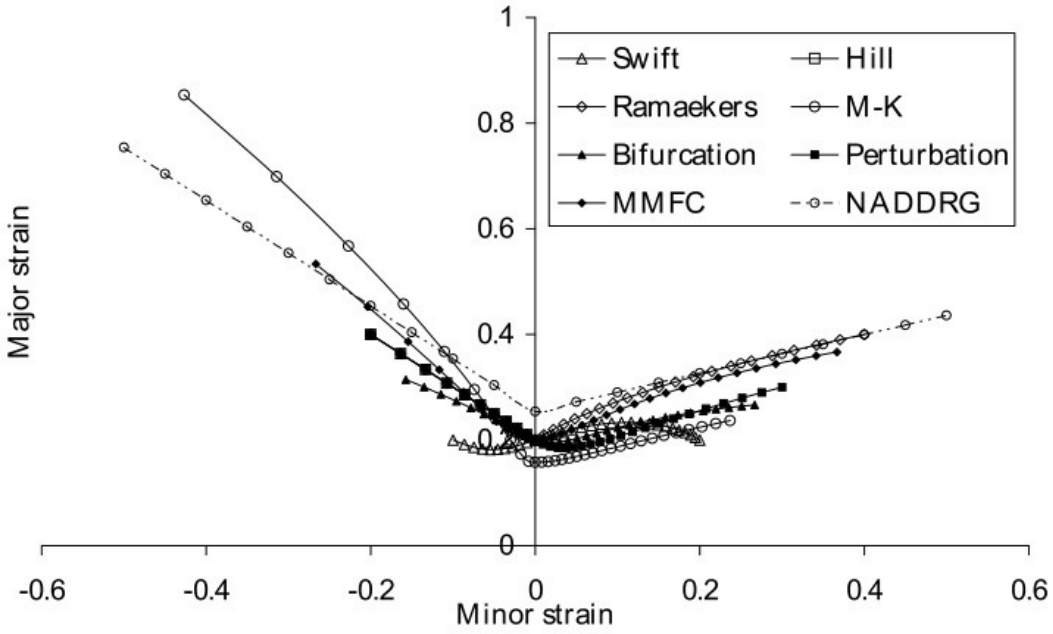

Figure 18. Effect of different analytical models on FLD (Zhang, 2008)

1.3.3 Experimental determination of FLD

1.3.3.1 Presentation of different experimental methods for FLD determination

Three different methods are used to determine the experimental FLD: biaxial flat test, cruciform biaxial test and Nakajima test. The flat and cruciform specimens are described below.

- Flat specimen

For deep drawing (punch test) or biaxial traction test, the eclipse or square flat plate is very common (Bird and Duncan, 1981). Figure 19 shows the flat plate specimens for the biaxial traction test. In the middle of these specimens, the gauge region is located. The thickness of this region is lower than the initial thickness.

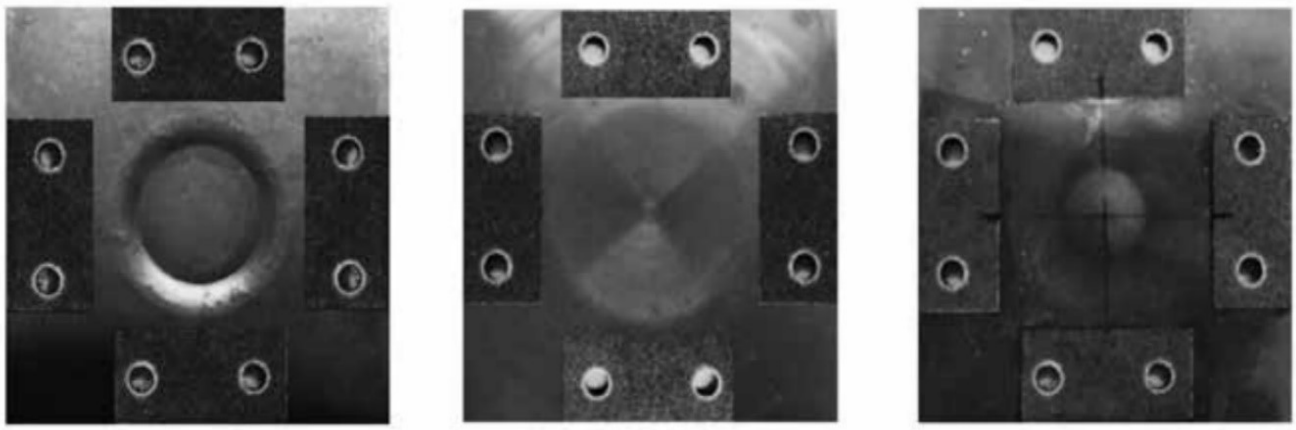

Figure 19. Flat specimen with bolt holes (Chowdhury et al., 2015)

The first disadvantage of this model is edge deformation and that the stress distribution is non-homogeneous (Chowdhury et al., 2015). The second disadvantage is that loading characterization of this model depends on the shape of the specimen during the test so the force is not varied. The important advantage of this model is very easy for manufacturing the specimen.

- Cruciform specimen

One of the best ways to determine stress and strain in different directions is the biaxial traction test (Lamkanfi et al., 2010; Welsh and Adams, 2002). The previous studies show that the tolerable cruciform specimen should contain three main features: 1- the failure must happen in gauge zone 2- It should be capable to distribute homogeneous stress in gauge zone 3- all of the material for reinforcement and test zone should be the same (Lamkanfi et al., 2010; Welsh et al., 2006). In different cruciform shapes, the cross-section area abides against forces. In the biaxial test, the cruciform shape with a central square gauge is very common. The other type of cruciform specimen obtained lots of limbs with a central part of a cruciform with the center circle part. Figure 20 shows two types of cruciform specimens.

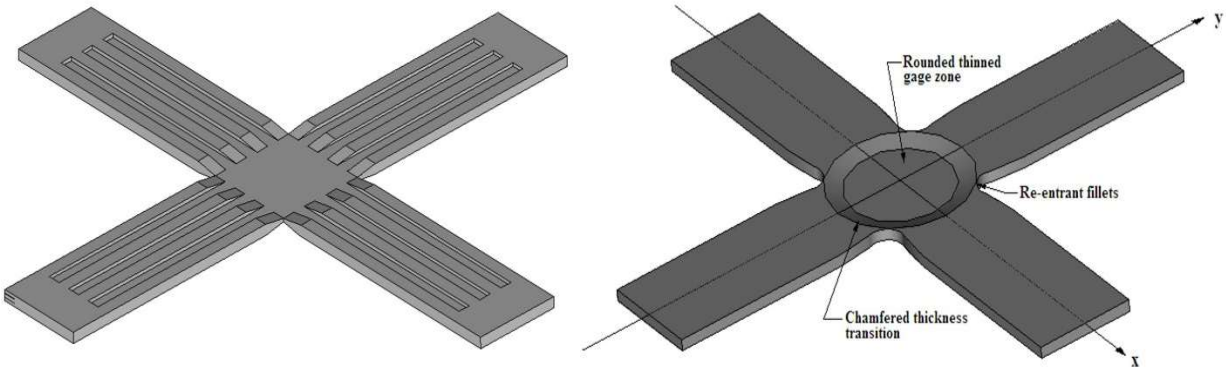

Figure 20. Different cruciform specimen (Hanabusa et al., 2013)

One of the important points for choosing the type of cruciform specimen is designing the arm joints for decreasing the failure (Lamkanfi et al., 2009). The other important parameter for designing is gauge size. If this gauge zone size is decreased too much, the test will fail.

There are several new ways to design the gauge zone to distribute a stress/strain homogeneously along the specimen. Also, the fillets in each corner are very important to lead the stress in the best way (Galster, 1963; Lecompte et al., 2007).

1.3.3.2 Nakajima formability test for FLD determination

This method is an out-plane strain test for the determination of FLD. In the Nakajima test, different strain paths can be obtained by stretching different size specimens with the hemispherical punch and circular molds. The mold used in this test includes a punch, a matrix, and a sheet holder. Figure 21 shows a schematic of the Nakajima test.

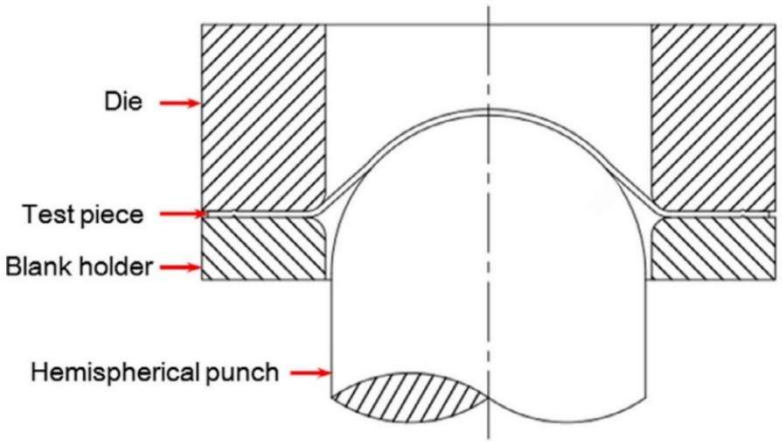

Figure 21. Schematic of the Nakajima test (Zhang et al., 2017)

Nakajima's experimental test is performed according to the ISO 12004 standard (International Standard ISO 12004-2, 2008). In this test, the deformations of 8 samples are studied. Each sample gives one point on FLD.

One of the methods for measuring the deformation of specimens used electrolytic etching. In this method, the positive and negative pole and electrolytic etching chemical dilution are used to create circles on the metal. The white and black grids are created on the surface of specimens before deformation. The black grid needs more voltage than the white grid for marking on the specimen surface. So, the surface oxide is created on the metal surface. The white grids are used for aluminum alloy specimens. The black grids are used for steel alloy specimens. The experimental determination of strain in Nakajima tests is presented in chapter 5.

1.3.3.3 Biaxial test for FLD determination

The biaxial test is common to determine the behavior of metals in the manufacturing process. The schematic of a biaxial testing machine is shown in Figure 22. In the biaxial traction test, the specimen is stretched in two directions. The biaxial test shows the deformation of a specimen on different axis (ε_{11}, ε_{22}, ε_{33}). The important advantage of the biaxial test is representing crack propagation in a different direction.

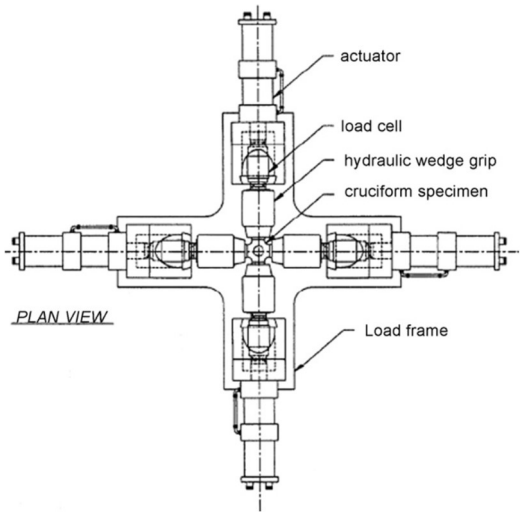

Figure 22. Schematic of biaxial testing machine (Makinde et al., 1992)

There are several methods for designing the specimens to determine the strain and stress along with the geometry. The different parts of biaxial testing machines are presented below.

For applying the load on flat plates or cruciform specimens in two different directions, biaxial testing machine is required. Compressive or tensile load must be applied continuously during the test (Ferron and Makinde, 1988; Petersen et al., 2009). The load must be applied symmetrically and the center of the specimen must stay in the center of the testing machine. A biaxial testing machine is shown in Figure 23.

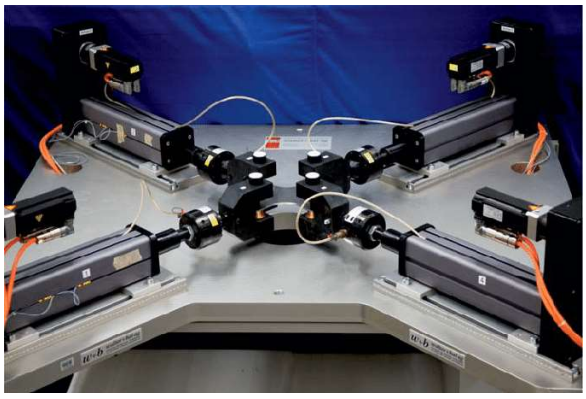

Figure 23. Biaxial testing machine (Brünig et al., 2016)

The different part of the biaxial test machine is presented below.

- Hydraulic systems

In this type of machine, the forces are applied with 4 hydraulic arms. They typically use actuators for applying forces on the specimen. The smart part of this system is servo to control a closed-loop for observing the loads and displacement of the specimen. By this testing characterization, the load ratio can be changed until a full failure. Face to face arms have the same displacement in both axes (Atrian and Panahi, 2018; Fessler and Musson, 1969; Welsh and Adams, 2000).

For distributing the same force in each direction, some modification has been applied on the testing machine by adding a pair of opposite hydraulic actuators, connected by hydraulic line. The shape of one single actuator is shown in figure 24.

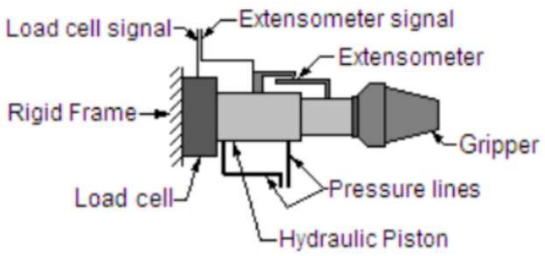

Figure 24. Schematic of the single hydraulic actuator (Olsson, 2011)

- Mechanical systems

The mechanical systems are commonly used for testing composite materials and metals. In these systems, the actuator types are less important. Mechanical or hydraulic actuators can be used. The load ratio in mechanical systems depends on the shape of the device (Ferron and Makinde, 1988). From US patent No.5905205, Dahn shows (Dahn et al., 1990) that there is a new way to apply biaxial loads on a flat plate. In this model, the four-bar linkage is attached to one vertex attachment point, so the force is applied by a uniaxial tensile force to the opposite side of the vertex. By using the force transfer to the specimen, the biaxial stress in one direction is applied and in the perpendicular direction, the compressive force is applied. The biggest disadvantages of this model are the complexity of the specimen, the operating cost and the manufacturing time.

- Strain measurement

One of the important methods to determine deformation in the biaxial traction test is the Digital Image Correlation (DIC) method. DIC is a non-contact accurate and powerful way to determine strain and deformation of the specimen (Pan et al., 2009). The first time DIC was used in 1980 by

Peters (Peters and Ranson, 1982). In the DIC method, the image is taken from step 1 until the end of the test and all of the pictures are saved. All the specimens are coated by white and black color spray. After that, the software generates all of the displacement fields from the photos with image processing technology. On the first image the coordinates and the size of the specimen are defined (Nguyen et al., 2017). This software is worked based on finding a correlation between undeformed and deformed specimens images. The DIC method will be presented in chapter 5.

1.4 Conclusion

Different approaches have been developed to predict the ability of sheet metal to be stretched.

Among the different theoretical approaches, M-K model derives from the observation that necking usually develops in a zone with a pre-existing defect in a metal sheet. A major advantage of this model is its ability to be used with viscoplastic material modeling. In Chapter 2, micromechanical based viscoplastic models will be introduced. They will then coupled with M-K approach in Chapter 3.

Biaxial testing approaches and direct deep-drawing methodologies have also been developed to predict necking and strain localization using purely experimental approaches. Implementation of these approaches will able the comparison of numerical and experimental FLD predictions in Chapter 5.

References

Afshin, E., Kadkhodayan, M. (2015). An experimental investigation into the warm deep-drawing process on laminated sheets under various grain sizes, Materials and Design, 87, 25–35. https://doi.org/10.1016/j.matdes.2015.07.061

Altmeyer, G., (2011). Modélisation théorique et numérique des critères d'instabilité plastique : application à la prédiction des phénomènes de striction et de localisation lors d'opérations d'emboutissage, Ecole Nationale Supérieure d'Arts et Métiers l'école nationale superieure d'arts et métiers.

Altmeyer, G., Abed-Meraim, F., Balan, T. (2010). Investigation of some localization criteria and their relevance to prediction of forming limit diagrams, Steel Research International, 81, 1364-1367.

Arrieux, R. (1995). Materials Processing Technology Determination and use of the forming limit stress diagrams in sheet metal forming, Journal of Materials Processing Technology, 53.

Atrian, A., Panahi, H. (2018). Experimental and finite element investigation on wrinkling behaviour in deep drawing process of Al3105/Polypropylene/Steel304 sandwich sheets, Procedia Manufacturing, 15, 984-991. https://doi.org/10.1016/j.promfg.2018.07.396

Bagheripoor, M., Bisadi, H. (2014). An investigation on the roll force and torque fluctuations during hot strip rolling process, Production and Manufacturing Research, 2(1), 128-141. https://doi.org/10.1080/21693277.2014.895916

Banabic, D. (2010). Sheet metal forming processes: constitutive modelling and numerical simulation, Springer Science and Business Media.

Bird, J. E., Duncan, J. L. (1981). Strain hardening at high strain in aluminum alloys and its effect on strain localization. Metallurgical Transactions A, 12(2), 235-241. https://doi.org/10.1007/BF02655196

Brünig, M., Gerke, S., Schmidt, M. (2016). Biaxial experiments and numerical analyses on damage prediction in metal forming processes, MATEC Web of Conferences, 80. https://doi.org/10.1051/matecconf/20168003001

Butuc, M. C., Da Rocha, A. B., Gracio, J. J., Duarte, J. F. (2002). A more general model for forming limit diagrams prediction, Journal of Materials Processing Technology, 125, 213-218.

Cao, J., Yao, H., Karafillis, A., Boyce, M. C. (2000). Prediction of localized thinning in sheet metal using a general anisotropic yield criterion, International Journal of Plasticity, 16(9), 1105-1129. https://doi.org/10.1016/S0749-6419(99)00091-1

Chen, M.C., Hsieh, C.C., Wu, W. (2007). Microstructural characterization of Al/Mg alloy interdiffusion mechanism during Accumulative Roll Bonding, Metals and Materials International, 13(3), 201. https://doi.org/10.1007/BF03027805

Choi, W., Gillis, P. P., Jones, S. E. (1989). Calculation of the forming limit diagram. Metallurgical Transactions A, 20(10), 1975.

Chowdhury, N. T., Wang, J., Chiu, W. (2015). Design of a Flat Plate Specimen Suitable for Biaxial Tensile Tests on Polym, KIT Katalog Plus, 23(9), 627-639.

Colgan, M., Monaghan, J. (2003). Deep drawing process: Analysis and experiment. Journal of Materials Processing Technology, 132(1-3), 35-41. https://doi.org/10.1016/S0924-0136(02)00253-4

Da Rocha, A. B., Barlat, F., Jalinier, J. M. (1985). Prediction of the forming limit diagrams of anisotropic sheets in linear and non-linear loading, Materials Science and Engineering, 68(2), 151-164.

Dahn, I. J. R., Van, T., Westminster, N. (1990). United States Patent, Patent Number, 2(19), 1-7.

Dehsorkhi, R., Qods, F., Tajally, M. (2012). Application of continual annealing and roll bonding (CAR) process for manufacturing Al–Zn multilayered composites, Materials Science and Engineering: A, 549, 206-212. https://doi.org/10.1016/j.msea.2012.04.035

Djavanroodi, F., Derogar, A. (2010). Experimental and numerical evaluation of forming limit diagram for Ti6Al4V titanium and Al6061-T6 aluminum alloys sheets, Materials and Design, 31(10), 4866-4875. https://doi.org/10.1016/j.matdes.2010.05.030

Dohmann, F., Hartl, C. (1997). Tube hydroforming-research and practical application. Journal of

Materials Processing Technology, 71(1), 174-186.

Eizadjou, M., Kazemi Talachi, A., Danesh Manesh, H., Shakur Shahabi, H., Janghorban, K. (2008). Investigation of structure and mechanical properties of multi-layered Al/Cu composite produced by accumulative roll bonding (ARB) process, Composites Science and Technology, 68(9), 2003-2009. https://doi.org/10.1016/j.compscitech.2008.02.029

Evangelista, S. H., Lirani, J., Al-Qureshi, H. A. (2002). Implementing a modified Marciniak-Kuczynski model using the finite element method for the simulation of sheet metal deep drawing, Journal of Materials Processing Technology, 130-131, 135-144. https://doi.org/10.1016/S0924-0136(02)00729-X

Ferron, G., Makinde, A. (1988). Design and Development of a Biaxial Strength Testing Device, Journal of Testing and Evaluation, 16(3), 253-256. https://doi.org/10.1520/JTE10375J

Fessler, H., Musson, J.K (1969). A 30 ton biaxial tensile testing machine. Journal of Strain Analysis for Engineering Design, 4, 22-26. https://doi.org/10.1243/03093247V041022

Galster, E. M. (1963). A method for producing a defined uniform biaxial tensile stress field. British Journal of Applied Physics, 14(11), 810-812. https://doi.org/10.1088/0508-3443/14/11/319

Hanabusa, Y., Takizawa, H., Kuwabara, T. (2013). Numerical verification of a biaxial tensile test method using a cruciform specimen, Journal of Materials Processing Technology, 213(6), 961-970. https://doi.org/10.1016/j.jmatprotec.2012.12.007

Hill, R. (1952). On discontinuous plastic states, with special reference to localized necking in thin sheets. Journal of the Mechanics and Physics of Solids, 1(1), 19-30. https://doi.org/10.1016/0022-5096(52)90003-3

Hiroi, T., Nishimura, H. (1997). The influence of surface defects on the forming-limit diagram of sheet metal, Journal of Materials Processing Technology, 72(1), 102-109. https://doi.org/10.1016/S0924-0136(97)00136-2

Hora, P., Tong, L., Berisha, B. (2013). Modified maximum force criterion, a model for the theoretical prediction of forming limit curves, International Journal of Material Forming, 6(2), 267-279. https://doi.org/10.1007/s12289-011-1084-1

Hora, P., Tong, L. (2008). Theoretical prediction of the influence of curvature and thickness on the enhanced modified maximum force criterion, Conference paper, Interlaken, Switzerland.

Hutchinson, J. W. (1970). Proceedings of the Royal Society A: Mathematical, Physical and Engineering Sciences.

International Standard ISO 12004-2 metalic materials sheet and strip determination of forming limit curves. (2008). Geneva, Swizerland: International organization for standardization.

Jeswiet, J., Geiger, M., Engel, U., Kleiner, M., Schikorra, M., Duflou, J., Bruschi, S. (2008). Metal forming progress since 2000. CIRP Journal of Manufacturing Science and Technology, 1(1), 2-17. https://doi.org/10.1016/j.cirpj.2008.06.005

Jones, S. E., Gillis, P. P. (1984). Analysis of Biaxial Stretching of a Flat Sheet. Metallurgical Transactions, Physical Metallurgy and Materials Science, 15 A(1), 133-138. https://doi.org/10.1007/BF02644395

Kakandikar, G.M. and Nandedkar V. M. (2002). Optimization of forming load and variables in deep drawing process for automotive cup using Genetic Algorithm.

Karimi, M., Toroghinejad, M. R., Asgari, H., Szpunar, J. A. (2018). Texture evolution and plastic anisotropy of commercial purity titanium/SiC composite processed by accumulative roll bonding and subsequent annealing, Materials Chemistry and Physics, 219(July), 182-188. https://doi.org/10.1016/j.matchemphys.2018.08.027

Kawka, M., Olejnik, L., Rosochowski, A., Sunaga, H., Makinouchi, A. (2001). Simulation of wrinkling in sheet metal forming, Journal of Materials Processing Technology, 109(3), 283-289. https://doi.org/10.1016/S0924-0136(00)00813-X

Keeler, S. P. and Brazier, W.G. (1977). Relationship between laboratory material characterization and press-shop formability, Microalloying, Vol. 75, pp. 517-530.

Kolahdooz, A., Aminian, S. (2018). Effects of important parameters in the production of Al-A356 alloy by semi-solid forming process, Journal of Materials Research and Technology, 8. https://doi.org/10.1016/j.jmrt.2017.11.005.

Kolasangiani, K., Shariati, M., Farhangdoost, K. (2015). Prediction of forming limit curves (FLD,

MSFLD and FLSD) and necking time for SS304L sheet using finite element method and ductile Article, Journal of Computational and Applied Research in Mechanical Engineering, 4(2), 121-132. https://doi.org/10.1038/jcbfm.1990.117

Lamkanfi, E., Van Paepegem, W., Degrieck, J., Makris, A., Ramault, C., Van Hemelrijck, D. (2009). Optimization of a cruciform composite specimen under biaxial loading by means of evolutionary algorithms, ICCM International Conferences on Composite Materials, 1-7.

Lamkanfi, E., Van Paepegem, W., Degrieck, J., Ramault, C., Makris, A., Van Hemelrijck, D. (2010). Strain distribution in cruciform specimens subjected to biaxial loading conditions. Part 2: Influence of geometrical discontinuities, Polymer Testing, 29(1), 132-138. https://doi.org/10.1016/j.polymertesting.2009.10.002.

Lange, K. (1985). Handbook of metal forming, McGraw-Hill Book Company, 1985, 1216.

Lecompte, D., Smits, A., Sol, H., Vantomme, J., Van Hemelrijck, D. (2007). Mixed numerical-experimental technique for orthotropic parameter identification using biaxial tensile tests on cruciform specimens, International Journal of Solids and Structures, 44(5), 1643-1656. https://doi.org/10.1016/j.ijsolstr.2006.06.050.

Liu, S.D., Meuleman, D., Thompson, K. (1998). Analytical and Experimental Examination of Tubular Hydroforming Limits, SAE Technical Paper, SAE International. https://doi.org/10.4271/980449

Makinde, A., Thibodeau, L., Neale, K. W. (1992). Development of an apparatus for biaxial testing using cruciform specimens, Experimental Mechanics, 32(2), 138-144. https://doi.org/10.1007/BF02324725

Manesh, H. D., KARIMI Taheri, A. (2003). Bond strength and formability of an aluminum-clad steel sheet, Journal of Alloys and Compounds, 361, 138-143. https://doi.org/10.1016/S0925-8388(03)00392-X

Mansourinejad, M., Mirzakhani, B., Pishbin, H., Amadeh, A., Farshchian, B. (2010). Influence of die and punch profile radii on deep drawing force and punch load-displacement diagram, AIP Conference Proceedings, 1315(January), 389-394. https://doi.org/10.1063/1.3552474

Marciniak, Z., Kuczyński, K. (1967). Limit strains in the processes of stretch-forming sheet metal,

International Journal of Mechanical Sciences, 9(9), 609-620. https://doi.org/10.1016/0020-7403(67)90066-5

Murthy, D. S., HemantPatil, Sarada. (2016). Studies on influence of roller diameter and roller speed on process parameters in hot rollig process using manufacturing simulation, International journal of current engineering and scientific research, 2394-0697, Volume-3, Issue-5.

Müschenborn, W., Sonne, H.M. (1975). Einfluß des Formänderungsweges auf die Grenzformänderungen des Feinblechs, Archiv Für Das Eisenhüttenwesen, 46(9), 597-602. https://doi.org/10.1002/srin.197503686

Nguyen, V. T., Kwon, S. J., Kwon, O. H., Kim, Y. S. (2017). Mechanical Properties Identification of Sheet Metals by 2D-Digital Image Correlation Method, Procedia Engineering, 184(Dic), 381-389. https://doi.org/10.1016/j.proeng.2017.04.108

Olsson, R. (2011). A survey of test methods for multiaxial and out-of-plane strength of composite laminates, Composites Science and Technology, 71(6), 773-783. https://doi.org/10.1016/j.compscitech.2011.01.022

Pan, B., Qian, K., Xie, H., Asundi, A. (2009). Two-dimensional digital image correlation for in-plane displacement and strain measurement: a review. Measurement Science and Technology, 20(6), 62001.

Peters, W. H., Ranson, W. F. (1982). Digital imaging techniques in experimental stress analysis, Optical Engineering, 21(3), 213427.

Petersen, D., Bonacuse, P., Kalluri, S. (2009). Axial-Torsional Fatigue: A Study of Tubular Specimen Thickness Effects, Journal of Testing and Evaluation, 21(3), 160. https://doi.org/10.1520/jte11765j

Polak, S., Kaczyński, P., Gronostajski, Z., Jaskiewicz, K., Krawczyk, J., Skwarski, M., Chorzępa, W. (2017). Warm forming of 7075 aluminum alloys. Procedia Engineering, 207, 2399–2404. https://doi.org/10.1016/j.proeng.2017.10.1015

Radhi, H. I., Jabur, L. S. (2018). Investigation the effect of roller's speed and diameter on Coefficient of friction during rolling process, International Journal of Mechanical and

Mechatronics Engineering, 18(2), 104-111.

Rana, A. K., Datta, S., Kundu, S. (2020). Deformation behaviour during deep drawing operation under simple loading path: A simulation study, Materials Today: Proceedings, 26, 750-755. https://doi.org/https://doi.org/10.1016/j.matpr.2019.12.413

Ribeiro, F. C., Marinho, E. P., Inforzato, D. J., Costa, P. R., Batalha, G. F. (2010). Creep age forming: a short review of fundaments and applications, Journal of Achievements in Materials and Manufacturing Engineering, 43(1), 353–361.

Ribeiro, F., Marinho, E. (2010). Creep age forming: a short review of fundaments and applications, Journal of Achievements in Materials and Manufacturing Engineering, 43(1), 353-361. https://doi.org/E938A604DC6FFA42E00C71152B69A156

Saito, Y., Utsunomiya, H., Tsuji, N., Sakai, T. (1999). Novel Ultra-High Str. Acta Materialia, 47(2). https://doi.org/10.1016/S1359-6454(98)00365-6

Shamanian, M., Mostaan, H., Safari, M., Szpunar, J. A. (2017). Archives of Civil and Mechanical Engineering, 17(3), 574-585. https://doi.org/10.1016/j.acme.2017.01.002

Shao, Z., Li, N., Lin, J., Dean, T. A. (2016). Development of a New Biaxial Testing System for Generating Forming Limit Diagrams for Sheet Metals Under Hot Stamping Conditions, Experimental Mechanics, 56(9), 1489-1500. https://doi.org/10.1007/s11340-016-0183-9

Shercliff, H., Ashby, M. (1990). A process model for age hardening of aluminium alloys--I, The model, Acta Metallurgica et Materialia, 38, 1789-1802. https://doi.org/10.1016/0956-7151(90)90291-N

Son, S.G., Kim, H.K., Cho, J.H., Kim, H.W., Lee, J.C. (2016). Differential speed rolling of twin-roll-cast 6xxx al alloy strips and its influence on the sheet formability, Metals and Materials International, 22(1), 108-117. https://doi.org/10.1007/s12540-015-5255-3

Swift, H. W. (1952). Plastic instability under plane stress, Journal of the Mechanics and Physics of Solids, 1(1), 1-18. https://doi.org/https://doi.org/10.1016/0022-5096(52)90002-1

Vishtal, A., Retulainen, E. (2012). Deep-drawing of paper and paperboard: The role of material properties, BioResources, 7(3), 4424-4450.

Wang, F., Qian, D., Hua, L., Lu, X. (2019). The effect of prior cold rolling on the carbide dissolution, precipitation and dry wear behaviors of M50 bearing steel, Tribology International, 132(June), 253-264. https://doi.org/10.1016/j.triboint.2018.12.031

Welsh, J. S., Adams, D. F. (2000). Development of an electromechanical triaxial test facility for composite materials. Experimental Mechanics, 40(3), 312-320. https://doi.org/10.1007/BF02327505

Welsh, J.S, Adams, D.F. (2002). An experimental investigation of the biaxial strength of IM6/3501-6 carbon/epoxy cross-ply laminates using cruciform specimens, Composites Part A: Applied Science and Manufacturing, 33, 829-839. https://doi.org/10.1016/S1359-835X(01)00142-7

Welsh, J. S, Mayes, J. S., Biskner, A. C. (2006). 2-D biaxial testing and failure predictions of IM7/977-2 carbon/epoxy quasi-isotropic laminates, Composite Structures, 75(1), 60-66. https://doi.org/https://doi.org/10.1016/j.compstruct.2006.04.049

Wu, P. D., Graf, A., MacEwen, S. R., Lloyd, D. J., Jain, M., Neale, K. W. (2005). On forming limit stress diagram analysis, International Journal of Solids and Structures, 42(8), 2225-2241. https://doi.org/10.1016/j.ijsolstr.2004.09.010

Yuan, S. J., Liu, G. (2014). Tube Hydroforming (Internal High-Pressure Forming), Comprehensive Materials Processing (Vol. 3). https://doi.org/10.1016/B978-0-08-096532-1.00304-6

Zhang, C. (2008). Etude de l'effet de la sensibilité à la vitesse de déformation sur la formabilité de tôle en alliage d'aluminium, Institut National des Sciences Appliquées de Rennes.

Zhang, C., Leotoing, L., Guines, D., Ragneau, E. (2008). Theoretical and Numerical Study of Strain Rate Sensitivity on Formability of Sheet Metal, Numisheet 2008.

Zhang, Cunsheng, Leotoing, L., Zhao, G., Guines, D., Ragneau, E. (2010). A methodology for evaluating sheet formability combining the tensile test with the M-K model, Materials Science and Engineering A, 528(1), 480-485. https://doi.org/10.1016/j.msea.2010.09.001

Zhang, L., Min, J., Carsley, J. E., Stoughton, T. B., Lin, J. (2017). Experimental and theoretical investigation on the role of friction in Nakazima testing, International Journal of Mechanical Sciences, 133 (August), 217-226.https://doi.org/10.1016/j.ijmecsci.2017.08.020

Zhang, R., Shao, Z., Lin, J. (2018). A review on modelling techniques for formability prediction of sheet metal forming, International Journal of Lightweight Materials and Manufacture, 1(3), 115-125. https://doi.org/10.1016/j.ijlmm.2018.06.003

Zhao, L., Sowerby, R., Sklad, M. P. (1996). A theoretical and experimental investigation of limit strains in sheet metal forming, International Journal of Mechanical Sciences, 38(12), 1307-1317. https://doi.org/10.1016/0020-7403(96)00014-8

Zimniak, Z. (2000). Implementation of the forming limit stress diagram in FEM simulations. Journal of Materials Processing Technology, 106(1-3), 261-266. https://doi.org/10.1016/S0924-0136(00)00627-0

Chapter 2

Material modelling and crystal plasticity background

2.1 Introduction

The atom's arrangement is important for the determination of the mechanical properties of metallic polycrystalline materials. The bonds between atoms as well as the crystallographic structure of polycrystalline materials are quite important to determine their mechanical properties. During the forming processes, the mechanical properties of polycrystalline materials are changed. The material behavior goes to plastic behavior. The plastic deformation is involved during processes such as cold rolling and deep drawing and changes the microstructure of polycrystalline materials. The polycrystalline materials develop a crystallographic anisotropy when the grains orientations are changed. Changing grain's orientations is the main reason for anisotropic polycrystalline properties.

In this chapter 2, the different crystallographic structures are presented. Then, the classical mechanical behavior of polycrystalline materials at macroscopic scale is given including flow rule, hardening law and yield criterion. After that, the mechanical behavior of such materials is presented at a microscopic scale. Classical constitutive model for crystal plasticity is given in this chapter 2. The different crystal plasticity models such as Sachs, Taylor, Self-consistent model are presented in this chapter 2. The Taylor model will be used for CPFEM simulations in chapter 4. In the last part, different methods for textures representation are explained. In this thesis, the pole figure and inverse pole figure are used to represent material crystallographic textures. In last, the X-ray diffraction (XRD) method for the measurement of experimental textures is presented.

2.2 Polycrystals background

2.2.1 Microstructure in single crystal

Metals are formed of a multitude of small polyhedral volumes called grains or single crystals. The grain size may depend on the forming process and usually ranges between 2 μm until 300 μm. The grains are bounded by surfaces called grain boundaries. In the case of single crystals, all unit cells have the same crystallographic orientation. Each grain is one unit of polycrystalline material. If each crystal lattice has a different orientation, the material is a polycrystalline one. The material with homogeneous grain distribution has the same macroscopic mechanical properties in all directions. These materials are isotropic. If the grains are oriented in a given crystallographic direction, the macroscopic mechanical properties are not the same in different directions. This type

of material is anisotropic. The grain orientation can be changed under deformation or during the material's recrystallization.

In each polycrystalline material, the metal's atoms are connected by metal bonds and it makes an atoms network or lattice. This polycrystalline network structure is presented in Figure 25.

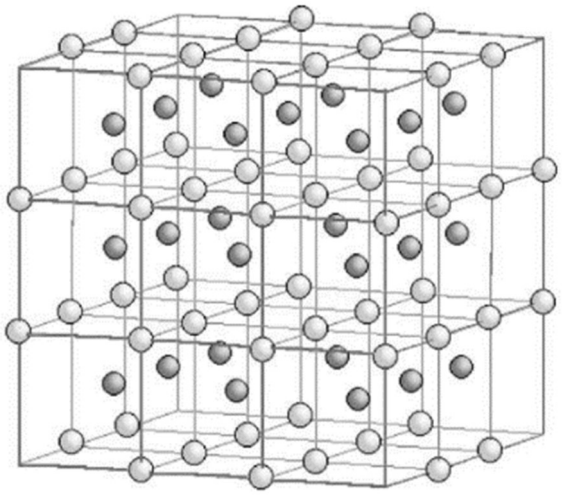

Figure 25. Schematic polycrystalline network (Lord and Ranganathan, 2004)

The mechanical properties of polycrystalline materials depend on the atom structures. There are 7 structures systems and 14 atom arrangement systems named Bravais lattice. The most common systems are cubic, tetragonal, orthorhombic, hexagonal, rhombohedral. For metals, the most common systems structures are body-centered cubic (BCC), face-centered cubic (FCC) and hexagonal close-packed (HCP). In this thesis, only the BCC and FCC structures are considered for the analysis of the crystallographic structures effect on the material texture evolution and forming limit diagram determination.

2.2.2 Crystallographic planes and directions

Each lattice has different crystallographic directions and planes. Plastic deformation such as slip and twinning occurs in certain planes and in certain directions only. A crystal lattice is a set of arranged points. A crystalline lattice is thus defined as an infinite space obtained from an elementary cell.

A crystallographic direction, $\vec{r}$, is designated by the following Miller indices [u v w] such as :

$$\vec{r} = u\vec{a} + v\vec{b} + w\vec{c} \quad (2.1)$$

In previous equation, a, b and c are the lengths of the three sides of the unit cell (see Figure 27). The cubic structures are symmetric. In some cubic crystal systems, there are equivalent but not necessarily equal crystallographic directions. This family of symmetrical cubic direction is noted <u v w>. For example, for cubic, the symmetrical direction <111> includes the $[111], [\bar{1}11], [1\bar{1}1], [11\bar{1}]$ directions.

A crystallographic plane is represented by the three Miller indices: h, k and l. These Miller indices are the inverses of the intersections of the plane with the three axis of the crystal. These intersections are measured as a function of the lengths a, b and c (see Figure 27).

The plans are noted as (h k l). The families' planes are defined as {h k l}. For example for cubic structure, the {110} family plan contains (110), (101), (011), (110), (101), (011) plans. Some different crystallographic planes are presented in Figure 26 for a cubic structure.

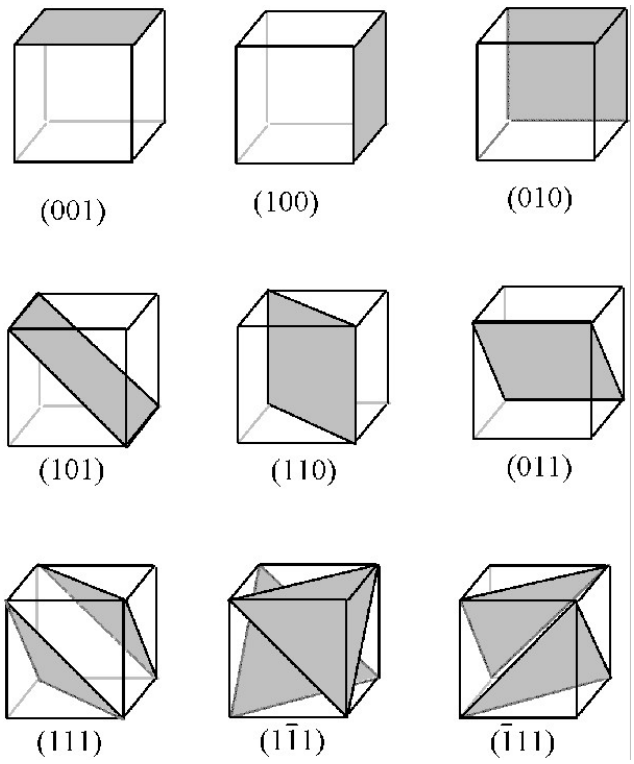

Figure 26. Example of crystallographic planes in a cubic structure

2.2.3 Different crystal structures

The different lattice systems are presented in Table 1. A unit cell is always drawn with lattice points at each corner, but there are also lattice points at the center of certain faces or the center of volume in the cells of some lattice (Austin and McDowell, 2011; chin and Hosford, 1969; Kalidindi and Bronkhorst, 1992; Toroghinejad and Dini, 2006). A crystal lattice is the set of regularly arranged points. Figure 27 shows the different parameters of a single crystal. The geometry of the elementary cell is defined by six parameters: a, b, c, α, β, γ. The lengths of the three sides are a, b and c. The three angles are defined by α, β and γ.

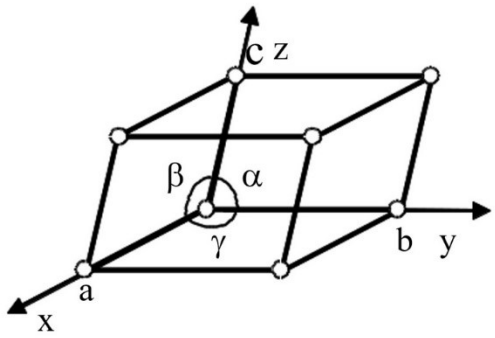

Figure 27. Different parameters of single crystal

The relations between these parameters build different crystalline systems presented in table 1. The different axis length, different angles built 14 types of Bravais lattice.

System	Axial, Lengths, Angles	Bravais lattice
Cubic	a = b = c, α = β = γ = 90	Simple Body-centered Face-centered
Tetragonal	a = b ≠ c, α = β = γ = 90	Simple Body-centered
Orthorhombic	a ≠ b ≠ c, α = β = γ = 90	Simple Body-centered Base-centered Face-centered
Rhombohedral	a = b = c, α = β = γ ≠ 90	Simple
Hexagonal	a = b ≠ c, α = β= 90, γ =120	Simple
Monoclinic	a ≠ b ≠ c, α = γ = 90 ≠ β	Simple Base-centered
Triclinic	a ≠ b ≠ c, α ≠ β ≠ γ ≠ 90	Simple

Table 1. Crystalline systems - Bravais lattice

2.2.4 Deformation in crystals

Crystals always include defects. The mechanical properties of a material mainly depend on the type and density of defects. The crystal defects can change material properties such as plastic deformation limit and fracture resistance. Four types of defects exist in crystals. First type is node's faults in the crystal network. The node gap is very common defect type. In this type of defect, one node is missing. The second type of defect is dislocation which is a linear defect, see Figure 28. Another type of crystal defect is a two-dimensional defect such as twin and grain boundaries. The fourth type is a three-dimensional type or volume defect such as inclusions.

Since dislocations are involved during large plastic deformation and formability of polycrystalline metals, more detail is given below for this one-dimensional type defect.

- Dislocations defect

Dislocation is a linear defect. This defect has a great influence on the ductility of metals. The dislocation occurs during the plastic deformation. Edge dislocation and screw dislocation are the two main dislocation types, see Figure 28. The theory of dislocation was introduced by Orowan (Orowan, 1934) and Taylor (Taylor, 1934) in order to explain plasticity.

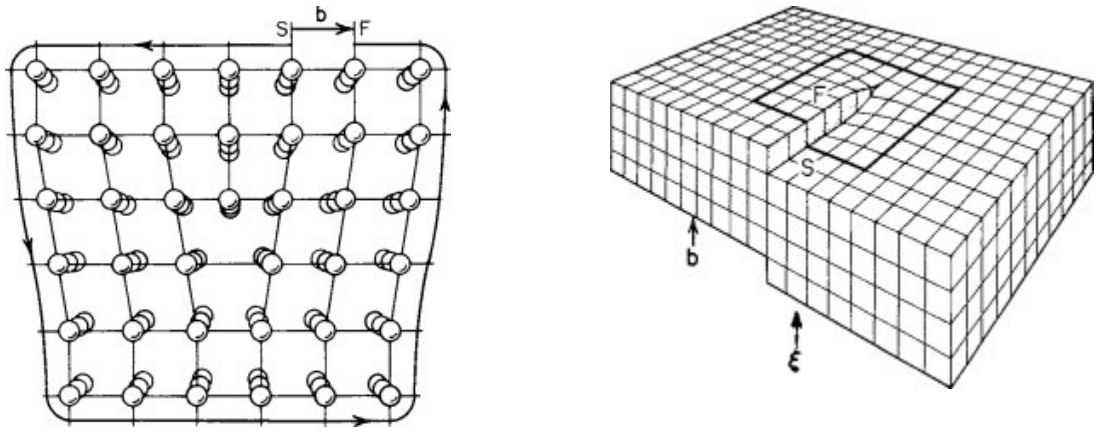

(a) **(b)**

Figure 28. Schematic of crystal dislocations

(a) Edge dislocation, (b) Screw dislocation (Hirth, 1996)

The edge dislocation is shown in Figure 28a. The edge dislocations can be observed easily as a half-plane of atoms in a lattice. The deformed nodes are located along one line. This line runs

along the top of the extra half-plane. The nodes dislocations occur inside the lattice by respecting the edge deformation. The calculation of edge dislocation stress is very complex because the lattice is not symmetric. These stresses are calculated by the equations below (Van Swygenhoven, 2002).

$$\sigma_{xx} = \frac{-\mu b}{2\pi(1-\upsilon)} \frac{y(3x^2+y^2)}{(x^2+y^2)^2} \quad (2.2)$$

$$\sigma_{yy} = \frac{\mu b}{2\pi(1-\upsilon)} \frac{y(x^2-y^2)}{(x^2+y^2)^2} \quad (2.3)$$

$$\tau_{xy} = \frac{\mu b}{2\pi(1-\upsilon)} \frac{x(x^2-y^2)}{(x^2+y^2)^2} \quad (2.4)$$

In these equations, the shear modulus is noted by μ, Burgers vector is noted by b, Poisson ratio is noted υ and the x and y are the coordinates of crystal.

The other type of dislocation is screw dislocation, see Figure 28b. In this type of dislocation, the crystal is cutting along a plane and this part is slipping parallel to the cutting plane. This boundary cut line is a screw dislocation. The stress in a screw dislocation is a shear radial stress. The equation below calculated this stress.

$$\tau_r = \frac{-\mu b}{2\pi r} \quad (2.5)$$

In this equation, the radial coordinate is noted by r.

In real plastic deformation, the dislocations are the mixture of both types. In this case, the line direction and burger vectors are neither parallel nor perpendicular. In mixed dislocation angle of line direction and burger vector is calculated by φ. For edge dislocation, we have $\varphi = \pi/2$ and for screw dislocation, we have φ=0.

The plastic deformation occurs during large strain. It makes microstructure changes. For the single crystal, the plastic deformation can occur by different mechanisms such as slip and twinning. The mechanism of twinning is not taken into account in this thesis.

Plastic deformation occurs when a large number of dislocations take place. Dislocations increase the amount of total lattice energy. The strain hardening occurs by plastic deformation. This hardening depends on the applied strain rate.

- Plastic deformation mechanism by crystallographic slip

The dislocation motion of the atoms in the single crystal is the reason of the crystallographic slip which induces plastic deformation. This crystallographic slip occurs only on specific planes and directions depending on the crystal structures. Figure 29 gives a schematic representation of crystallographic slip.

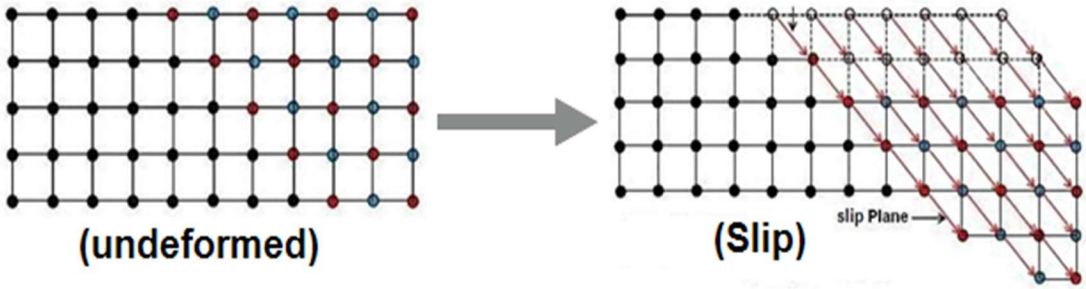

Figure 29. Representation of crystallographic slip.

- Plastic deformation mechanism by twinning

Twinning in metals may occur during metal solidification, recrystallization or plastic deformation. The twinning mechanism occurs when the crystals share the atoms in the same plane and other atoms deformed by slipping or sliding (Abdolvand and Daymond, 2012). These slips occur in certain directions and plans. It depends on the crystal systems of materials. Figure 30 represents twinning mechanisms. The twinning is affected by stacking fault energy, temperature, strain rate, etc. (Abdolvand and Daymond, 2012; Forest et al., 2002).

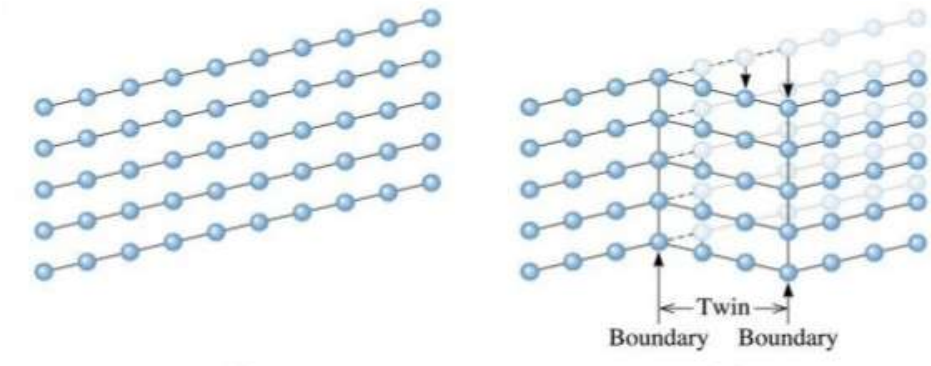

Figure 30. Representation of crystallographic twinning

2.3 Mechanical behavior of metallic materials at macroscopic scale

There are three important elements to describe the plastic behavior of materials: 1-Flow rule 2-Hardening law 3-Yield criterion.

2.3.1 Flow rule

This classical theory describes the plastic deformation vector. This vector is predicted by using the orientation and magnitude of plastic deformation. The classical flow rule is presented by Levy and Von Mises (Yu, 2006). The plastic strain rate is calculated by the equation below.

$$d\varepsilon_{ij}^{P} = d\lambda \frac{\partial f}{\partial \sigma_{ij}} \tag{2.6}$$

In this equation ε_{ij}^{p} is the plastic strain, λ is a plastic deformation factor and f is the plastic function. In this equation, dλ > 0. For isotropic material, during the work hardening, the plastic stress increases when the yield surface is expanded (Frodal et al., 2020).

2.3.2 Hardening law

The are several types of stress-strain curves for different materials such as perfectly plastic material, power-law work hardening and linear work-hardening

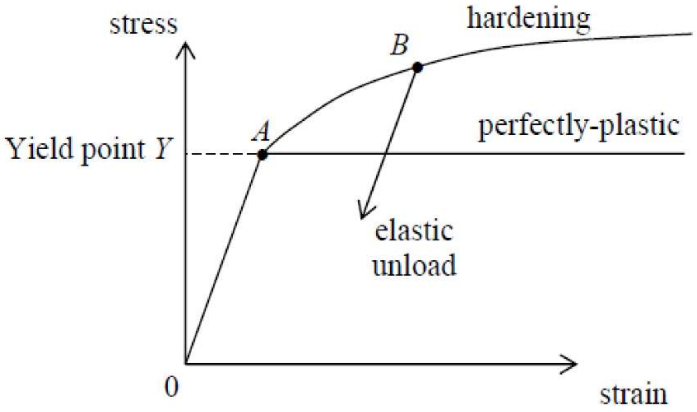

Figure 31. Stress-strain curve

The strain hardening or work hardening is the way to increase the hardness and the strength of metals by different process such as rolling or drawing. The main reason for this behavior change is the multiplication of new dislocations. Two common tests to increase hardening parameters are

bending test and the loading-unloading test (Yoshida et al., 1998; Zhao and Lee, 2001). There are two different types of hardening law: kinematic hardening and isotropic hardening, see Figure 32. The isotropic hardening works for isotropic materials. The kinematic hardening law is used for the study of the behavior of cyclic hardening (Eggertsen and Mattiasson, 2009). Kinematic hardening assumes that the yield surface remains constant in size and the surface translates in stress space with progressive yielding.

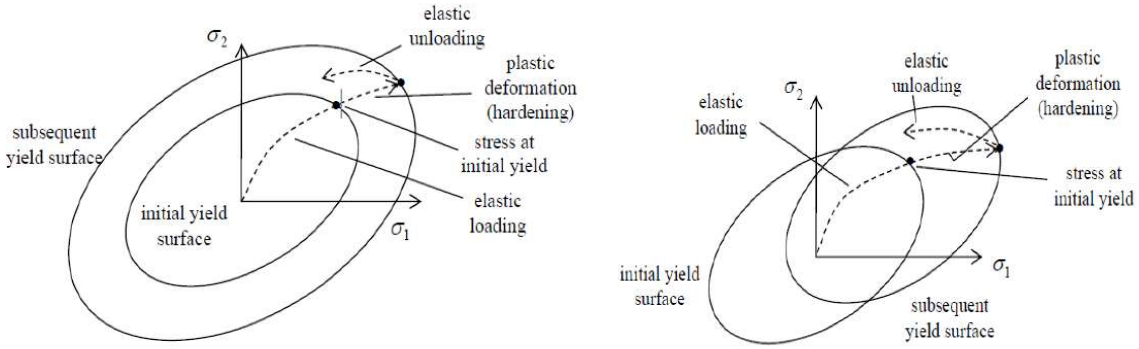

Figure 32. (a) Isotropic hardening, (b) Kinematic Hardening (Mousavi and Khaloo, 2011)

The yield function for isotropic hardening is $f(\sigma_{ij}, K_i) = \mathrm{f}_0(\sigma_{ij}) - K = 0$, where K is the hardening parameter. The yield function for kinematic hardening is written as : $f(\sigma_{ij}, K_i) = \mathrm{f}_0(\sigma_{ij} - \alpha_{ij}) = 0$, where α_{ij} is a shift-stress and σ_{ij} is normal stress.

The classical power-law equation is used as strain-hardening law (Hodge, 1957). This power law equation is represented below :

$$\sigma = K\varepsilon^n \tag{2.7}$$

In this equation, K represents the strength coefficient (MPa) and n represents the strain hardening exponent. The value of n has a large influence on work hardening. The initial work hardening is high for low values of n but it decreases very rapidly for high strain. On the other hand, for high value of n, the initial work hardening is low.

In this thesis, the evolution of the time-dependent hardening is obtained by using the classical power law:

(2.8)

where R_0, m, n, and K are respectively the hardening constant, strain rate sensitivity exponent, strain hardening exponent and strength constant (Evangelista et al., 2002).

2.3.3 Yield criterion

The limit of elasticity is defined by the yield criterion for different stress conditions during plastic deformation (Bramley, 2014). The yield point is a certain point to determine the elastic limit. From this point, the deformation is not returnable and the plastic deformation happened. On the microscopic scale, the bonds between atoms are changed (Bower, 2011). There are several types of yield criteria. Two most known isotropic criteria are the Von Mises and Tresca yield criteria. Anisotropic criteria exist such as Hill model, more details about such anisotropic criterion can be found in the literature (Hill and Orowan, 1948; Lemaitre et al., 1985).

- Von Mises yield criteria

Von Mises yield criteria is used for isotropic materials. The equation below shows general equivalent stress:

$$2\bar{\sigma}^2 = \left(\sigma_{xx} - \sigma_{yy}\right)^2 + (\sigma_{xx} - \sigma_{zz})^2 + \left(\sigma_{yy} - \sigma_{zz}\right)^2 + 6(\sigma_{xy}^2 + \sigma_{xz}^2 + \sigma_{yz}^2) \quad (2.9)$$

If the diagonal components of the stress tensor are non-zero and the other components are zero, the equivalent stress is calculated by the equation below.

$$2\bar{\sigma}^2 = \left(\sigma_{xx} - \sigma_{yy}\right)^2 + (\sigma_{xx} - \sigma_{zz})^2 + \left(\sigma_{yy} - \sigma_{zz}\right)^2 \quad (2.10)$$

If $\sigma_{zz} = 0$ (plane stress condition), the equivalent stress is calculated by the equation below.

$$\bar{\sigma}^2 = \sigma_{xx}^2 - \sigma_{xx}\sigma_{xx} + \sigma_{yy}^2 \quad (2.11)$$

- Tresca yield criteria

This criterion is presented by Tresca (Huang and Gao, 2004) which is more conservative than the Von Mises criterion. The Tresca criterion can be qualified by the equation below.

$$\frac{1}{2}\max\left(|\sigma_{xx} - \sigma_{yy}|, |\sigma_{yy} - \sigma_{zz}|, |\sigma_{zz} - \sigma_{xx}|\right) > \tau_{max} \quad (2.12)$$

Figure 33 represents these two criteria in the same diagram.

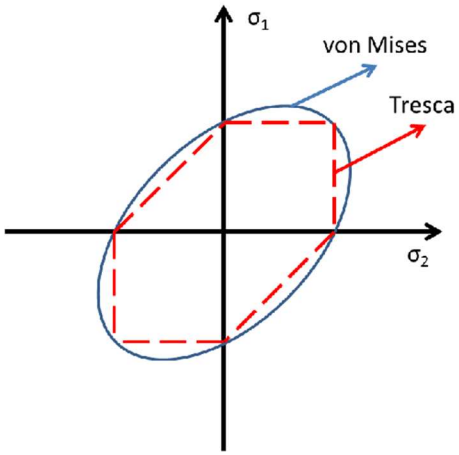

Figure 33. Von Mises and Tresca criteria diagram

2.4 Mechanical behavior of metallic materials at microscopic scale

2.4.1 Constitutive model for crystal plasticity

The decomposition of the deformation gradient, F, was investigated by Asaro and Needleman (1985) and is described below.

$$F = F^{*}F^{P}$$

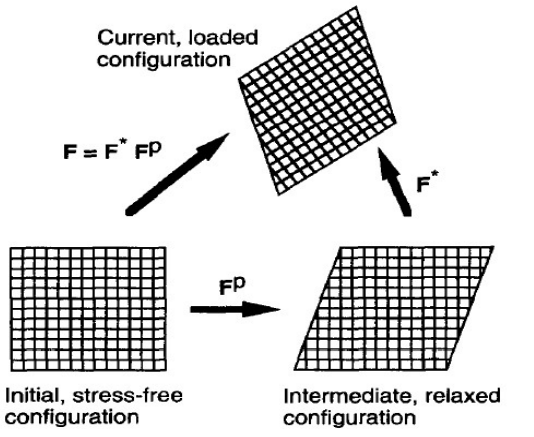

Figure 34. Decomposition of deformation gradient proposed by Asaro and Needleman (1985) (R. J. Asaro and A. Needleman, 1985)

In this equation, F^{P} is the plastic deformation gradient and F^{*} represents the rotation of the crystal lattice in which the elastic deformation is included, see Figure 34.

The microscopic velocity gradient, L, is defined by :

$$L = \dot{F}F^{-1} = L^{*} + L^{p} \tag{2.13}$$

L^{p} and L^{*} can be divided into symmetry part, strain rate, **D** and anti-symmetry part, rotation, **Ω**:

$$L^{P} = D^{P} + \Omega^{P} = \frac{1}{2}\left(L^{P} + L^{P^{T}}\right) + \frac{1}{2}\left(L^{P} - L^{P^{T}}\right) \tag{2.14}$$

$$L^{*} = D^{e} + \Omega^{*} = \frac{1}{2}\left(L^{*} + L^{*^{T}}\right) + \frac{1}{2}\left(L^{*} - L^{*^{T}}\right) \tag{2.15}$$

In these equations, D^{P} is called plastic strain rate and D^{e} is called elastic strain rate tensor. $\Omega^{P}$is called the plastic spin and Ω^{*} is called lattice spin.

The plastic velocity gradient L^{P} can be expressed as a function of the shear rate $\dot{\gamma}^{\alpha}$ and symmetric part, P^{α} and anti-symmetric part A^{α} of the Schmid tensor m^{α}:

$$L^{P} = \sum_{\alpha}^{n} \dot{\gamma}^{\alpha} \left(P^{\alpha} + A^{\alpha}\right) = \sum_{\alpha}^{n} \dot{\gamma}^{\alpha} \left(s^{\alpha} \otimes n^{\alpha}\right) = D^{P} + \Omega^{P} \tag{2.16}$$

In the previous equation (2.16), s^{α} and n^{α} are vectors representing respectively the slip direction and slip plane normal of the slip system α before deformation. These two vectors can be transformed by the rotation and become: $s^{*\alpha} = F^{*} \cdot s^{\alpha}$ and $n^{*\alpha} = F^{*} \cdot n^{\alpha}$. The Schmid tensor, m^{α}, in slip system, α is defined as: $m^{\alpha} = s^{*\alpha} \cdot n^{*\alpha} = P^{\alpha} + A^{\alpha}$

The classical visco-plastic power-law proposed by Hutchinson (1976) described the crystallographic slip mechanism and thus the induced plastic deformation:

$$\dot{\gamma}^{\alpha} = \dot{\gamma}_{0} \left(\frac{\tau^{\alpha}}{g^{\alpha}}\right) \left|\frac{\tau^{\alpha}}{g^{\alpha}}\right|^{n-1} \tag{2.17}$$

In equation (2.17), $\dot{\gamma}^{\alpha}$ represents the shear rate of a given slip system α; $\dot{\gamma}_{0}$ is the reference shear rate, τ^{α} is the corresponding resolved shear stress, g^{α} is the critical resolved shear stress and n represents the inverse rate sensitivity coefficient. The corresponding resolved shear stress is expressed as function of the symmetric part of the Schmid tensor P^{α} and the deviatoric Cauchy stress tensor S : $\tau^{\alpha} = P^{\alpha} \cdot S$.

2.4.2 Latent hardening law

During the plastic deformation of metals, the hardening occurs. Metals after this plastic deformation are more resistant. The experimental studies show the different strain hardening steps during plastic deformation. There are several numerical approaches for single crystal hardening and the description of the evolution of the critical resolved shear stress (CRSS) g^{α}. The CRSS controls the activities of the slip and twinning systems and can be updated by the hardening laws during the calculation processes.

In the latent hardening law, the increment of CRSS in system α is described by the equation below:

$$\dot{g}^{\alpha} = \sum_{\beta} H^{\alpha\beta} \left|\dot{\gamma}^{\beta}\right| \tag{2.18}$$

In this equation, $H^{\alpha\beta}$ described the n×n hardening matrix. This hardening matrix makes it possible to determine the variation of the value of the CRSS in each sliding system α. Kalidindi described this matrix as below (Kalidindi and Bronkhorst, 1992) :

$$H^{\alpha\beta} = q^{\alpha\beta} h_0 \left[1 - \frac{g^{\alpha}}{g_{sat}}\right]^{a} \tag{2.19}$$

In this equation, h_0, g_{sat} and a are the hardening law parameters. The initial hardening curve slope is presented by h_0. In this equation, if the h_0 is zero then the work hardening is equal to zero. The stress level of hardening saturation is controlled by g_{sat}. The matrix $q^{\alpha\beta}$ described the latent hardening behavior of the single crystal (Franciosi et al., 1980; Kocks, 1970; Tomé et al., 1984). When the 12 FCC slip systems are considered, the equation below describes the n×n matrix $q^{\alpha\beta}$ (Franciosi et al 1980, Tomé et al . 1984).

$$q^{\alpha\beta} = \begin{bmatrix} A & qA & qA & qA \\ qA & A & qA & qA \\ qA & qA & A & qA \\ qA & qA & qA & A \end{bmatrix} \text{ with } A=\begin{bmatrix} 1 & 1 & 1 \\ 1 & 1 & 1 \\ 1 & 1 & 1 \end{bmatrix} \tag{2.20}$$

This n×n matrix (n = the total number of considered slip and twinning systems) is populated by 1 (for coplanar systems) and q (for non-coplanar systems). The q is the latent hardening ratio usually taken between 1 and 1.4 (Franciosi et al., 1980; Kocks, 1970; Tomé et al., 1984).

2.5 Polycrystalline plasticity models

2.5.1 Main models for polycrystalline plasticity

There are several types of polycrystalline plasticity models. Only few of them are presented below.

The first type model was developed by Sachs (Sachs, 1928) which assumes that the stress tensor in each grain is proportional to the macroscopic stress tensor.

The second type model was developed by Taylor (Taylor, 1938). This model is widely used in crystal plasticity and is based on the assumption that each grain undergoes the same plastic deformation as the macroscopic polycrystalline.

The third type is Self-consistent model (Molinari et al., 1987). The advantage of this model compared to the previous two models is that they take into account the shape of the grain. The Kröner model is an elastoplastic Self-consistent model. This model is based on the results of Eshelby and the Kröner linear matrix (Eshelby, 1957; Kröner, 1961). For predicting the plastic and elastic interaction, the Hill's model based on the Eshelby formulation was introduced (Rodney Hill, 1965). The simple model with plastic interaction is presented by Berveiller and Zaoui (Berveiller and Zaoui, 1980). This model is based on Hill's model. This model is proposed for isotropic materials with spherical grain shape. Molinari proposed a self-consistent model for large viscoplastic strains (Molinari et al., 1987). This model neglects the elastic behavior of the polycrystal and predicts large deformation textures.

Garmestani proposed a statistical model to predict the micromechanical behavior of polycrystals under large viscoplastic deformations (Garmestani et al., 2001). The distribution and shape of the grains are described by the set of correlation functions in this model. The correlation function allows the investigation of the influence of each grain on the neighbour grains.

In the next part, the Taylor model is explained since it will be used in chapter 4 for CPFEM simulations.

2.5.2 Taylor model

In order to reach a better and accurate FLD determination, the prediction of crystallographic texture evolution must be taken into account in the numerical simulation.

Thus, a micromechanical model able to predict the crystallographic texture evolution must be used. In this work, the Taylor model is used for its simplicity in comparison to other models such as the well-known self-consistent model (Eshelby, 1957; Kröner, 1961). The Taylor model is also a more suitable model for large scale computing involved in the numerical simulation of complex sheet metal forming. The Taylor approach is based on the micromechanical modelling of large viscoplastic deformation of polycrystalline aggregates using the physical mechanisms of the plastic deformation. The Taylor model (also called the upper bound approximation) is proposed by Taylor in 1938 (Taylor, 1938). This model is based on the assumption of uniform strain, which means that each grain undergoes the same plastic deformation as the macroscopic domain. This model is usually formulated by the condition that the velocity gradient at the local level is equal to the macroscopic one: $\mathbf{L} = \bar{\mathbf{L}}$.

Based on the idea of Taylor (1938), several extensions have been proposed, such as the Lin model (Lin, 1957) who include isotropic elasticity. Asaro and Needleman (Asaro and Needleman, 1985) have extended the Taylor theory into elasto-viscoplastic based on the assumption of uniform deformation gradient : $\mathbf{F} = \bar{\mathbf{F}}$ (Schoenfeld et al., 1995).

2.6 Textures representation

During the plastic deformation of polycrystalline materials, the crystals are rotated and the orientations of these crystals are changed. The textures represent the grain orientation changes under plastic deformation. The mechanical deformations such as rolling, deep drawing, wire drawing, etc change the crystals orientations and anisotropy occur. The crystals textures are represented in three different ways, pole figures, inverse pole figures and orientation distribution function. The grain's orientations are defined by Euler angles presented below.

2.6.1 Euler angles

For the definition of the grain orientation, the Euler angles are used. There are 3 Eulerian angles φ_1, Φ, φ_2. The Euler angles relate the sample coordinate (X,Y,Z) to crystallographic coordinates (x,y,z) for each grain (Bunge, 1965). The rotation around the Z direction is defined by φ_1. This angle varies from zero to 2π. The rotation around the x direction is defined by Φ. This angle varies from zero to π. The rotation around the z direction is defined by φ_2. This angle varies from zero to 2π . Figure 35 shows these three angles.

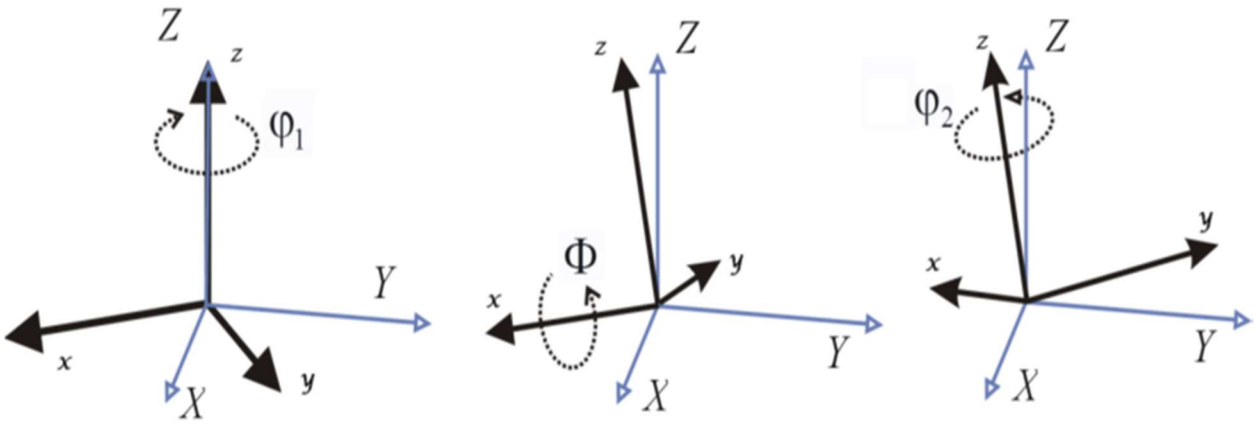

Figure 35. Representation of Eulerian angles

These three Euler angles are expressed with the following orientation matrix **a**:

$$a = a_{\varphi_2}.a_{\Phi}.a_{\varphi_1} \tag{2.21}$$

$$a = \begin{bmatrix} \cos\varphi_2 & \sin\varphi_2 & 0 \\ -\sin\varphi_2 & \cos\varphi_2 & 0 \\ 0 & 0 & 1 \end{bmatrix}.\begin{bmatrix} 1 & 0 & 0 \\ 0 & \cos\Phi & \sin\Phi \\ 0 & -\sin\Phi & \cos\Phi \end{bmatrix}.\begin{bmatrix} \cos\varphi_1 & \sin\varphi_1 & 0 \\ -\sin\varphi_1 & \cos\varphi_1 & 0 \\ 0 & 0 & 1 \end{bmatrix} \tag{2.22}$$

$$= \begin{bmatrix} \cos\varphi_1\cos\varphi_2 - \sin\varphi_1\sin\varphi_2\cos\Phi & \sin\varphi_1\cos\varphi_2 + \cos\varphi_1\sin\varphi_2\cos\Phi & \sin\varphi_2\sin\Phi \\ -\cos\varphi_1\sin\varphi_2 - \sin\varphi_1\cos\varphi_2\cos\Phi & -\sin\varphi_1\sin\varphi_2 + \cos\varphi_1\cos\varphi_2\cos\Phi & \cos\varphi_2\sin\Phi \\ \sin\varphi_1\sin\Phi & -\cos\varphi_1\sin\Phi & \cos\Phi \end{bmatrix}$$

This matrix **a** of each grain should be updated in each incremental steps following: $a_{t+\triangle t} = A^{rot}.a_t$. At each calculation step, the lattice spin Ω^* is used to update the grain orientation. The rotation angle α is obtained from the lattice spin Ω* (Lee et al., 2002) :

$$\alpha^2 = \frac{tr(\widehat{\Omega})}{2} \text{ with } \widehat{\Omega} = \Omega^*\Delta t \tag{2.23}$$

The equation below shows the orientation update matrix.

$$A^{rot} = I + \frac{\sin\alpha}{\alpha}\widehat{\Omega} + \frac{(1-\cos\alpha)}{\alpha^2}\widehat{\Omega}^2 \tag{2.24}$$

2.6.2 Different type of texture representation

The textures are represented in 3 different ways: pole figure, inverse pole figure and orientation distribution function (ODF). Each one is presented below.

- Pole figure

The most common way to represent the crystallographic orientation distribution textures is the pole figure explained in Figure 36. The pole figure is the stereographic projection sphere of grain's orientations on the specimen plane, see Figure 36a.

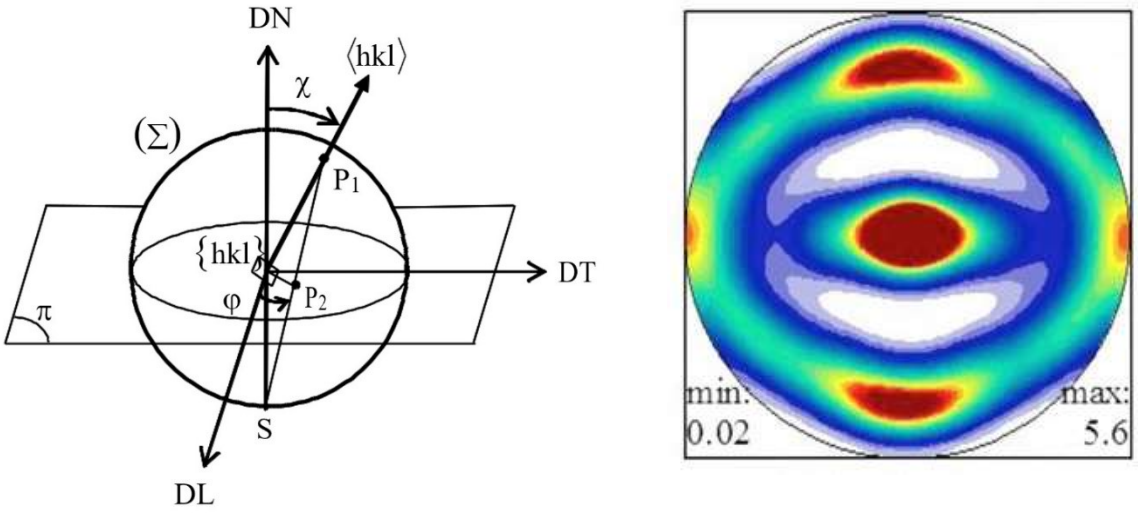

(a) (b)

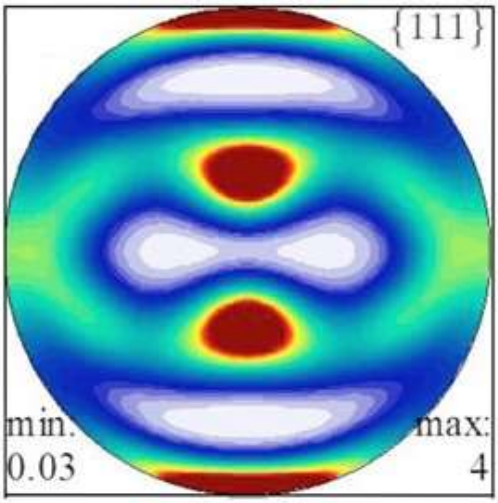

(c)

Figure 36. (a) Stereographic projection, (b)Rolling texture pole figure for BCC material, (c) Rolling texture pole figure for FCC material (Beyerlein et al., 2012)

The axes of pole figures are the same as the projection sphere. For a crystal, there is a family plane {hkl} which is cross from the projection sphere center. The normal of the family plane has contact with the sphere surface in point P_1. The point P_2 is the contact between P_1S and rolling plane. The projection of DN on a rolling plane is P_2. In this figure, χ and φ are the {hkl} crystallographic plane angles concerning the specimen axes. In the projection sphere, χ can variate between 0 and $\pi/2$ and φ can variate between 0 and 2 π.

The texture representation for plane strain compression is done by the {hkl}<uvw> system. The {hkl} plane is the crystallographic plane parallel to the rolling plane and <uvw> system is the crystallographic direction parallel to the rolling direction. There are two types of plane strain compression pole figures: copper type and brass type (Hu and Goodman, 1963). Figures 36b and 36c show these two types of pole figures. In some cases, there is a transition between these two types of pole figures. The material alloy and forming process temperature are one of the reasons for this transition.

- Inverse pole figure

The inverse pole figure (IPF) is another method to represent textures. This representation textures show the crystallographic orientation of grains parallel to the specimen plane. IPF shows certain textures with more details and accuracy. Figure 37a shows the general case of inverse pole figure. In the general case, the middle of the stereographic projection sphere divides into 24 different triangles. For example, the inverse pole figure is presented for <001> <011> <111> which is 1/24 of the main plane. Each line shows the fibers. The first study on IPF describes the deformation textures for uniaxial tension tests during compression and stretching. For an axisymmetric test, the fiber set the direction with tension and compression direction. So in a real test, the IPF is mixed of different fiber in different directions. Figure 37b shows an example of IPF in different directions. For example for FCC material such as aluminum, <111> component is the most stable but for most FCC material, the IPF is a mixture of <111> and <100> components (Dillamore and Roberts, 1965). For BCC material, the IPF is not very common to use.

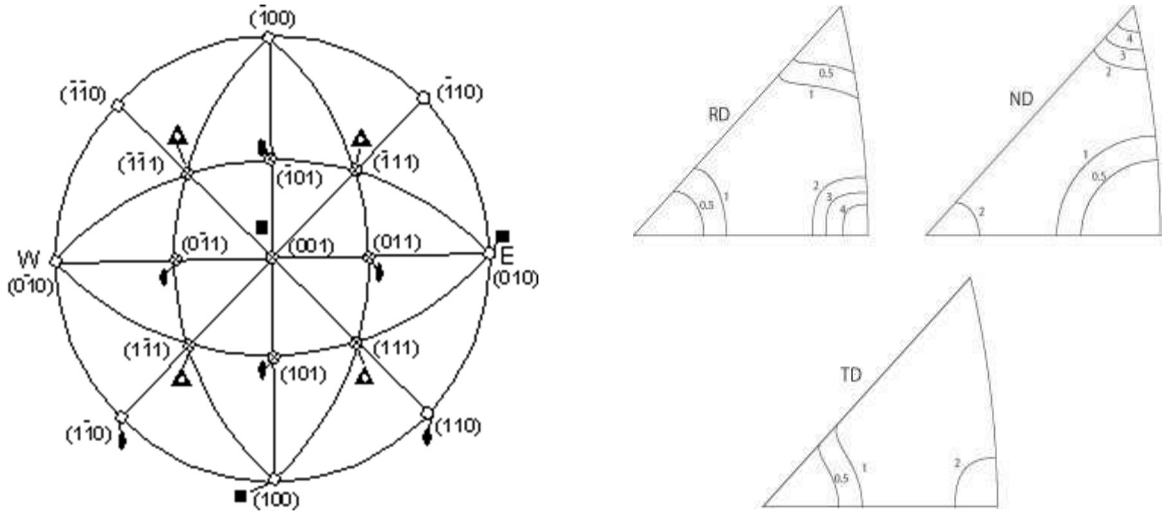

(a) (b)

Figure 37. (a) General case of inverse pole figure, (b) Inverse pole figure example

- Orientation distribution function

In polycrystalline materials, the grains are separated from each other by grain boundaries. For a complete grain behavior description, the shape and position of each grain should be studied separately. For describing the different polycrystalline structure, the statistical distribution function is used. One of the most important types of a statistical distribution is the orientation distribution function. The orientation distribution function (ODF) can describe the full 3D dimension and position of the crystals. ODF is defined by the volume fraction of grains in a certain orientation.

The orientations are presented in Euler space. In this space, each point is defined by 3 orientations φ_1, Φ, φ_2. By using these three parameters, the ODF is defined in Euler space (Kalidindi et al., 2009). Figure 38 shows the representation of three orientations in the Euler space.

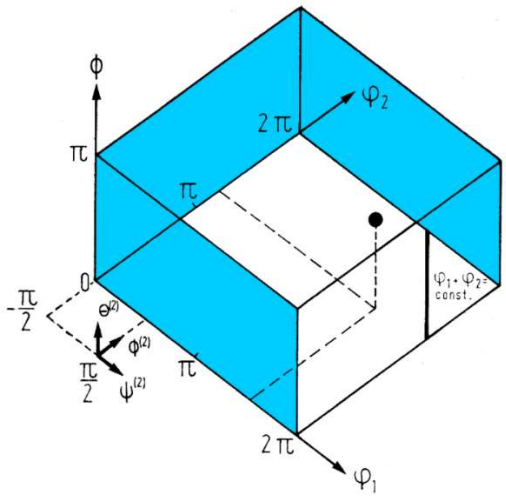

Figure 38. Representation of orientation in Euler space (Mainprice, 2004)

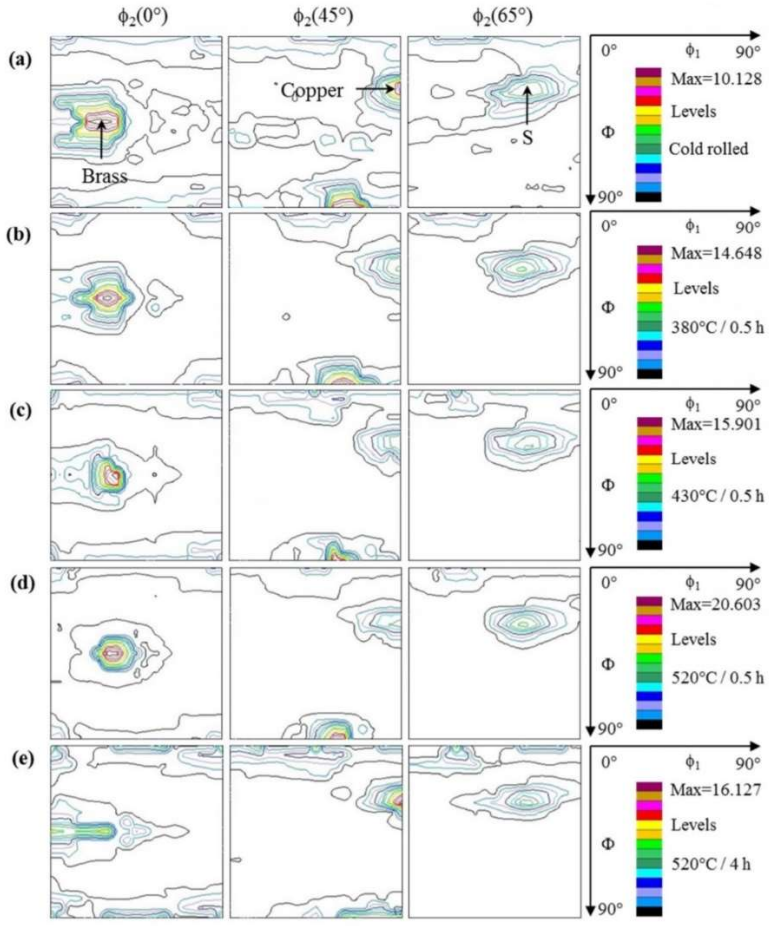

Figure 39. ODF for a cold rolling forming process at different temperatures (Yu et al., 2018)

A certain orientation is called by g. We note by ΔV(g), the volume of all the grains having an orientation between g and dg. V is the volume of the whole sample The Orientation Distribution Function is defined by the equation below.

$$\frac{\Delta V(g)}{V} = f(g)dg \qquad (2.25)$$

Figure 39 represents an example of ODF for a cold rolling process at different temperatures.

2.6.3 Experimental measurement of crystallographic texture

The experimental evaluation of texture using X-ray diffraction by a monochromatic beam is called X-ray crystallography. In this method, the atomic and molecular structure of a crystal is investigated. A 3-dimensional picture of a crystal is determined by measuring the diffracted beams angles and intensities (Frampton et al., 2000). An incident beam will be reflected in all crystals where the direction between the incident and reflected beam is parallel. X-ray diffraction (XRD) is based on equation Bragg's law (Bragg and Bragg, 1913).

$$n\lambda = 2d_{hkl} \sin \theta_{hk} \qquad (2.26)$$

In this equation, the wavelength is represented by λ (μm), n represents a positive integer, d (mm) is the distance between diffracting planes and θ is beam reflected angle. Figure 40 shows the XRD machine.

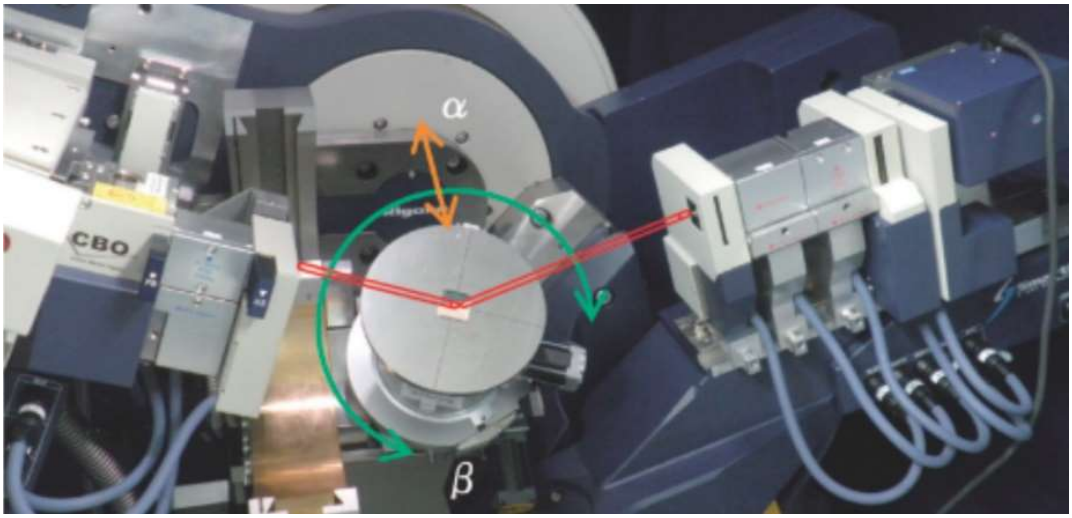

Figure 40. Parallel beam reflection method (Nagao and Kagami, 2011)

The equations below show the diffraction intensity peaks. The diffraction intensity is determined by studying the atom's arrangement in the crystal (Ruska et al., 1979).

$$I_{hkl} = I_0 . R . \frac{\Delta V}{V} \quad (2.27)$$

$$I_{hkl} \propto |F_{hkl}|^2 \quad (2.28)$$

$$F_{hkl} = \sum_{j=1}^{m} N_j f_j \exp\left[2\pi i(hx_j + ky_j + lz_j)\right] \quad (2.29)$$

In this equation, F_{hkl} is the structure factor, I_0 is the initial intensity of the incident beam, N_j is the fraction of every occupied position of atom j and fj is the scattering factor.

The intensity can be written in another form.

$$I_{hkl} = N_{hkl} . P_{hkl}(\alpha\beta) \quad (2.30)$$

In this equation, pole density is noted by P_{hkl} and the normalized function is represented by N_{hkl} and α (pole distance normal), β (azimuth normal) are shown in Figure 41 which show the X-ray reflection method.

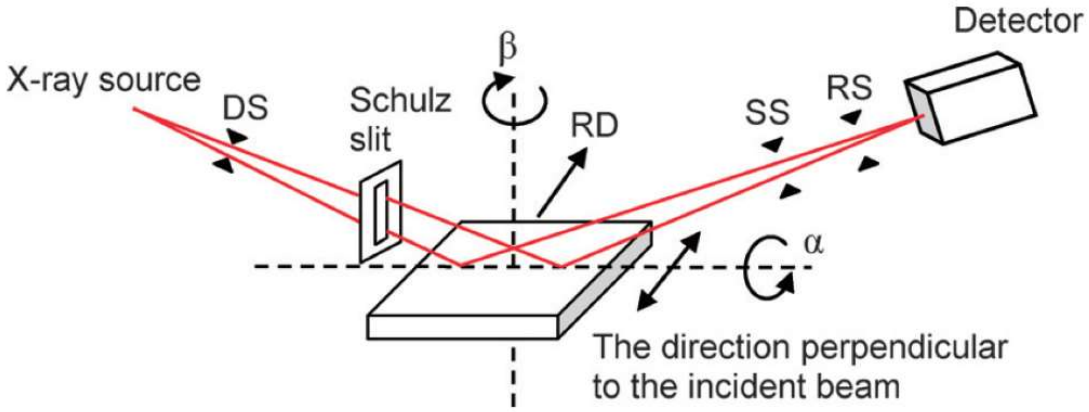

Figure 41. X-Ray reflection method (Nagao and Kagami, 2011)

For a complete type of XRD, both types of diffraction, reflection and transmission should be combined.

X-ray diffraction system consists of 3 main parts: X-ray source, sample holder and X-ray detector. The X-ray source diffracts the beams with a special wavelength for different materials (Cu, Al, Fe,

etc). The sample holder can turn the sample in different directions. The X-ray detector records the intensity of the reflected X-rays. In the next step, the recorded signals are converted to the data and the results are shown on a monitor.

In this thesis, this X-ray diffraction method will be used for the determination of texture of studied metals: St-14 mild steel and Al6061 commercial aluminum. The measured experimental textures for these metals are presented in chapter 5.

References

Abdolvand, H, Daymond, M. R. (2012). Internal strain and texture development during twinning: Comparing neutron diffraction measurements with crystal plasticity finite-element approaches, Acta Materialia, 60(5), 2240–2248. https://doi.org/10.1016/j.actamat.2012.01.016

Asaro, R. J., Needleman, A. (1985). Overview no. 42 texture development and strain hardening in rate dependent polycrystals, Acta Metallurgica, 33(6), 923–953.

Austin, R. A., McDowell, D. L. (2011). A dislocation-based constitutive model for viscoplastic deformation of fcc metals at very high strain rates, International Journal of Plasticity, 27(1), 1–24. https://doi.org/10.1016/j.ijplas.2010.03.002

Berveiller, M. (1980). Généralisation du problème de l'inclusion et application à quelques problèmes d'élastoplasticité des matériaux hétérogènes, J. Mécanique 19, No. 2, 343-361.

Beyerlein, I. J., Mara, N. A., Wang, J., Carpenter, J. S., Zheng, S. J., Han, W. Z., Pollock, T. M. (2012). Structure-property-functionality of bimetal interfaces, Jom, 64(10), 1192–1207. https://doi.org/10.1007/s11837-012-0431-0

Bragg, P. W. H., Bragg, W. L. (1913). 7, 17, 428–438.

Bramley, A. (2014). Yield Criteria BT - CIRP Encyclopedia of Production Engineering, Springer, 1315–1318. https://doi.org/10.1007/978-3-642-20617-7_16689

Bunge, H. J. (1965). Einige Bemerkungen zur Symmetrie verallgemeinerter Kugelfunktionen, Wiss, 7, 351–360.

Chin, G.Y , Hosford, W. . (1969). Accommodation of constrained deformation in f.c.c metals by slip and twinning, 309(April), 433–456.

Dillamore, I. L, Roberts, W. T. (1965). Preferred orientation in wrought and annealed metals, Metallurgical Reviews, 10(1), 271–380. https://doi.org/10.1179/mtlr.1965.10.1.271

Eggertsen, P.A, Mattiasson, K. (2009). Material modelling for accurate springback prediction, International Journal of Material Forming, 2, 793–796. https://doi.org/10.1007/s12289-009-0507-8

Eshelby, J. D. (1957). The determination of the elastic field of an ellipsoidal inclusion and related problems, Proceedings of the Royal Society of London, Series A. Mathematical and Physical Sciences, 241(1226), 376–396.

Forest, S., Parisot, R and Paris, M. De. (2002). Torino2000, 58(1), 11.

Frampton, C. S., Knight, K. S., Shankland, N, Shankland, K. (2000). Single-crystal X-ray diffraction analysis of pyrene II at 93 K, Journal of Molecular Structure, 520(1–3), 29–32.

Frodal, B. H., Morin, D., Børvik, T, Hopperstad, O. S. (2020). On the effect of plastic anisotropy strength and work hardening on the tensile ductility of aluminium alloys, International Journal of Solids and Structures, 188–189, 118–132. https://doi.org/https://doi.org/10.1016/j.ijsolstr.2019.10.003

Garmestani, H., Lin, S., Adams, B. L., Ahzi, S. (2001). Statistical continuum theory for large plastic deformation of polycrystalline materials, Journal of the Mechanics and Physics of Solids, 49(3), 589–607. https://doi.org/10.1016/S0022-5096(00)00040-5

Hill, R. (1965). A self-consistent mechanics of composite materials, Journal of the Mechanics and Physics of Solids, 13(4), 213–222.

Hill, R, Orowan, E. (1948). A theory of the yielding and plastic flow of anisotropic metals, Proceedings of the Royal Society of London. Series A. Mathematical and Physical Sciences, 193(1033), 281–297. https://doi.org/10.1098/rspa.1948.0045

Hirth, J. P. (1996). Chapter20-dislocations, Physical Metallurgy, 1831–1875. https://doi.org/https://doi.org/10.1016/B978-044489875-3/50025-9

Hodge, P. G. (1957). A new method of analyzing stresses and strains in work hardening plastic solids, J. Appl. Mech., 24, 482–483.

Hu, H, Goodman, S. R. (1963). Cube texture in austenitic stainless steel, Transactions of the metallurgical society of aime.

Huang, W, Gao, X. Y. (2004). Tresca and von Mises yield criteria: A view from strain space. Philosophical Magazine Letters, 84, 625–629. https://doi.org/10.1080/09500830512331325091

Kalidindi, S. R, Bronkhorst, C. A. (1992). Crystallographic Deformation Texture Processing Evolution in Bulk, Journal of the Mechanics and Physics of Solids, 40(3), 537–569. https://doi.org/10.1016/0022-5096(92)80003-9

Kalidindi, S. R., Knezevic, M., Niezgoda, S., Shaffer, J. (2009). Representation of the orientation distribution function and computation of first-order elastic properties closures using discrete Fourier transforms, Acta Materialia, 57(13), 3916–3923. https://doi.org/https://doi.org/10.1016/j.actamat.2009.04.055

Kröner, E. (1961). Zur plastischen verformung des vielkristalls, Acta Metallurgica, 9(2), 155–161.

Lemaitre, J., Chaboche, J.L., Benallal, A., Desmorat, R. (1985). Mécanique des matériaux solides (Vol. 2), Dunod Paris.

Lin, C. C. (1957). Note on Garabedian's Paper Numerical Construction of Detached Shock Waves, Journal of Mathematics and Physics, 36(1–4), 206–209. https://doi.org/10.1002/sapm1957361206

Lord, E. A., Ranganathan, S. (2004). The γ-brass structure and the Boerdijk-Coxeter helix, Journal of Non-Crystalline Solids, 334–335(February 2018), 121–125. https://doi.org/10.1016/j.jnoncrysol.2003.11.069

Mainprice, D. (2004). Crystal Preferred Orientation.

Molinari, A., Canova, G. R., Ahzi, S. (1987). A self consistent approach of the large deformation polycrystal viscoplasticity, Acta Metallurgica, 35(12), 2983–2994. https://doi.org/https://doi.org/10.1016/0001-6160(87)90297-5

Nagao, K. , Kagami, E. (2011). VII. Pole figure measurement, The Rigaku Journal, 27(2), 6–14.

Orowan, E. (1934). Die mechanischen Festigkeitseigenschaften und die Realstruktur der Kristalle, Zeitschrift Für Kristallographie-Crystalline Materials, 89(1–6), 327–343.

Ruska, J., Gauckler, L. J., Lorenz, J., Rexer, H. U. (1979). The quantitative calculation of SiC polytypes from measurements of X-ray diffraction peak intensities, Journal of Materials Science, 14(8), 2013–2017. https://doi.org/10.1007/BF00551044

Sachs, G. (1928). Plasticity problems in metals, Trans. Faraday Soc, 24(0), 84–92. https://doi.org/10.1039/TF9282400084

Schoenfeld, S. E., Ahzi, S, Asaro, R. J. (1995). Elastic-plastic crystal mechanics for low symmetry crystals, Journal of the Mechanics and Physics of Solids, 43(3), 415–446. https://doi.org/10.1016/0022-5096(94)00065-D

Taylor, G.I. (1934). The Mechanism of Plastic Deformation of Crystals,Part I, Theoretical. Proceedings of the Royal Society of London Series A, 145(855), 362–387. https://doi.org/10.1098/rspa.1934.0106

Taylor, G.I. (1938). Plastic strain in metals, Our. Inst. Metals, 62, 307–324. http://ci.nii.ac.jp/naid/10007428664/en/

Toroghinejad, M. R., Dini, G. (2006). Effect of Ti-microalloy Addition on the Formability and Mechanical Properties of a Low Carbon (ST14) Steel, International Journal of ISSI.

Van Swygenhoven, H. (2002). Grain Boundaries and Dislocations, Science, 296(5565), 66 – 67. https://doi.org/10.1126/science.1071040

Yoshida, F., Urabe, M., Toropov, V.V. (1998). Identification of material parameters in constitutive model for sheet metals from cyclic bending tests, International Journal of Mechanical Sciences, 40(2), 237–249. https://doi.org/https://doi.org/10.1016/S0020-7403(97)00052-0

Yu, H.-S. (2006). Perfect Plasticity. Plasticity and Geotechnics, 69–85.

Yu, X., Dai, H., Li, Z., Sun, J., Zhao, J., Li, C., Liu, W. (2018). Improved Recrystallization Resistance of Al–Cu–Li–Zr Alloy through Ce Addition, Metals, 8, 1035. https://doi.org/10.3390/met8121035

Zhao, K., Lee, J. (2001). Generation of Cyclic Stress-Strain Curves for Sheet Metals, Journal of Engineering Materials and Technology-Transactions of The Asme,*123*. https://doi.org/10.1115/1.1395021

Chapter 3

Numerical FLD determination using biaxial and Nakajima tests for FCC and BCC metals: application to deep drawing simulation

3.1 Introduction

Necking, strain localization and failure occurring during sheet metal forming lead to scrap defective products and increase manufacturing costs. Numerical simulation of forming processes, and particularly simulation of deep-drawing operations, is used to avoid such additional costs by helping the designers to predict such critical physical phenomena. Main experimental, analytical and numerical approaches have been presented in Chapter 1.

In this chapter, two numerical approaches enlightened in Chapter 1 are compared to predict FLD. The first one is derived from Marciniak-Kuczynski (M-K) method. A 3D FEM modeling of biaxial test including an initial band with reduced thickness is implemented to predict localized necking. The second method is based on a FEM simulation of the Nakajima test. Fundamental differences between these models are discussed and FLD obtained with these approaches are compared.

FLD is used to compare the formability of different materials or to predict the criticality at necking, or even at failure. In industry, an approximation of strain localization risk is given by comparing an experimental or a numerical FLD and the strain states for each elementary volume constituting a metal sheet during deep-drawing operations. An example of this method is presented in the third part of this chapter.

3.2. FEM model for FLD determination using biaxial test with initial defect

In this part, a numerical Marciniak-Kuczynski will be developed and applied to the prediction of formability for St-14 mild steel and Al6061 aluminum alloys.

3.2.1 FEM Marciniak-Kuczynski criterion and associated parameters

Introduced by Marciniak-Kuczynski in 1967 (Marciniak and Kuczyński, 1967), the M-K model is a multi-zone analytical model dedicated to the prediction of strain localization. During loading, material instability phenomena are assumed to occur in the region of the sheet affected by an initial geometrical defect. This defect is modeled by a band of reduced thickness but may represent any kind of heterogeneous behavior. By convention, the safe and defect parts of the sheet will be respectively called zone A and zone B in the following. Strain localization is considered to occur when the plastic deformation is concentrated in the defect zone, i.e. when the plastic strain ratio (or its time derivative) in zones A and B reaches a threshold value. The classical M-K model can

be written with an analytical way, leading to an analytical formulation of the localized necking criterion. Efficient implementations of this criterion are obtained for phenomenological material models (Müschenborn and Sonne, 1975).

Another approach is chosen in this part in order to obtain a versatile implementation, adaptable to a large class of materials modeling, including models based on crystal plasticity. A fully 3D finite element model of a planar metal sheet with an initial defect is implemented in Abaqus implicit software. Parametric studies are given as illustrations of this model to investigate the effect of different user-defined M-K parameters, such as the initial orientation of the band θ_0 and the initial thickness ratio, f_0, on the FLD for BCC and FCC polycrystalline materials.

For the finite element model of Marciniak-Kuczynski, a 180×180 mm metal sheet with 1 mm thickness is used to be consistent with experimental data that will be presented in Chapter 5. This metal sheet has an imperfection zone with a 14 mm width. Various initial thickness ratio $f_0 = \frac{t_0^B}{t_0}$ are taken, where t_0 is the initial thickness of the sheet and t_0^B the initial thickness inside the band, as presented in Figure 42. Common values of the initial thickness ratio, f_0, range between 0.90 and 0.999 (Hashemi et al., 2012). Then, for each loading path, different initial orientations of the band have to be simulated to detect the critical initial orientation of the band that leads to lower the formability prediction.

Simulations with initial angles θ_0 equal to 0°, 20° and 40° are given to illustrate the model. These simulations are done for eleven values of the loading force ratio α ranging between 0 and 1, with $\alpha = \frac{F_2}{F_1}$. The initial loading is corresponding to 400 MPa. These loadings are applied to the edges.

Strain and stress states are then computed and stored for each loading step for two specific elements located in the homogeneous regions of the stress and strain fields of zones A and B. Observation of relative evolutions of the mechanical fields inside and outside the imperfection band shows a superior increase of the strain rate in the band. This phenomenon leads to a concentration of the strain inside the band and then to the strain localization.

Different localization indicators may be defined to predict localization. In this part, the out-of-plane strain ratio is used as a strain localization measurement. Localization is predicted when this ratio exceeds a user-predefined value S_{MK} proposed by Evangelista et al. (2002):

$$S_{MK} = \frac{\epsilon_{33}^{A}}{\epsilon_{33}^{B}} \tag{3.1}$$

In equation (3.2), ϵ_{33}^{B} and ϵ_{33}^{A} represent the deformation in the thickness in zone B and the thickness in zone A, respectively. When S_{MK} is decreasing less than 0.8, the simulation is stopped and minor and major strains for this loading ratio are stored.

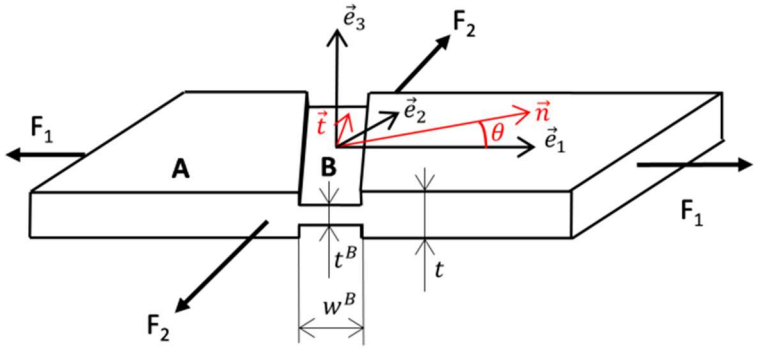

Figure 42. Definition of zone A and zone B in M-K model (Altmeyer et al., 2010)

A 21600 linear hexahedral mesh based on C3F8R elements mesh is built for this model. The mesh size in the imperfection zone B is 50% smaller than in the perfect zone A, as shown in Figure 43. Different values of the initial thickness ratio are considered, with f_0 chosen equal to 0.90, 0.95 and 0.99. The boundary conditions for this model are defined. One corner is fixed, two adjacent out-of-plane faces are free to move in one direction, respectively the principal directions 1 and 2, while a normal force is applied on the remaining out-of-plane faces. The loading ratio, with $\alpha = \frac{F_2}{F_1}$, defines the relations between the applied forces in directions 1 and 2. To represent loads from uniaxial to equibiaxial tension, the loading ratio is prescribed from 0 to 1 with 10 increments. Initial corresponding loading of 400 MPa is applied to be consistent with the experimental procedure defined in Chapter 5. These boundary conditions in this model are illustrated in Figure 43.

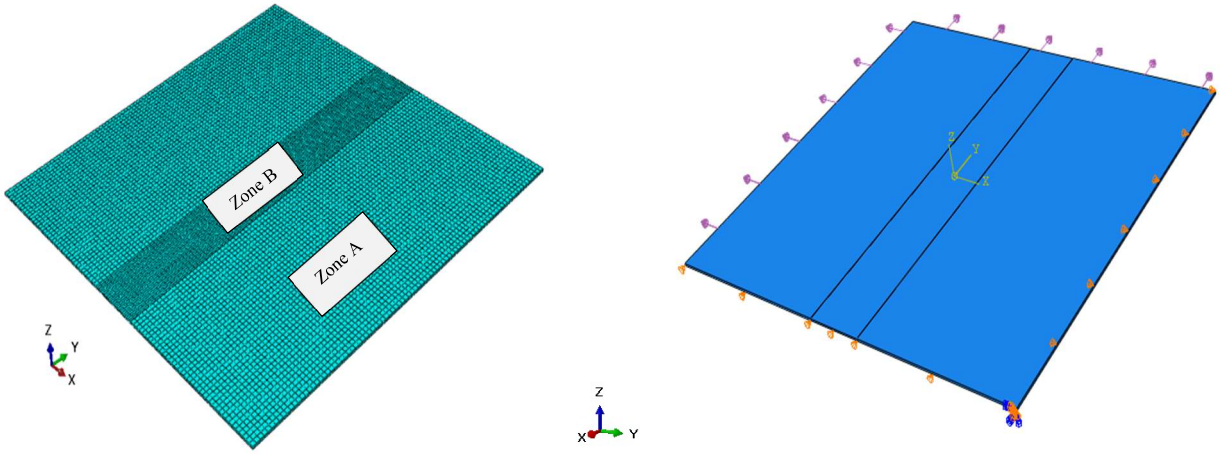

Figure 43. Initial mesh and boundary conditions for Marciniak-Kuczynski FEM model

After the geometry being created in Abaqus, the material behavior and the boundary conditions are applied on the metal sheet. After meshing operations, job is run for each loading ratio. Strain and stress states are stored for two specific elements in zones A and B while threshold value S_{MK} is reached. When the criterion is passed, the strain localization is predicted, critical minor and major strain values are registered for each loading ratio value. These values are then used to plot the corresponding FLD.

3.2.2 Material parameters for BCC and FCC metal sheet simulation

Two materials are used to illustrate FEM Marciniak-Kuczynski model. These materials are selected because they are used by our industrial partners for some of their machining, deep drawing and stamping applications. The first material is a commercial low carbon St14 mild steel, composed of Iron, Carbon, Copper, Manganese, Phosphorous, Sulfur, Nitrogen. This mild steel is also easy to weld. The second material is an alloy of aluminum Al6061 with good surface finishing, good corrosion resistance to the atmosphere and seawater resistance properties. It is also quite suitable for welding. Most other aluminum alloys are difficult to weld due to their chemical composition (Ramesh et al., 2011). The chemical composition of both materials and their hardening properties according to formula 2.8 are respectively given in Table 2 and Table 3.

C	Si	Mn	P	S	Al	N (ppm)
0.02	0.004	0.222	0.007	0.004	0.058	30
BCC - St14 mild steel						

Al	Cr	Cu	Fe	Mg	Mn	Other
0.958	0.035	0.015	0.007	0.004	0.015	0.0015
FCC - Al6061 alloy of aluminum						

Table 2. Chemical composition of St14 mild steel (BCC) and Al6061 alloy of aluminum (FCC) materials (Toroghinejad and Dini, 2006; Rahmatabadi et al., 2018)

Material	E *GPa*	ν	ρ *kg/m^3*	n	K *(MPa)*	m
St14	210	0.30	7860	0.19	660	0.012
Al6061	68.9	0.33	2698	0.23	205	0.009

Table 3. Mechanical properties of St14 mild steel (BCC) and Al6061 alloy of aluminum (FCC) materials, (Evangelista et al., 2002; Technical datasheet, Robert Laminage, 2008)

3.2.3 FLD determination using FEM model of biaxial test with initial defect

3.2.3.1 Effect of initial thickness ratio on FLD

In this part, the effect of the initial thickness ratio, f_0, on forming limit diagram is investigated. St14-mild steel material is chosen for this study. The value of f_0 ranges between 0.90 and 0.99.

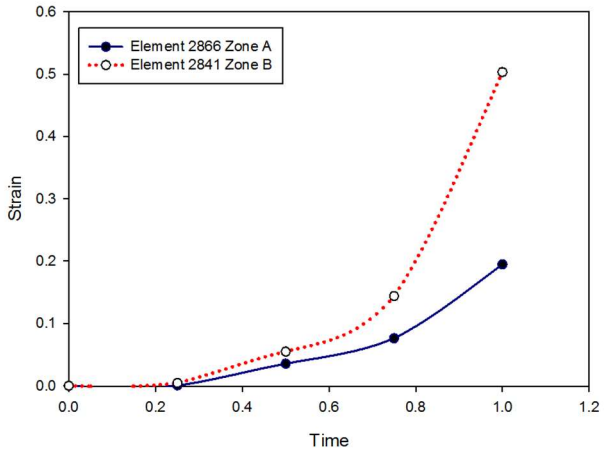

Figure 44. Strain-Time (s) curves for f_0=0.95, α = 0.5, θ = 0°

The initial thickness ratios are chosen for this study equal to 0.90, 0.95 and 0.99. 11 values of the loading ratio α are simulated. One may observe that the strain values are higher in zone B than in zone A, as predicted by the model. The thickness in zone B reduces faster than in zone A, leading to necking in zone B. Results for band orientations equal to 0° and initial thickness ratio f_0=0.95 are shown in Figure 44, using elements in the middle of zones A (element number=2866) and B (element number=2841). The current thickness ratio is actualized for each loading increment and the job is stopped when the threshold value is reached. Results are shown in Figure 45 for a specific loading ratio α and an initial orientation of the band collinear with the minor loading direction and different initial thickness ratios.

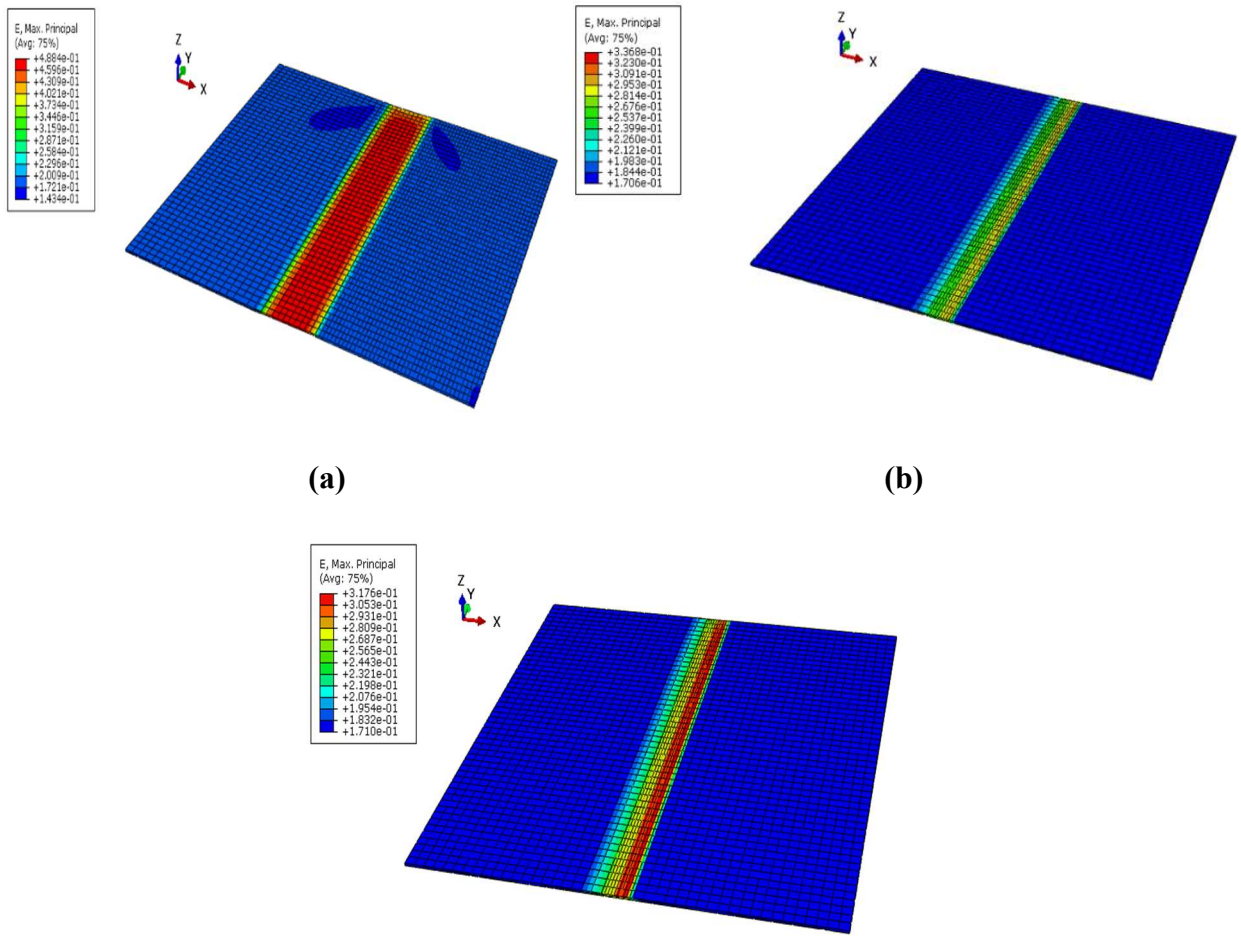

(a) **(b)**

(c)

Figure 45. Major strain for St-14 mild steel sheet (α=0.5)

f_0=0.90 (a), f_0=0.95 (b), f_0=0.99 (c)

FLD is then obtained for each investigated value of f_0, and results are synthesized in Figure 46.

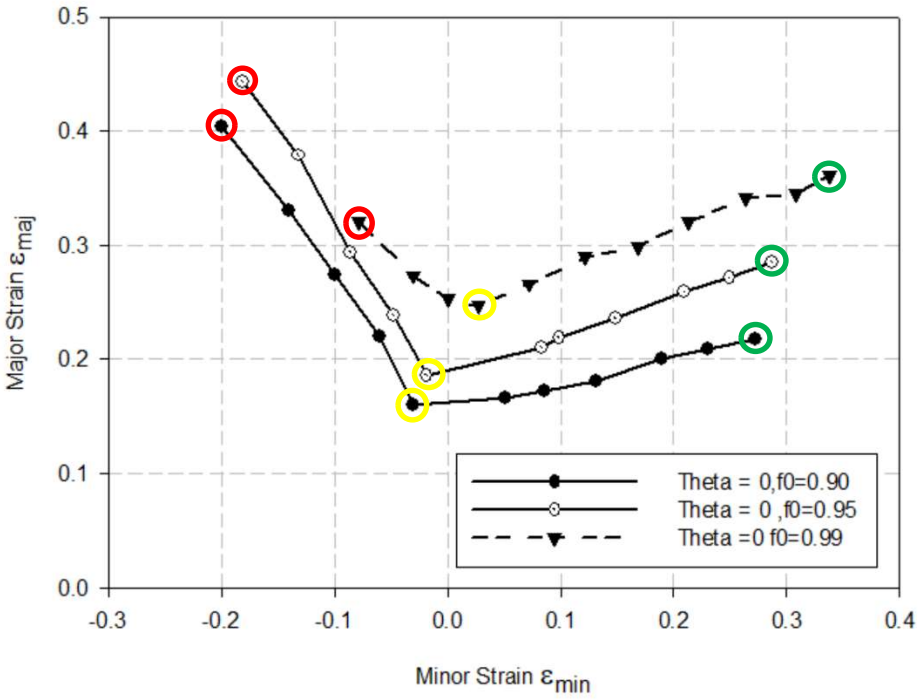

Figure 46. Numerical FLD obtained with a FEM based M-K model for different values of f_0

Increasing f_0 leads to higher formability predictions for BCC St-14 material. Effects of f_0 choice on FLD are shown for loading paths close to uniaxial (red circle on Figure 7), plane (yellow circle) and equibiaxial (green circle) tensions. For $\alpha = 0$, the maximum major strain occurs for $f_0 = 0.95$ and the maximum minor strain occurs for $f_0 = 0.9$. At FLD_0 (near yellow point), the formability predictions are also higher when f_0 is increased. The highest values of minor and major strain occur for $f_0 = 0.99$. The same observations are made for the equibiaxial expansion point (green point).

3.2.3.2 Effect of the initial orientation of the band on FLD

The effect of the initial orientation of the band on FLD is now analyzed. Three initial orientations θ_0 are investigated: 0°, 20° and 40°. Simulations are done for every value of the loading ratio α to obtain FLD associated to each initial orientation of the band. A constant ratio f_0 equal to 0.9 is prescribed for every simulation. Some results are drawn in Figure 47. One may notice that the maximum strain value is increased by increasing θ values for uniaxial tension. Some convergence issues are obtained for the simulations with θ values higher to 45°.

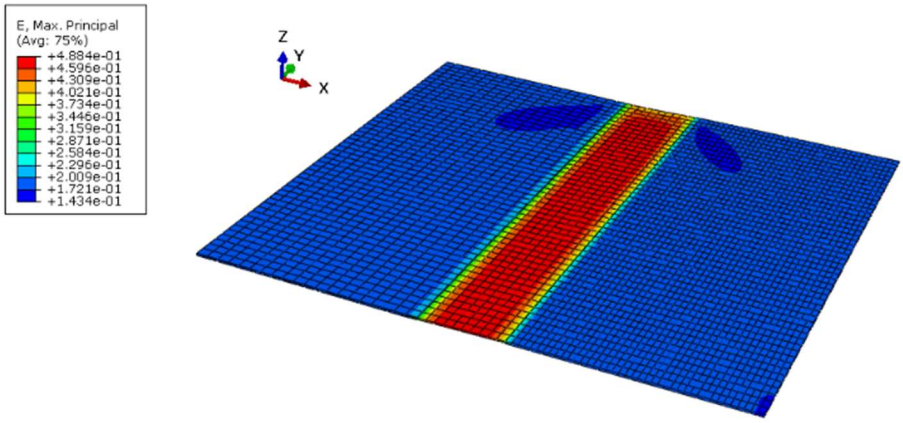

(a)

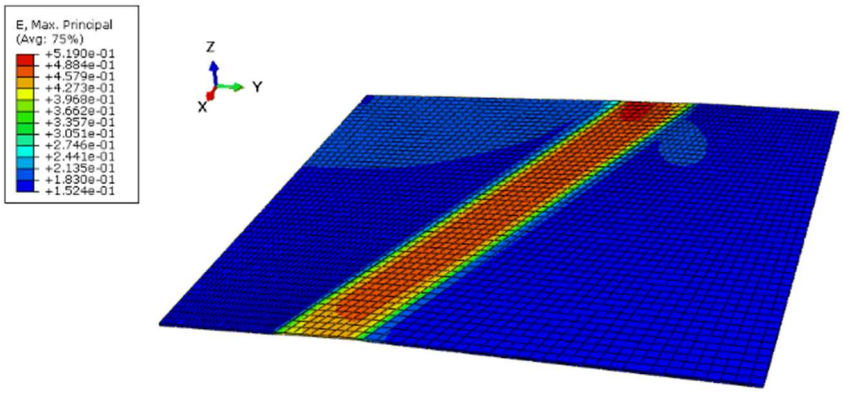

(b)

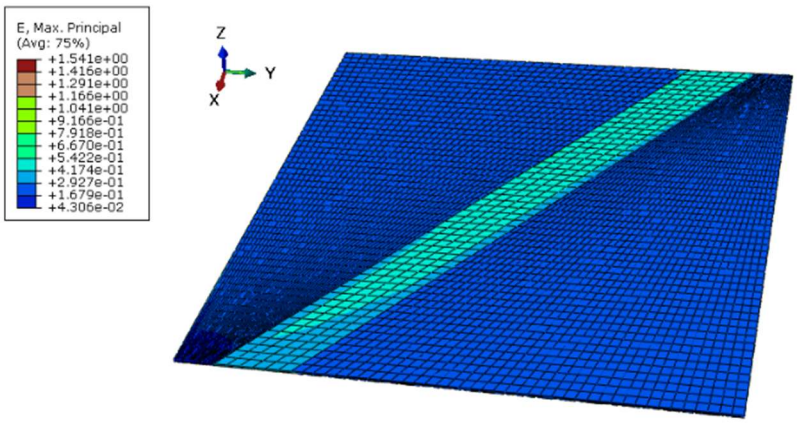

(c)

Figure 47. Major strain for St-14 metal sheet (α=0.5) for (a) θ = 0°, (b) θ =20° and (c) θ =40°

Figure 48 represents the numerical FLD obtained with the FEM-based M-K model for different values of orientation band θ for St-14 mild steel. One may observe from these curves that the left side of FLD is influenced by the initial orientation of the band.

At the uniaxial tension point, formability predictions decrease by increasing θ. The critical state is then predicted maximum for θ = 40°. Near plane tension point and in the expansion domain, influence of the initial orientation of the band becomes unnoticeable.

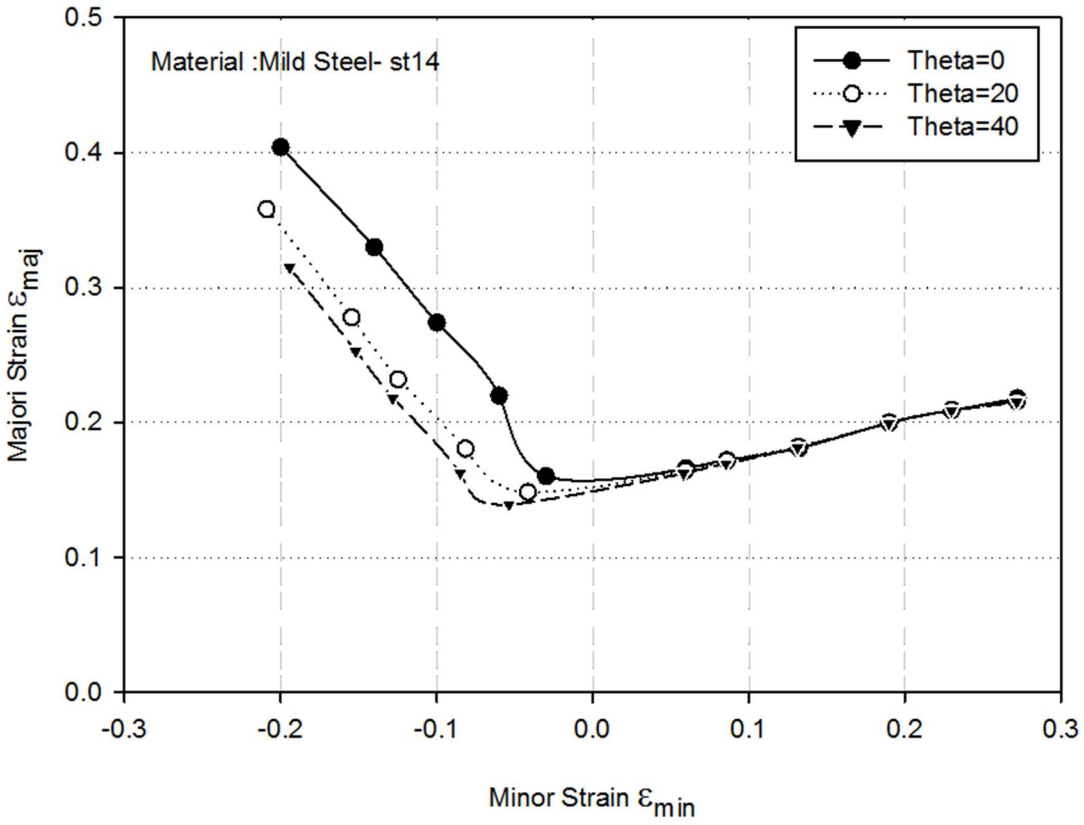

Figure 48. Numerical FLD obtained with a FEM based M-K model for different values of orientation band θ for St-14 mild steel

3.2.3.3 Effect of polycrystalline materials structures on FLD

In this part, the effect of polycrystalline materials structures is investigated by using two materials: Al6061 and St-14. Al6061 is a commercial alloy of aluminum and St-14 is a commercial low carbon mild steel. Al6061 has a FCC structure and St-14 has a BCC structure. The M-K parameters f_0 and θ are assumed equal to 0.95 and 0°. The finite element simulations for these two materials are shown below.

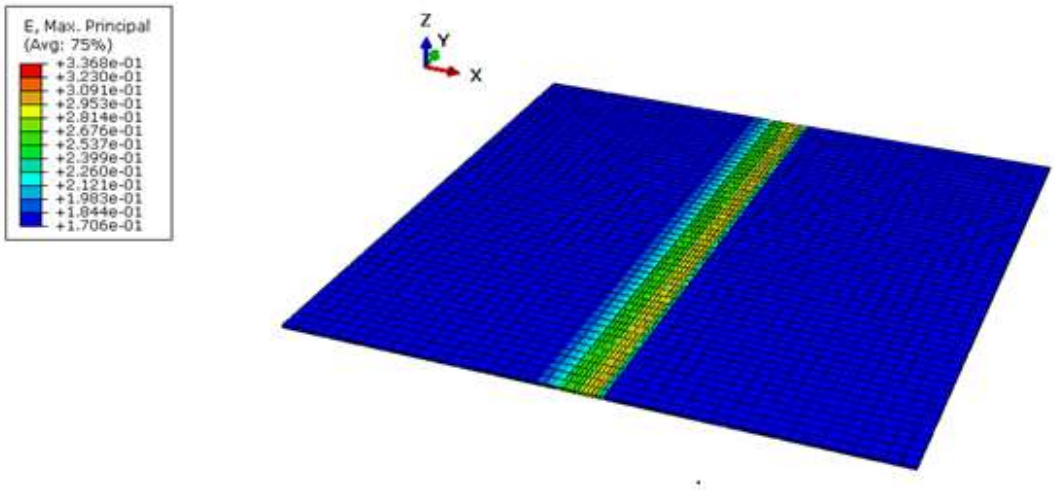

(a)

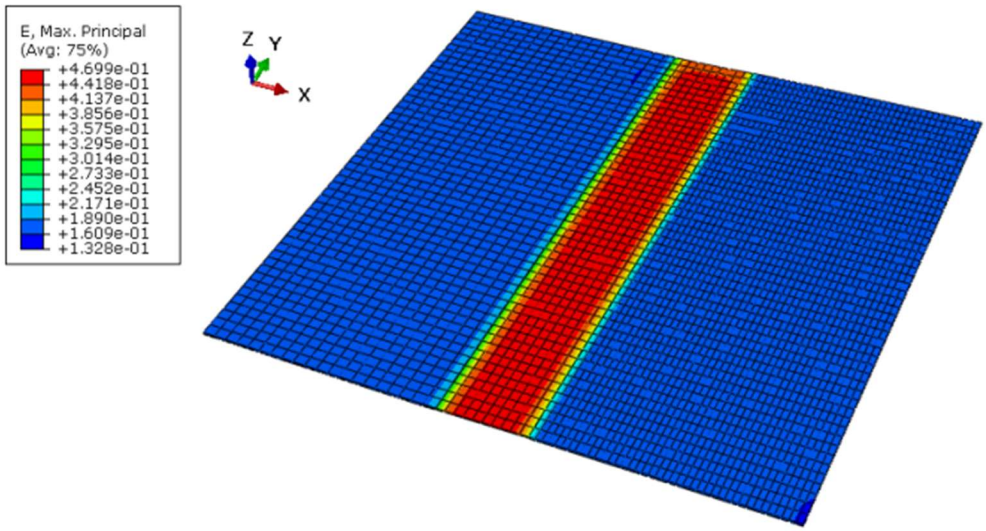

(b)

Figure 49. Major strain for α=0.5 and θ = 0° for St-14 sheet (a) and Al6061 sheet (b)

In these simulations, the maximum strains concentrate on the imperfection zone. Figure 50 shows the FLD for St-14 (BCC) and Al6061 (FCC) materials. Figure 50 shows that in this study, BCC material formability is a little higher than the FCC material. This result is consistent with numerical literature results (Inal et al., 2005). From this FLD, it is understood that the formability in the uniaxial tension part of FLD is more than the equibiaxial part.

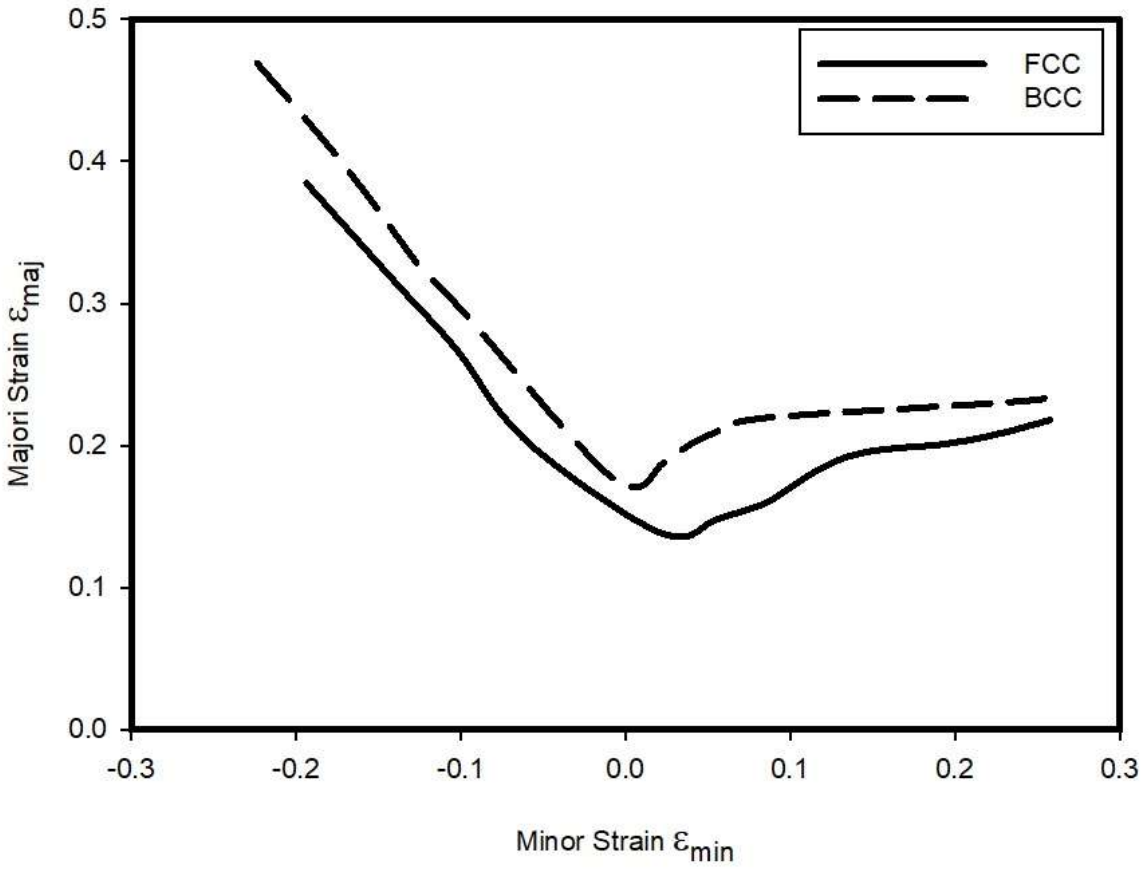

Figure 50. Forming limit diagram for FCC and BCC materials

3.3 FEM model for FLD determination using Nakajima test

Nakajima test is a standardized experimental procedure for the prediction of FLD for metal sheets. This test reproduces a process close to deep-drawing operations. Experimental determination of FLD requires specific facilities for high accuracy and is costly and time-consuming (Janbakhsh et al., 2012). Several studies have therefore been conducted on the use of appropriate numerical methods and finite element procedures to determine FLD by a purely numerical way (Habibi et al., 2017). In this part, the FLD curves for the aluminum alloy sheet Al6061 and St14 mild steel are obtained by simulating the Nakajima test with the M-K damage factor, f_0. This is a material damage data option in Abaqus which is introduced to stop the simulation when a critical strain state is reached.

3.3.1 FEM simulation for Nakajima test

3.3.1.1 Numerical and material parameters

In the Nakajima test, different strain paths can be obtained by stretching samples with different geometries using a spherical punch and circular molds (Habibi et al., 2017; Lumelskyj et al., 2017). The parts designed in Catia v5R21 include a deformable sheet and three rigid tools: a spherical punch, a die and a sheet holder. In the following simulation, the tools are rigid and the sheets are deformable. 66714 3D rigid (R3D3) elements are built for the rigid parts as shown in Figure 51.

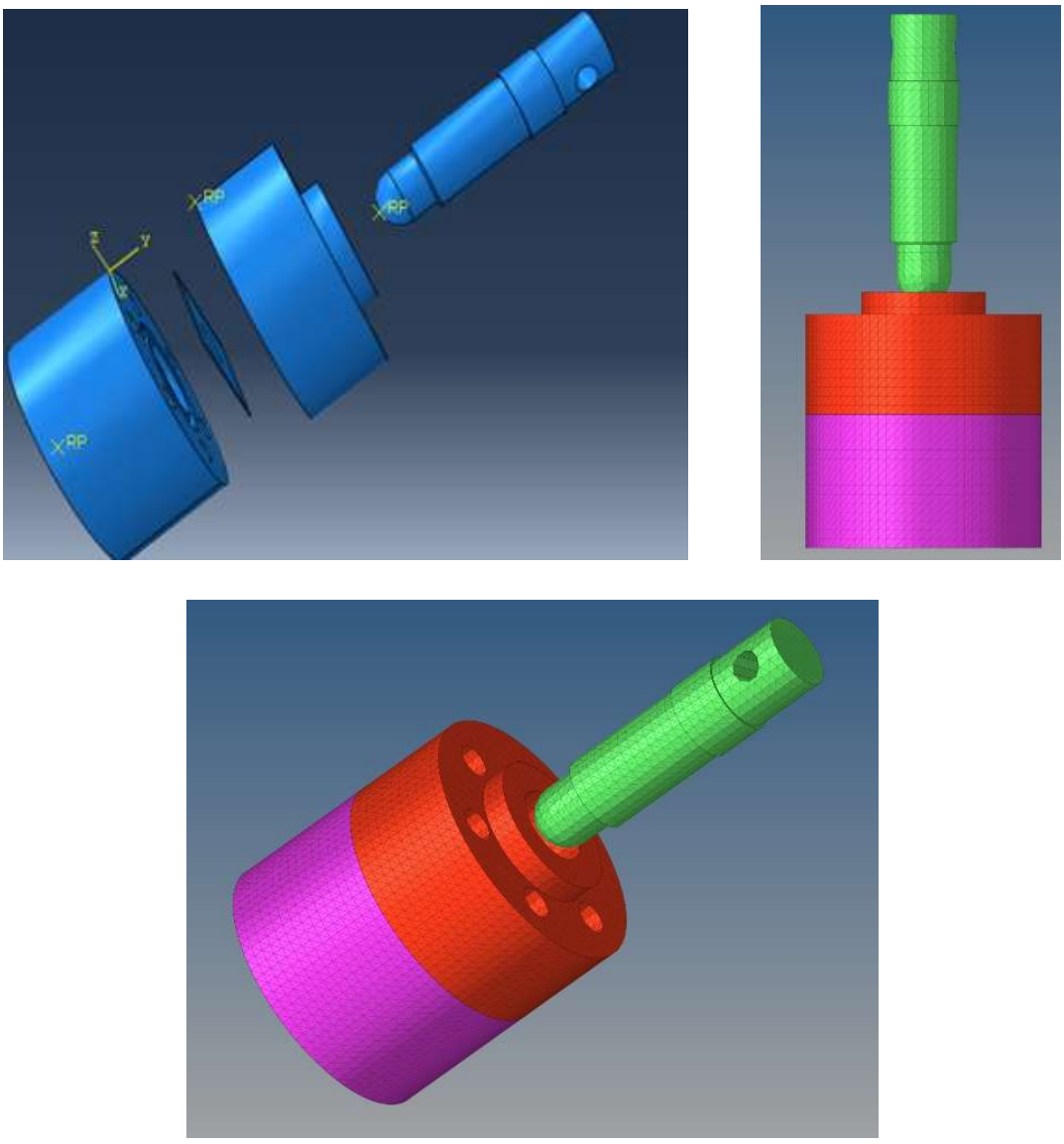

Figure 51. CAD and mesh of Nakajima test mounting

According to the international standard ISO 12004-2 (2008), at least five sheet samples are required to reproduce different strain paths. In our study, eight samples have been analyzed. The different sample sizes are shown in Figure 52.

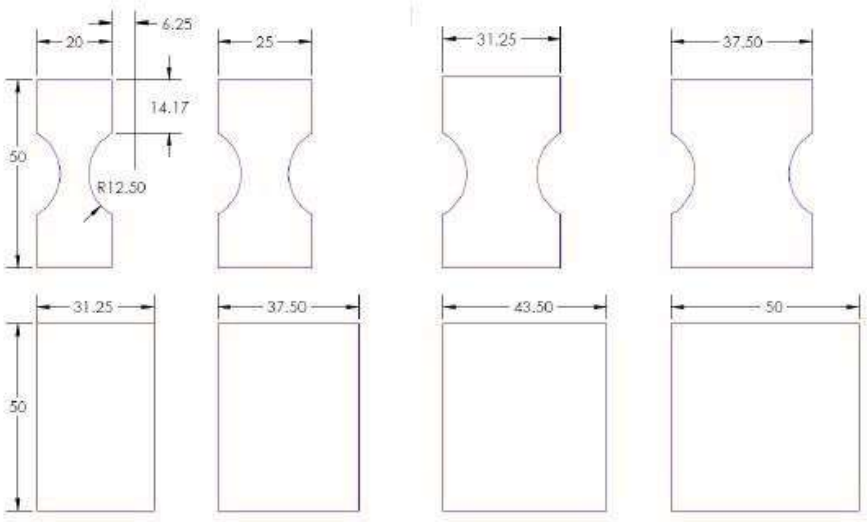

Figure 52. Nakajima sample sizes (Hashemi et al., 2014)

These eight samples with 0.7 mm thickness are meshed using C3D8R elements in Abaqus software. The Nakazima sample mesh is shown below.

The integration point of C3D8R elements is located in the middle of the element. Two different materials are analyzed: Al6061 and St-14 presented in part 3.2.2 and Table 3 and are studied respectively as FCC and BCC material. In addition, a material parameter is defined in Abaqus to play the role of stop criteria when necking appears. Among the different models available in Abaqus, "M-K" damage is once more chosen for its common use in Nakajima FEM simulation. This parameter may be used to evaluate the occurrence of necking phenomena and then to define the initiation of damage in the metal sheet. Visualization of the M-K damage factor helps to see the necking criticality in the metal sheet. Two user-defined parameters are introduced to calibrate the M-K model, the initial thickness ratio $f_0 = 0.991$ is considered to be an optimal thickness value and the initial orientation of the groove (Habibi et al., 2017).

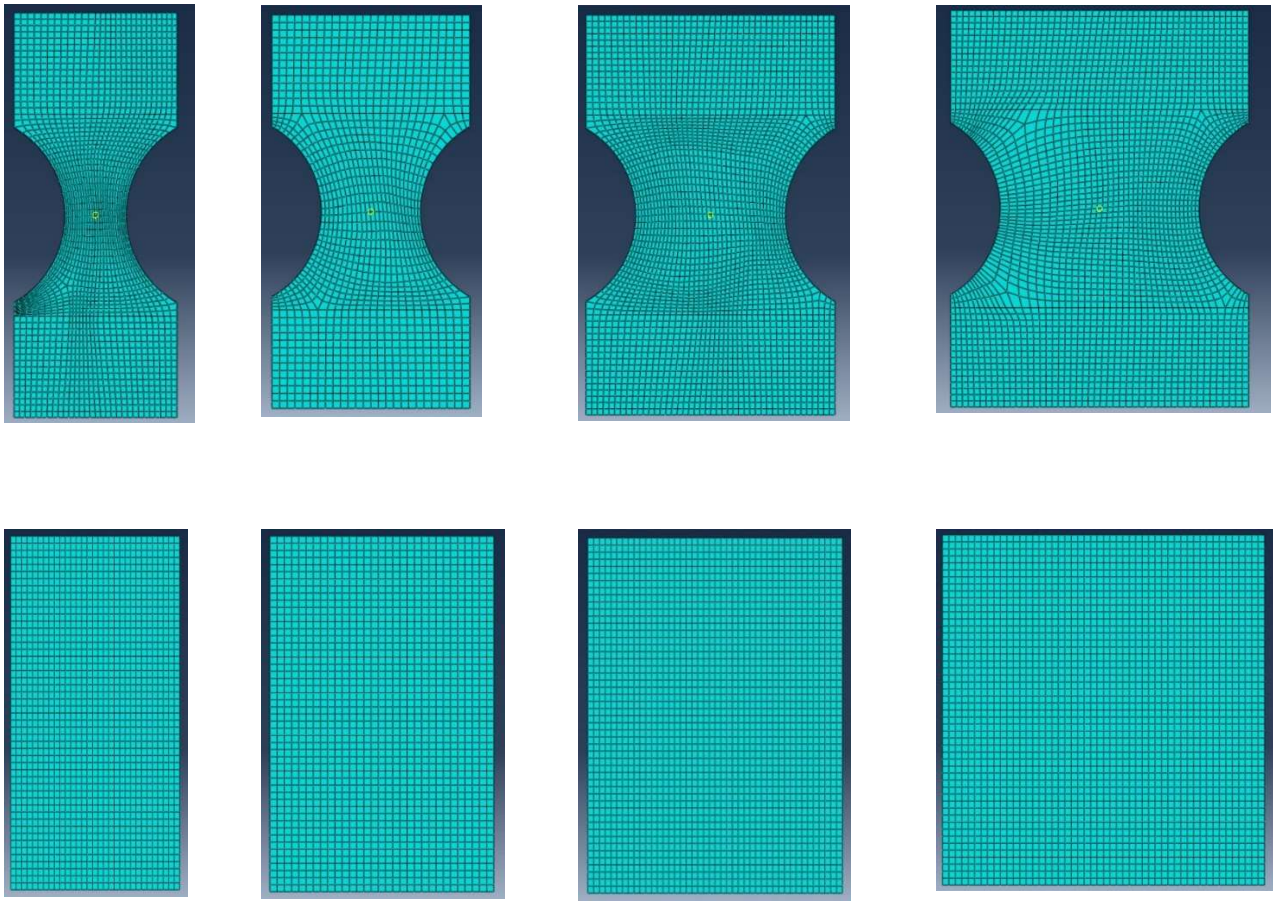

Figure 53. Nakajima sample mesh

The M-K damage parameters are given in the table below.

f_0	θ
0.991	0°

Table 4. Parameters of the M-K model groove

The die and the blank holder remain clamped. At all steps, the boundary conditions are applied in two parts of the edge of the sheet symmetrically. The sheet was pressed between the die and sheet holder and the sheet holder applied a 2 kN pre-force is on the sheet. Between the blank holder and the die applied in the reference point of the blank holder, while the punch translates following the Y-axis with a speed of 2 mm/s. The friction conditions between the sheet metal and the tool are described by Coulomb's model. The friction coefficient between punch and sheet is equal to 0.33. The friction coefficient for other parts is equal to 0.21 (Rahmatabadi and Hashemi, 2017).

Dynamic explicit analyses are carried out for both materials. The specimen deformations fields are shown in Figure 54.

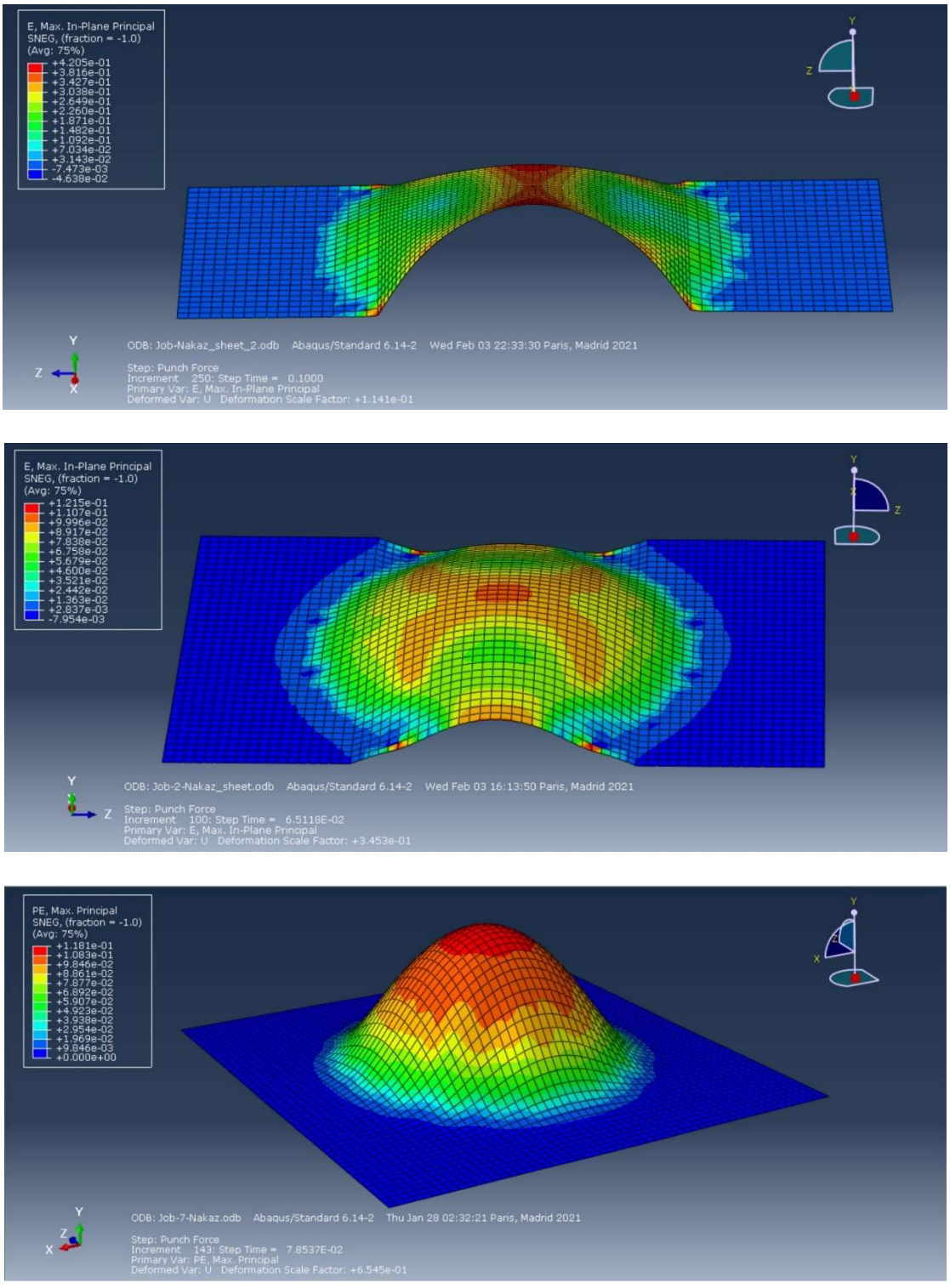

Figure 54. Strain distribution for Nakajima test - St-14 mild steel

3.3.2 FLD determination using Nakajima test for FCC and BCC materials

In this study, necking is considered to occur when the force reaches its maximum. When the maximum force in the punching direction is observed, the principal strains for the critical element located in the necking area are recorded (Moshksar and Mansoorzadeh, 2003). An illustration of the evolution of the force during the test for the second St-14 mild steel specimen is given in Figure 55.

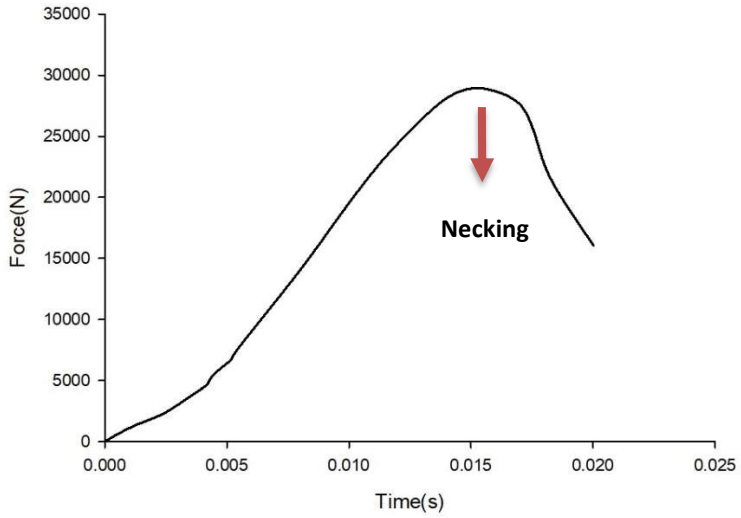

Figure 55. Punch force evolution during Nakajima test

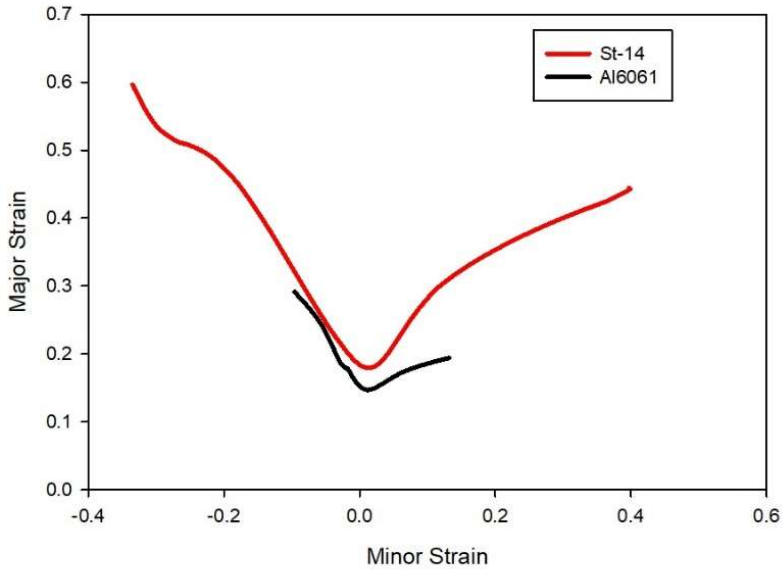

Figure 56. FLD for Al6061 and St-14 from Nakajima test

The minor and major strains are calculated for 8 different specimens. Each specimen represents one point on the FLD.

These FLD show that the formability of St-14 is higher than Al6061 for every loading path, in accordance with (Motamedi et al., 2017). The major strain at the FLD_0 point for St-14 is 25.42% higher than Al6061. In the next part, the results from FLD are used to analyze the formability of the sheet during the deep drawing process.

3.4 Application: deep drawing FEM simulations using FLD

In recent years, computer-aided manufacturing and design software have become essential tools for engineers. Its extensive use helps to reduce production costs and time and to preserve raw materials during forming processes (Park and Yarlagadda, 2008; Sheng et al., 2008).

In this part, the numerical simulation of deep drawing is investigated by using the Finite Element Method. Formability predictions obtained with Nakajima tests are used to predict the criticality of deep drawing process. Comparisons of current strain states and previously obtained FLD are therefore performed within Altair Hyperworks. The maximal punch forces may then be predicted.

3.4.1 FEM simulation for deep drawing processes

In this part, a deep drawing process with a cylindrical punch for Al6061 and St14 alloys is simulated. The deep drawing simulation model contains three different parts: die, sheet holder and punch. These parts are thicker than metal sheets, therefore they are assumed not deformable and modeled as rigid bodies in the following simulations (TalebSafa and Aghaei, 2018). For punch, die and sheet holder, 535, 1000 and 800 R3D4 linear quadrilateral elements are respectively built. The sheet metal is between the die and the sheet holder. The metal sheet specimen is circular sheet metal with a 150 mm diameter and 0.7 mm thickness. For sheet specimens, 10602 linear quadrilateral elements of type C3D8R are built. The mesh for the deep drawing FE model and the metal sheet is shown in Figure 57.

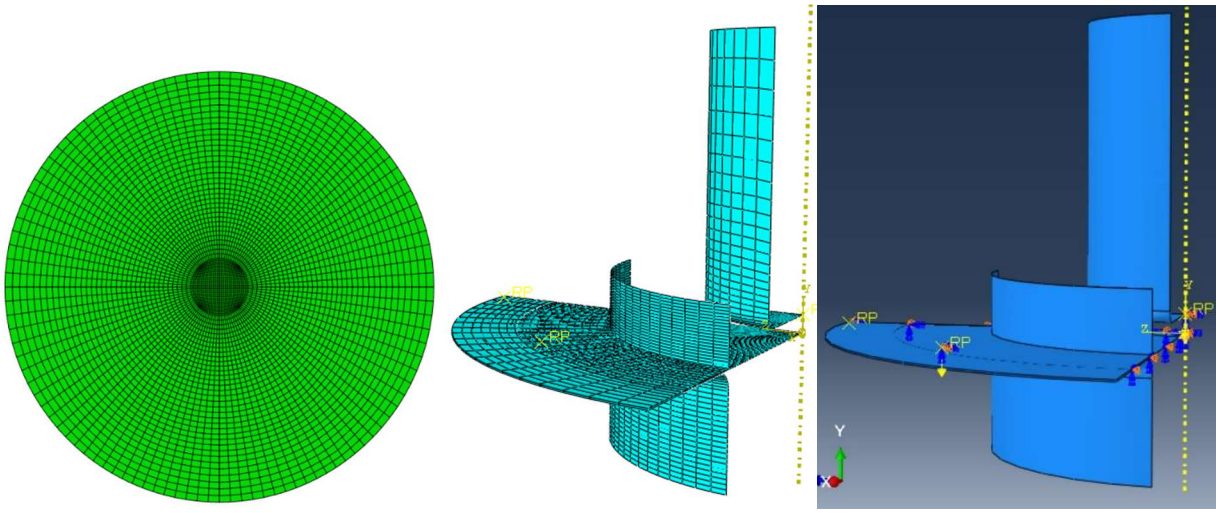

(a) **(b)** **(c)**

Figure 57. FE model for the deep drawing process

(a) cup mesh (b) deep drawing testing facilities mesh (c) applied boundary conditions

During this simulation, different types of boundary conditions are defined. The die is completely fixed during the simulation so the reference point is defined in a corner of the die. The Encastre boundary conditions are added at the reference point. The punch can move in the Y-axis. The initial punch speed is 0.7 m/s. The different boundary conditions for this simulation are shown in Figure 57c. An initial force is applied to the sheet holder. This initial force is equal to 20 kN. The sheet holder force is very important to control wrinkling during the deep drawing test. The interaction between different parts of the machine and specimen is defined as a surface-to-surface penalty contact type. The friction coefficient between the sheet metal and the die and between the punch and sheet metal is equal to 0.33 friction coefficient. The friction coefficient between the die and the sheet holder is equal to 0.15 (Colgan and Monaghan, 2003). Parallel computing is used for decreasing the simulation time. The simulation results and the effect of punch forces are represented in the next part.

3.4.2 Effect of punch force on the deep drawing process

The FEM simulation results are shown below. The effect of punch force is investigated on the lateral surface. These simulations are performed for Al6061 (FCC material) and St14 (BCC material) alloys. The simulation results for St14 with 10 kN punch is shown below.

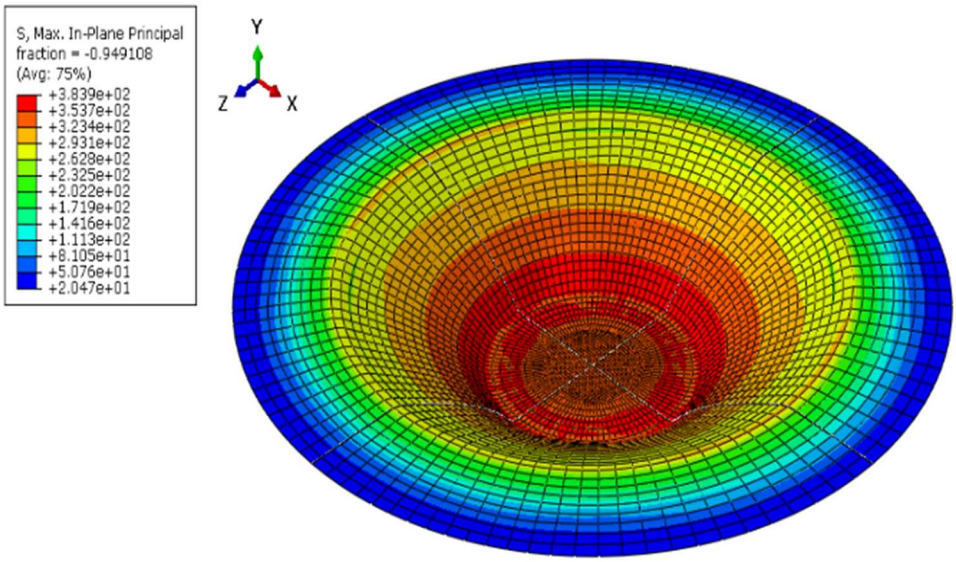

(a)

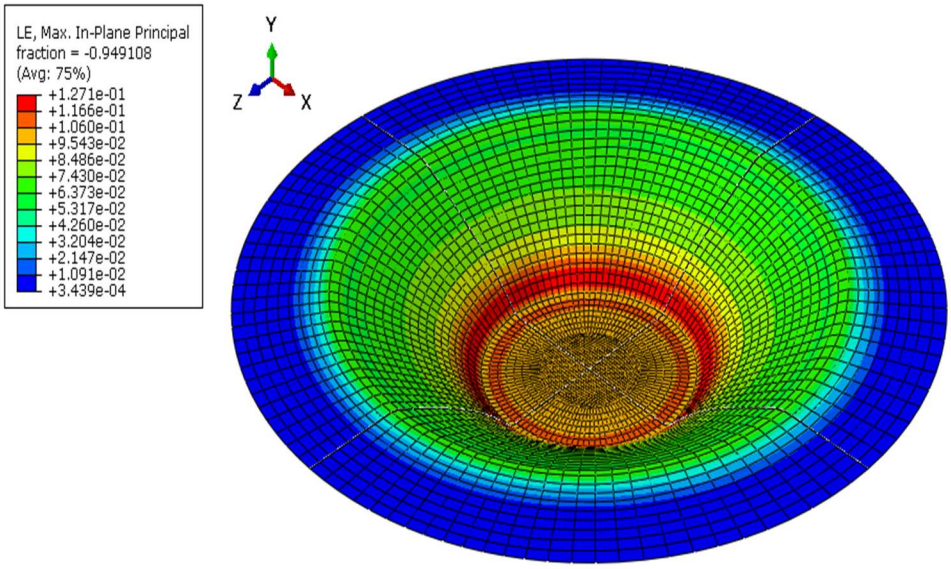

Figure 58. Maximum stress (a) and strain (b) in the St-14 deep drawing process for 10 kN punch force

The results in Figure 58 show that the maximum stress occurs on the flat zone (the specimen bottom) and the minimum stress occurs in the annular zone. The maximum strain occurs in the concave zone. By increasing the punch forces the maximum strain goes up to the lateral zone. The

evolution of punch force during the process is determined for Al6061 and St14 and is shown in Figure 59.

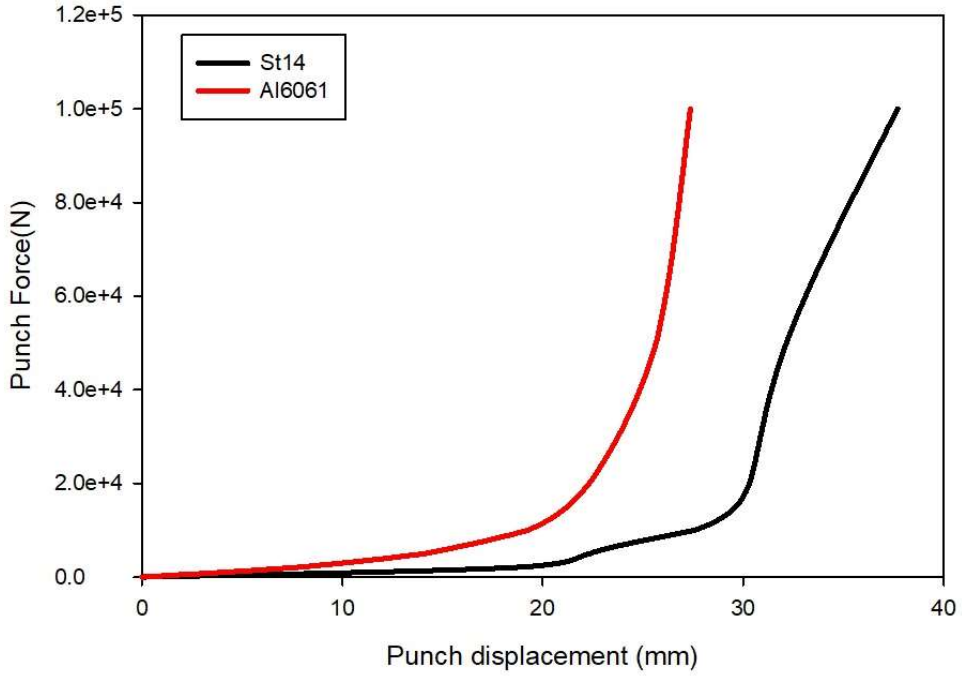

Figure 59. Punch force-displacement for Al6061 and St-14

The punch force changes from 0 to 100 kN and the results show that the maximum punch displacement is 37.78% bigger for St-14 than for Al6061. The curve slope shows the growth of the force for Al6061 is faster than St-14. The punch force limit during these simulations is 100 kN because if the sheet holder force does not change and the punch force passes 100 kN then the wrinkling will start in the convex zone.

3.4.3 Formability analysis for deep drawing process using FLD

In this part, the formability of sheet metal during the deep drawing process is analyzed with numerical Nakajima FLC obtained from part 3.3.2. The formability of metal sheets during the deep drawing process depends on different parameters such as punch speed, punch force, friction coefficient and sheet holder force (Oliveira et al., 2007). To study the effect of punch force on formability, this simulation is done for various punch forces to find a maximum applied punch force for both materials. The maximum applied punch force for forming metal sheet without wrinkling and necking is calculated.

- Simulation result for 60kN punch force for Aluminium-Al6061

The applied punch force for Aluminium-Al6061 is equal to 60 kN in this process. Figure 60 shows the analysis of the forming process for this applied punch force for Al6061. The failure occurs in the lateral zone. The minor and major strain in this zone passed the numerical Nakajima FLC.

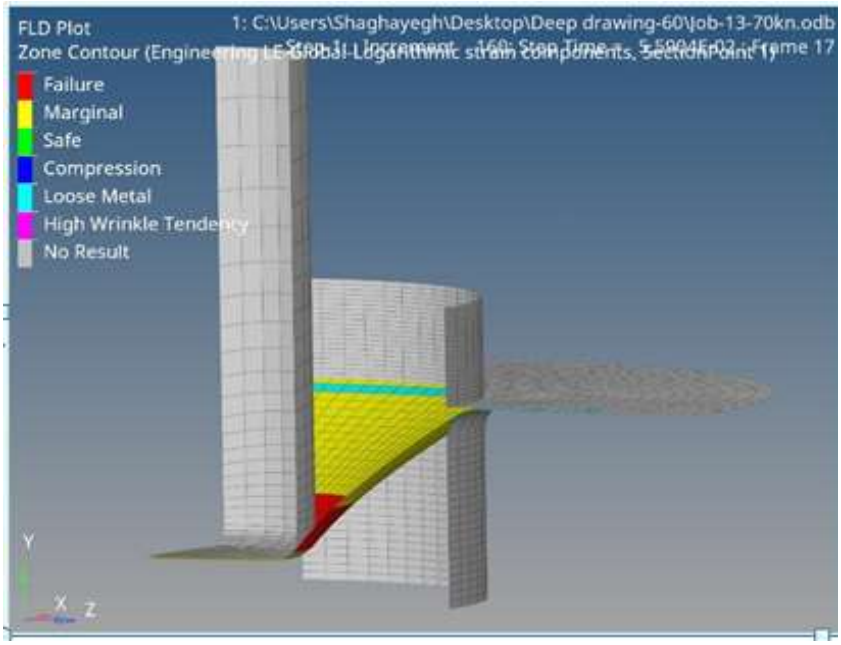

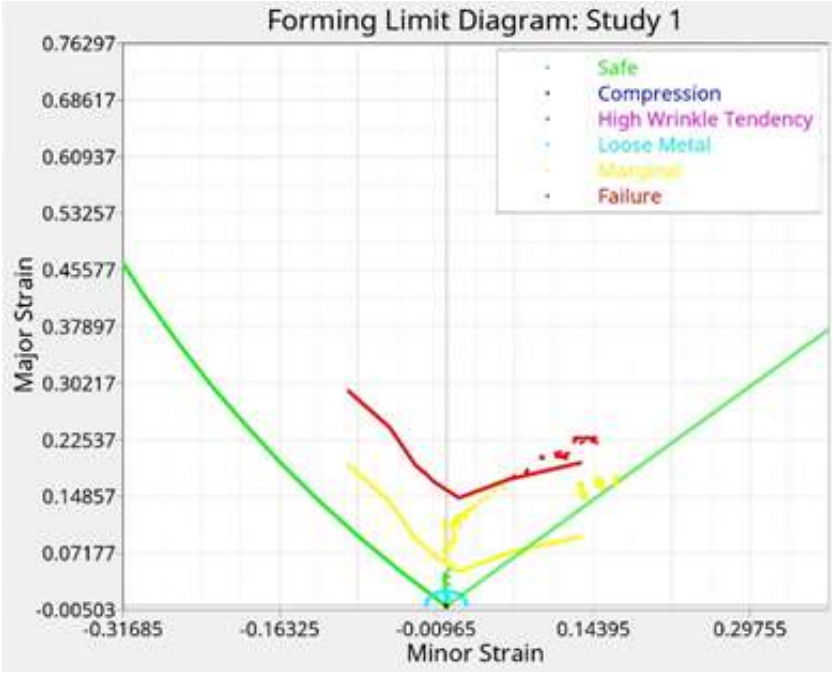

Figure 60. Effect of critical punch force on formability - Aluminum Al6061 specimen

- Simulation result for 80kN punch force for St-14 mild steel

The next study in this part is finding the maximum applied punch force for the St-14 mild steel specimen. The maximum applied punch force for the St-14 specimen is equal to 80 kN. Results are shown in Figure 61.

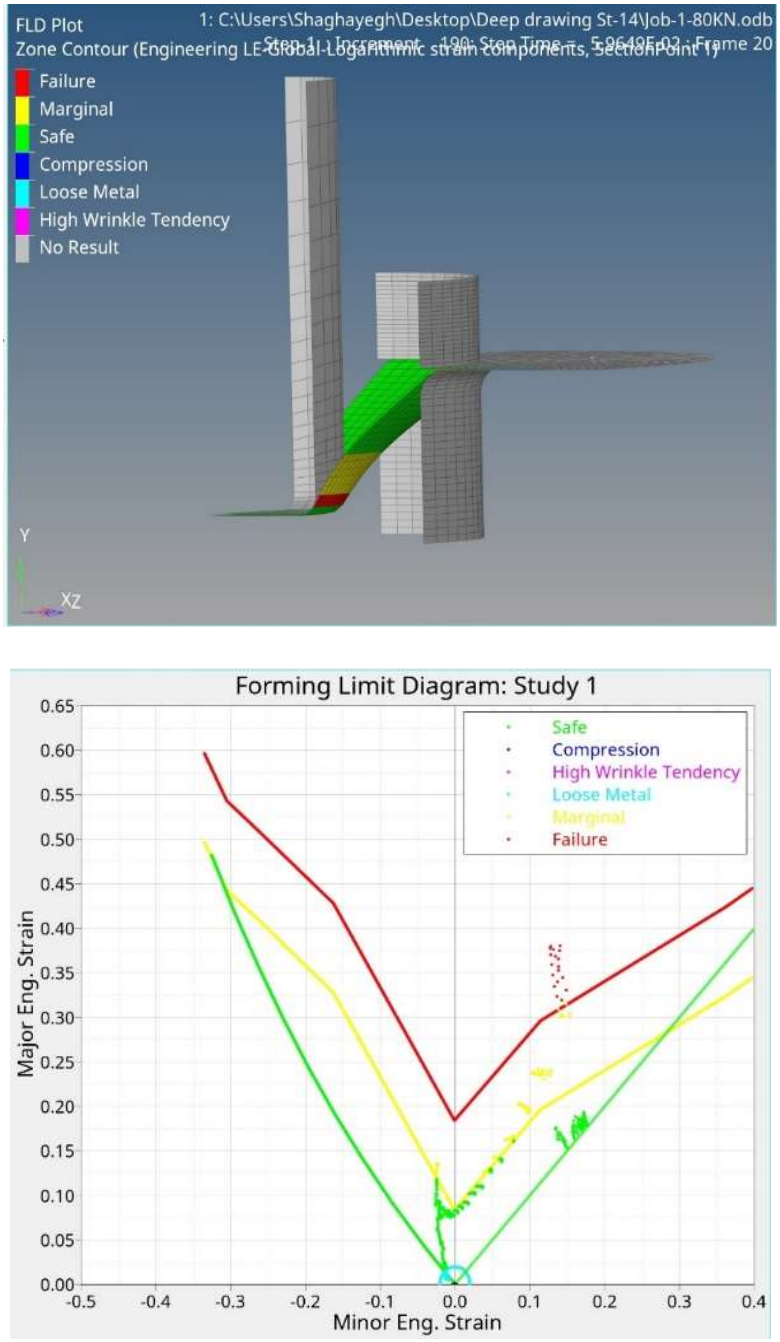

Figure 61. Effect of critical punch force on formability - St-14 mild steel specimen

3.5 Conclusion

This chapter deals with the numerical investigation of strain localization by using the Marciniak-Kuczynski model. The results show that the formability of sheet metal is increased by increasing the value of the initial thickness ratio, f_0. The formability of sheet metals is changed by changing the orientation bands θ. In this study, the orientation band changes from 0° to 40°. By increasing the value of θ the formability of sheet metal is decreased.

Forming limit diagrams for the FCC and BCC materials slip system are then computed using the Marciniak-Kuczynski model. The main aim of this part is to point out the differences of FLD for FCC and BCC materials. From the obtained results, it is shown that the lower forming limit curve forecast for FCC materials and that the difference in the biaxial part of FLD is more than the uniaxial part.

A second method to obtain FLD is then implemented in this thesis is the deep drawing test. During this process, and for the studied materials, the maximum punch forces for BCC structures are bigger than the FCC structure and the punch displacements for BCCs materials are bigger than FCCs materials, so the formability and ductility for BCCs is higher than FCCs. For the determination of the formability of the sheet metals, the Nakajima test is used so the numerical tests are done for BCC and FCC material and the FLD for both materials are drawn. The strain for the Nakajima test is an out-plane strain and in this case, also, the formability of BCC materials is higher than FCC materials.

References

Altmeyer, G., Abed-Meraim, F., and Balan, T. (2010). Investigation of some localization criteria and their relevance to prediction of forming limit diagrams, Steel Research International, 81, 1364–1367.

Colgan, M., Monaghan, J. (2003). Deep drawing process: Analysis and experiment, Journal of Materials Processing Technology, 132(1–3), 35–41. https://doi.org/10.1016/S0924-0136(02)00253-4

Evangelista, S. H., Lirani, J., Al-Qureshi, H. A. (2002). Implementing a modified Marciniak-Kuczynski model using the finite element method for the simulation of sheet metal deep drawing, Journal of Materials Processing Technology, 130–131, 135–144. https://doi.org/10.1016/S0924-0136(02)00729-X

Habibi, M., Ghazanfari, A., Assempour, A., Naghdabadi, R., Hashemi, R. (2017). Determination of Forming Limit Diagram Using Two Modified Finite Element Models, Asjr-Me, 48(4), 141–143.

Hashemi, R., Mamusi, H., and Masoumi, A. (2014). A simulation-based approach to the determination of forming limit diagrams. Proceedings of the Institution of Mechanical Engineers, Part B: Journal of Engineering Manufacture, 228(12), 1582–1591. https://doi.org/10.1177/0954405414522448

Inal, K., Neale, K. W., Aboutajeddine, A. (2005). Forming limit comparisons for FCC and BCC sheets, International Journal of Plasticity, 21, 1255–1266. https://doi.org/10.1016/j.ijplas.2004.08.001

Janbakhsh, M., Djavanroodi, F., Riahi, M. (2012). A comparative study on determination of forming limit diagrams for industrial aluminium sheet alloys considering combined effect of strain path anisotropy and yield locus, Journal of Strain Analysis for Engineering Design, 47(6), 350–361. https://doi.org/10.1177/0309324712448302

Lumelskyj, D., Rojek, J., Banabic, D., and Lazarescu, L. (2017). Detection of Strain Localization in Nakazima Formability Test - Experimental Research and Numerical Simulation, Procedia Engineering, 183, 89–94. https://doi.org/10.1016/j.proeng.2017.04.016

Marciniak, Z., Kuczyński, K. (1967). Limit strains in the processes of stretch-forming sheet metal, International Journal of Mechanical Sciences, 9(9), 609–620. https://doi.org/10.1016/0020-7403(67)90066-5

Moshksar, M. M., Mansoorzadeh, S. (2003). Determination of the forming limit diagram for Al 3105 sheet, Journal of Materials Processing Technology, 141, 138–142. https://doi.org/10.1016/S0924-0136(03)00262-0

Motamedi, M.A, Hadian, B., Hashemi, R. (2017). Forming limit diagram for Al 6061 at different temperatures from nakazima test, 16th Iranian Airospace Conferance, 1–9.

Müschenborn, W., Sonne, H.M. (1975). Einfluß des Formänderungsweges auf die Grenzformänderungen des Feinblechs, Archiv Für Das Eisenhüttenwesen, 46(9), 597–602. https://doi.org/10.1002/srin.197503686

Oliveira, R.P., Alves, M., Menezes, J.L. (2007). Influence of process parameters on the deep drawing of stainless steel, Finite Elements in Analysis and Design, 43, 1062–1067. https://doi.org/10.1016/j.finel.2007.06.011

Rahmatabadi, D., Hashemi, R. (2017). Experimental evaluation of forming limit diagram and mechanical properties of nano/ultra-fine grained aluminum strips fabricated by accumulative roll bonding, International Journal of Materials Research, 108(12), 1036–1044. https://doi.org/10.3139/146.111566

Rahmatabadi, D., Tayyebi, M., Sheikhi, A., Hashemi, R. (2018). Fracture toughness investigation of Al1050/Cu/MgAZ31ZB multi-layered composite produced by accumulative roll bonding process, Materials Science and Engineering A, 734(August), 427–436. https://doi.org/10.1016/j.msea.2018.08.017

Ramesh, C. S., Pramod, S., Keshavamurthy, R. (2011). A study on microstructure and mechanical properties of Al 6061–TiB2 in-situ composites, Materials Science and Engineering: A, 528(12), 4125–4132. https://doi.org/https://doi.org/10.1016/j.msea.2011.02.024

St-14 Robert Company datasheet, (2008)., 1–2.

TalebSafa, V., Aghaei, M. (2018). Predicting the forming limit diagram by using numerical simulation of Nakazima and M-K tests, Amirkabir Journal of Mechanical Engineering.

Toroghinejad, M. R., Dini, G. (2006). Effect of Ti-microalloy Addition on the Formability and Mechanical Properties of a Low Carbon (ST14) Steel, International Journal of ISSI.

Chapter 4

CPFEM simulation of biaxial traction test with MK-approach

4.1 Introduction

In modern industries, the knowledge of the evolution of the material microstructure during forming processes is important. The macroscopic and microscopic deformation of polycrystalline metals can be simulated by Crystal Plasticity Finite Element Method (CPFEM) (Lorentzen, 1997). The CPFEM is based on crystal plasticity theory coupled with the finite element method. The CPFEM is based on grain deformations (Wang et al., 2014). This method is a good computational way to predict the micromechanical behavior of materials. The single crystal orientation and texture evolution can be predicted by this method (Wanet al. 2016). The stress and strain during the simulation are calculated for each grain. The lattice rotation is calculated by respecting the hardening law.

The background of CPFEM comes back to the 1950s. In 1993, Fleck and Hutchinson (Fleck, Hutchinson, 1993) worked on new plasticity theory for microscale to predict the grains orientations during the forming process. The strain gradient plasticity model presented by Nix (Nix, Gao, 1998) is suitable for CPFEM codes. A three-dimensional CPFEM model is presented by Si (Si et al., 2008). This method is used in Abaqus/standard software by writing a User-defined mechanical material behavior subroutine called UMAT subroutine.

In this chapter 4, the CPFEM for the M-K biaxial traction test is developed. The CPFEM has been implemented in the commercial code Abaqus software using an UMAT subroutine.

The plastic deformation of polycrystalline at microscale level is described by this method (Beaudoin et al., 1994). The initial grains crystallographic orientation or texture is obtained with the XRD experimental measurement. These measured orientations will be used in the simulations as input data. The evolution of the grain's orientation is investigated during the biaxial traction test for BCC and FCC crystallographic structures. In this study, two polycrystalline materials are used: St-14 mild steel and Al6061 commercial aluminum. The commercial St-14 mild steel has a BCC crystallographic structure while Al6061 commercial aluminum alloy has a FCC crystallographic structure.

In the last part of this chapter 4, the calculation time of simulations is studied since FEM run time is very important.

4.2 Crystal Plasticity Finite Element Model

4.2.1 UMAT subroutine

The UMAT subroutine is an additional Fortran program in ABAQUS CAE to define mechanical constitutive law. This subroutine supplies the jacobian matrix of materials for mechanical constitutive law and the stress and strain values are updated after each increment (Simulia, 2014).

The following UMAT subroutine is based on the Taylor model (Taylor, 1938) presented in Chapter 2. The Taylor model is the simplest model for polycrystalline homogenization. The main feature of this model is that the gradient deformation for each grain is equal to the macroscopic deformation gradient of the polycrystalline. The macroscopic Cauchy stress for the polycrystal equals to the average of Cauchy stress for all of the grains (Staroselsky and Anand, 2003) :

$$\overline{T} = \frac{1}{N}\sum_{J=1}^{N} T^{J} \qquad (4.1)$$

In this equation, T^{J} is the Cauchy stress for grain number J and N is the number of grains.

The simulated model includes 514535 C3D8R elements for the biaxial test including the Marciniak-Kuczynski model. The mesh is shown in Figure 62. The CPFEM model size is 0.6×0.6×0.3 mm for the perfect zone and 0.6×0.6×0.297 mm in defect zone (Mashayekhi and Sherbaf, 2012).

Based on previous presented simulations in chapter 3, CPFEM calculations are performed in a second step. In chapter 3, the boundary conditions, as well as details for the FEM simulation, are given.

The CPFEM simulation runs in Abaqus standard static mode with 0.001 fixed time step and 18147-time step increments.

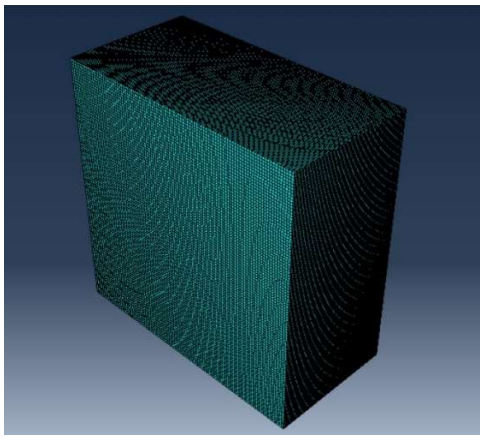

Figure 62. Mesh for CPFEM simulation

CPFEM code is a user material subroutine in Abaqus. This subroutine takes into account deformation at grain scale as well as the lattice rotation. In CPFEM simulation, the stress and strain for a single crystal are calculated by Abaqus CAE for each increment.

The stress and strain are updated during each increment and at the end of each increment the jacobian matrix $\frac{\partial \Delta\sigma}{\partial \Delta\varepsilon}$ is calculated. This matrix depends on gradient time integration. For linearizing the stress and strain at the end of each increment, the Newton-Raphson method is used. The jacobian matrix is calculated by using the Newton-Raphson method.

In a CPFEM simulation, the initial texture is taken into account. In this study, the initial textures for FCC and BCC materials come from the XRD experimental measurement done at the University of Tehran (see Chapter 5). 500 initial Eulerian orientations have been considered. We note that this initial texture is close to a random one (see Figure 63).

The simulations also include the hardening mode. The hardening law and deformation modes are defined in the UMAT subroutine. Deformation modes come from literature for FCC and BCC materials (Nagra et al., 2018). There are 7 subroutines in Umat to calculate lattice hardening law. Both the classical power law and Kalidindi hardening law are taken into account in the UMAT. In chapter 2, one may find equations describing these hardening laws. Then, the rotation is calculated in one subprogram. This subroutine investigates the initial orientation of the cubic crystal. The next part of this subroutine is devoted to the calculation of slip direction and slip planes. The slip rates are calculated in one separate subroutine for all of the slip systems. All of these subroutines are repeated iteratively for all of the increments. The hardening matrix is built in a separate

subroutine after this step. The self-hardening matrix is a diagonal matrix and latent hardening is an off-diagonal matrix.

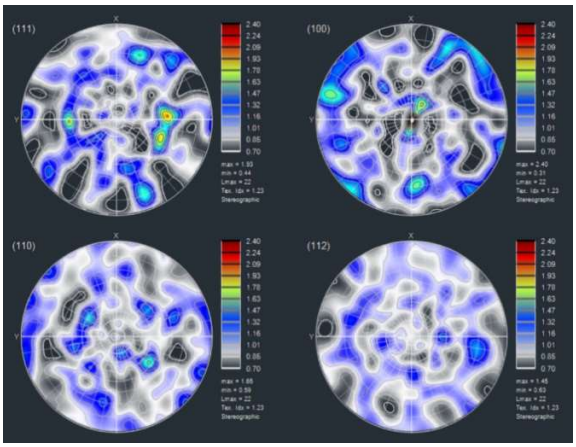

(a)

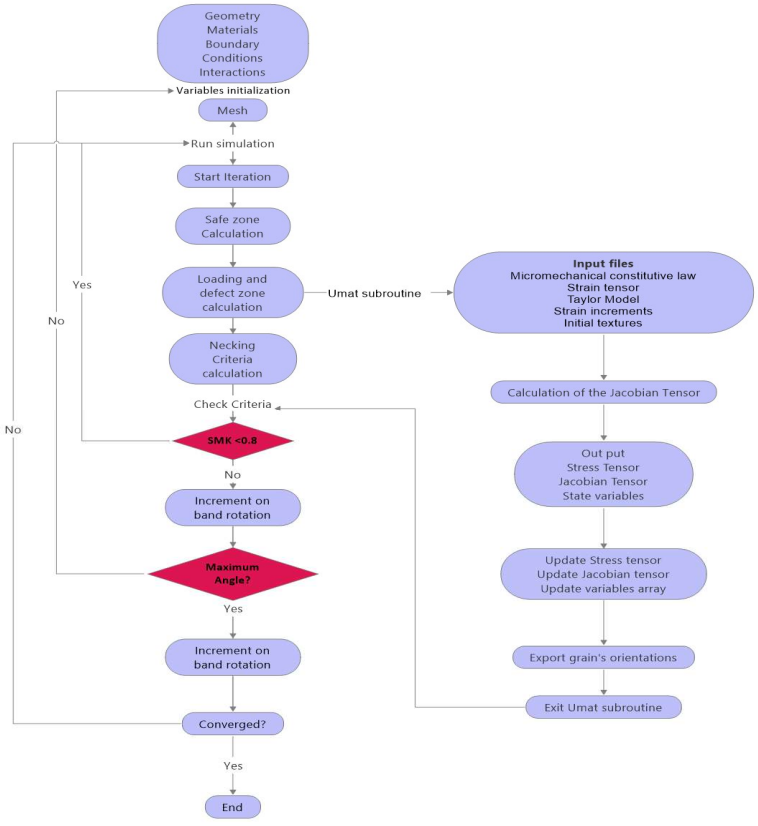

(b)

Figure 63. (a)Initial orientation for St-14 mild steel XRD measurement from the University of Tehran (b) CPFEM simulation algorithm

4.3 CPFEM simulation of biaxial traction test with MK-approach

In this part 4.3, the biaxial traction test coupled with M-K criterion is analyzed with a CPFEM simulation. Two types of material structures: BCC and FCC are considered for the simulations. The {111} <110> slip system is taken for FCC material and the {110} <111> slip system is taken for BCC material. In this study, the X-direction represents the rolling direction (RD), the Y-direction represents the transverse direction (TD) and the Z-direction represents the normal direction (ND).

4.3.1 Analyses of texture evolution for BCC materials under biaxial traction test

For this study, 3 different values of the loading ratio α are chosen. $\alpha = 0.1$ is chosen as the first point of the biaxial traction test. $\alpha = 0.5$ is chosen as FLD_0 point and $\alpha = 0.9$ is penultimate point.

Figures 64-65-66 show the simulated poles figures (111), (100), (110) and (122) for zones A and B for different values of α. These simulated textures show that the grain's orientations are sensible to the value of α in both zones. It is a foreseeable result since the different values of α lead to different loading or strain path conditions. The pole figures (111) for different values of α in zone A show that the grain orientation changing density is decreased by increasing α value.

- Textures for α=0.1

Figure 64 shows the pole figures for α=0.1 for zones A and B.

The intensity of texture is more important in zone A than in zone B. In zone B, the crystallographic textures are quite heterogeneous because this zone, it's a perturbation zone. In zone B, the distribution of stress and strain is less regular than in zone A. On the other hand, in zone A, we note a relative symmetry in the distribution of the crystallographic texture orientations.

- Textures for α=0.5

The pole figures for $\alpha = 0.5$ are shown in Figure 65 for zone A and zone B.

Here again, only the texture in zone A are symmetric. However, the intensity is nearly the same in both zones A and B but slightly greater in zone B.

- Textures for α=0.9

Figure 66 shows the pole figures for α=0.9 for both zones. The grain's orientations change in zone A and B symmetrically. This is explained by the fact that the loading is close to a biaxial test since α=0.9. The intensity of the texture is quite equal in zone A and zone B but still stronger in zone B. In conclusion, we note that the applied loading strongly affects the final crystallographic texture in both zones.

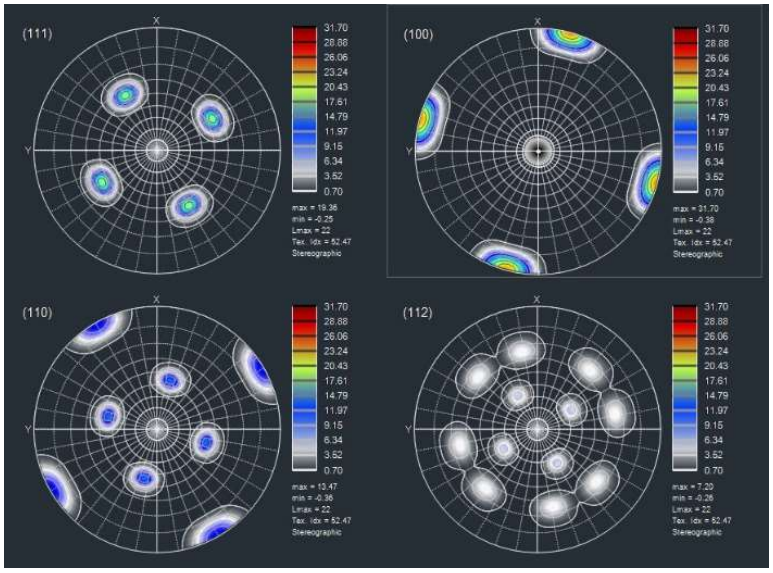

(a) Zone A

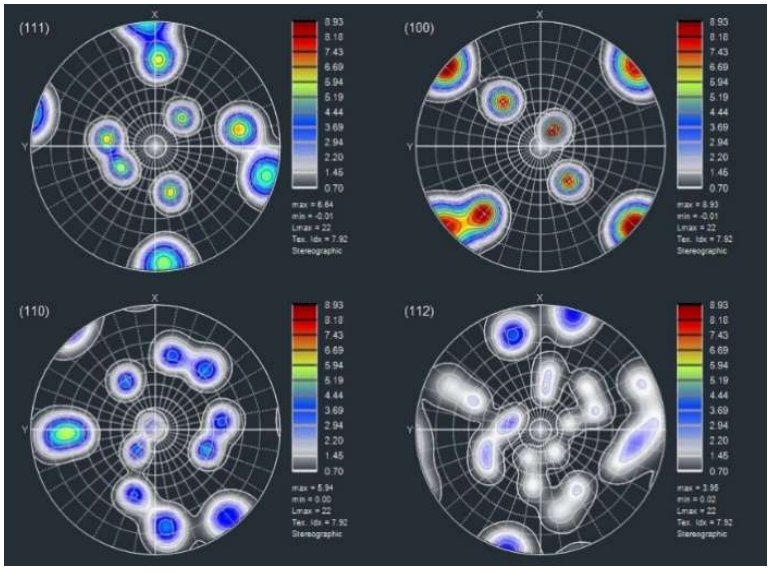

(b) Zone B

Figure 64. Pole figures for biaxial traction test with M-K approach, α=0.1
(a) Zone A, (b) Zone B

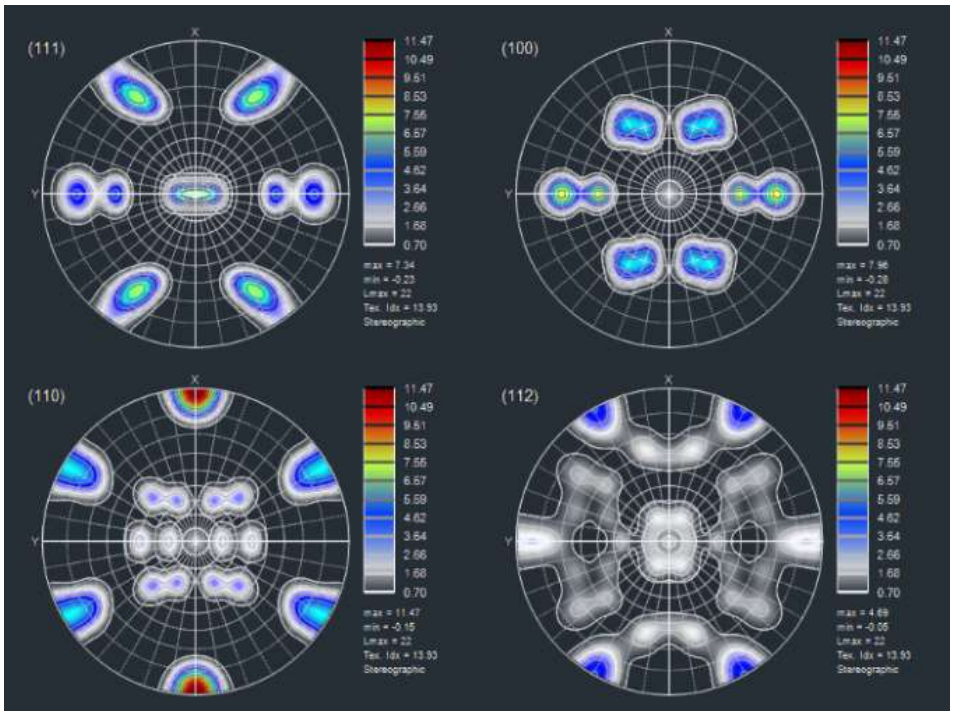

(a) Zone A

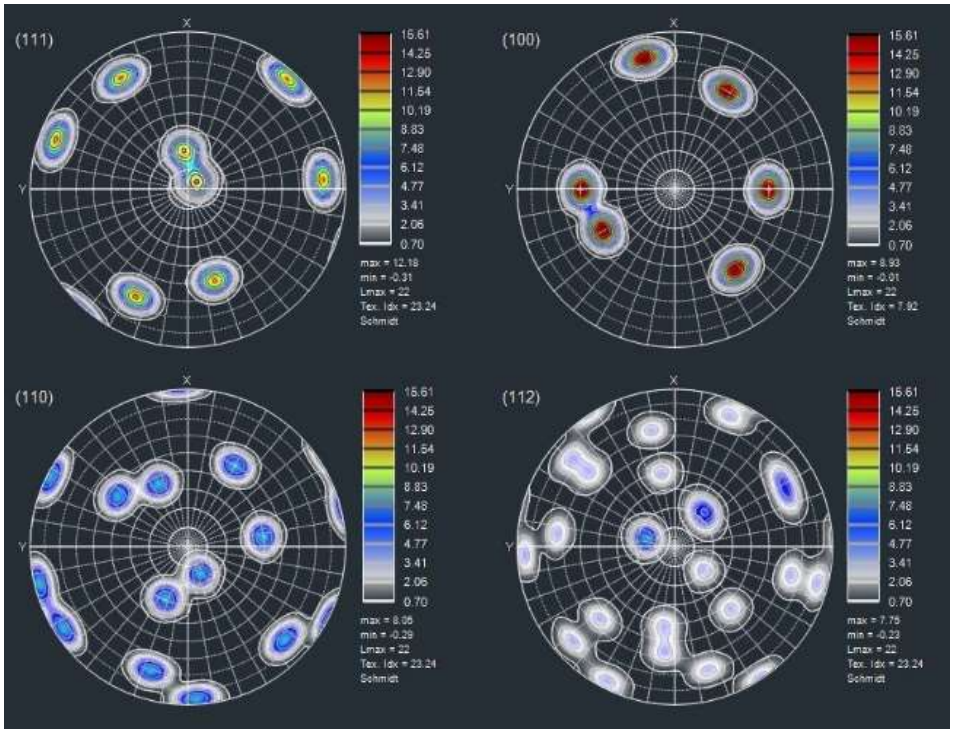

(b) Zone B

Figure 65. Pole figure for biaxial traction test with M-K approach, α=0.5 (a) Zone A, (b) Zone B

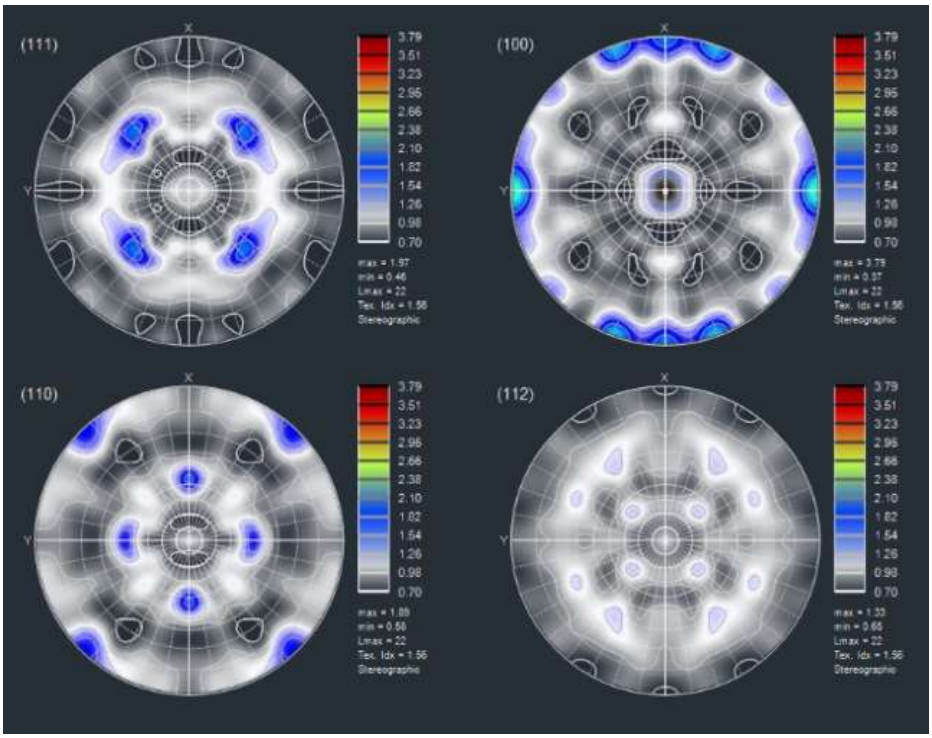

(a) Zone A

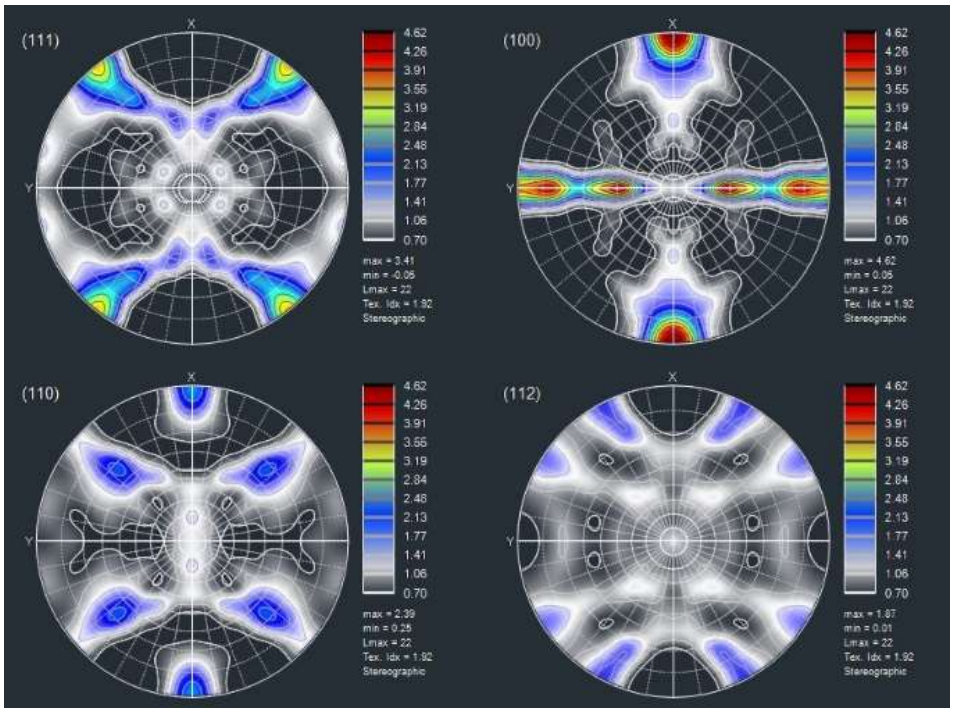

(b) Zone B

Figure 66. Pole figure for biaxial traction test with M-K approach α=0.9 (a) Zone A, (b) Zone B

4.3.2 Analyses of texture evolution for FCC materials under biaxial traction test

In this part, the effect of the loading ratio α on the microstructure of FCC materials is investigated. For simulation, an alloy of aluminum, Al6061, is taken as studied FCC material. Results of simulation are given in figures 67-68-69.

3 values are chosen for α: 0.1, 0.5, 0.9 like the previous part.

- Textures for α=0.1

Figure 67 shows the pole figures for α = 0.1 for both zones A and B. The pole figures show that the grain orientation changes are symmetric in zone A and in zone B. This was not the case for BCC structures where only symmetry appears in zone A. For zone A, the (111) pole figure shows that the maximum density is located near to the center. The intensity is greater in zone A than in zone B. However, we note that these intensities for FCC structures are lower than for BCC structures (see figure 67). The textures in zone B are more diffuse than in zone A mainly due to the fact that zone B is a perturbation zone one.

- Textures for α=0.5

Here again, a symmetry for both zones are recovered (see figure 68). A difference between the intensities of these two zones are important, the intensity is largely higher in zone A than in zone B. The distribution of texture is more diffuse in zone B than in zone A.

- Textures for α=0.9

The symmetry in both zones A and B is recovered again for this loading ratio (see figure 69). For α=0.9, the intensity of texture is equivalent in both zones but slightly greater in zone B. This is due to the fact that the loading is close to a biaxial test.

Our results are consistent with literature such as the work of Signorelli (Signorelli et al., 2019) who shows that the textures are very sensible to the perturbation zone existing in a M-K model.

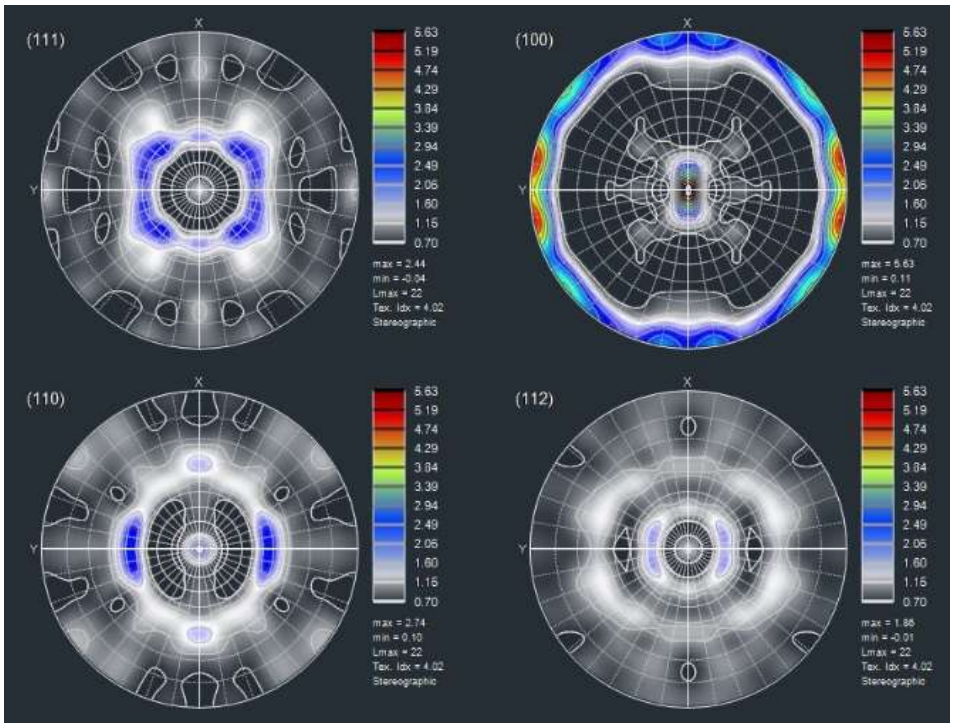

(a) Zone A

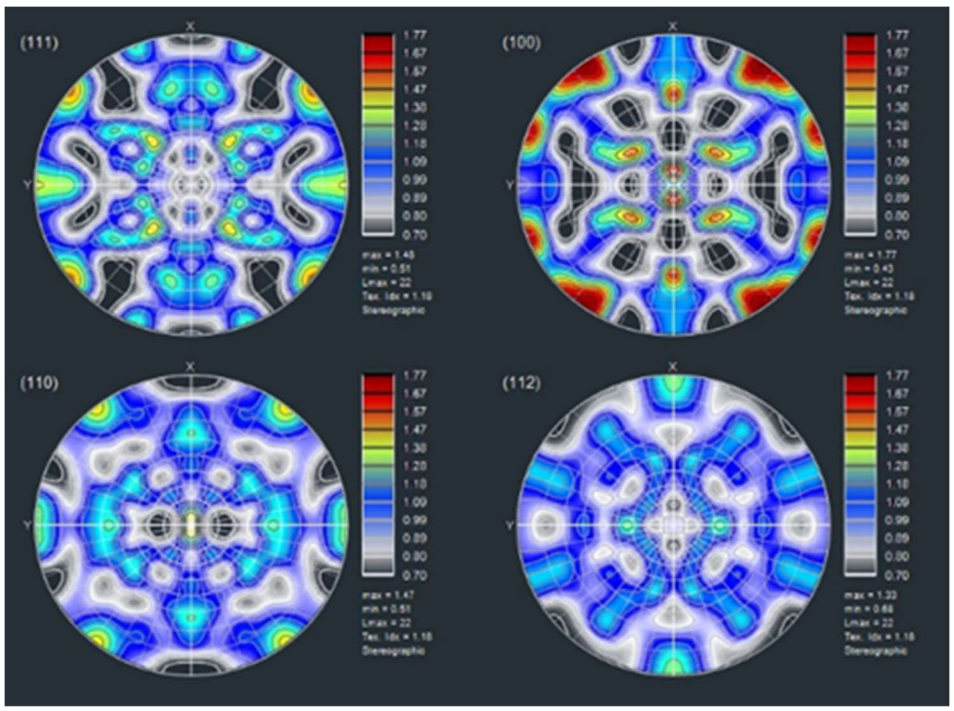

(b) Zone B

Figure 67. Pole figure for biaxial traction test with M-K approach α=0.1
(a) Zone A, (b) Zone B

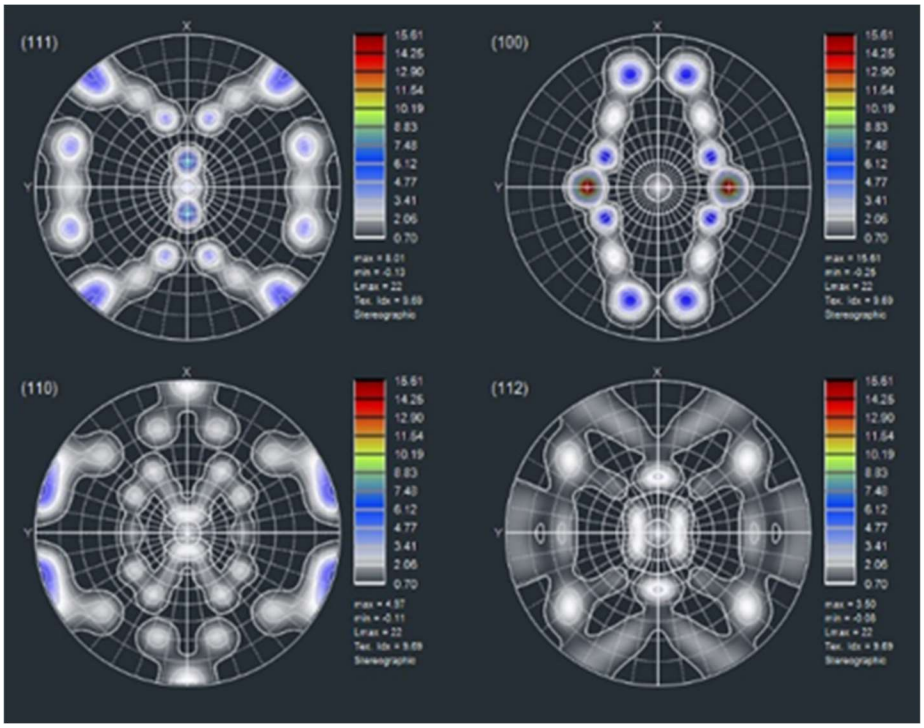

(a) Zone A

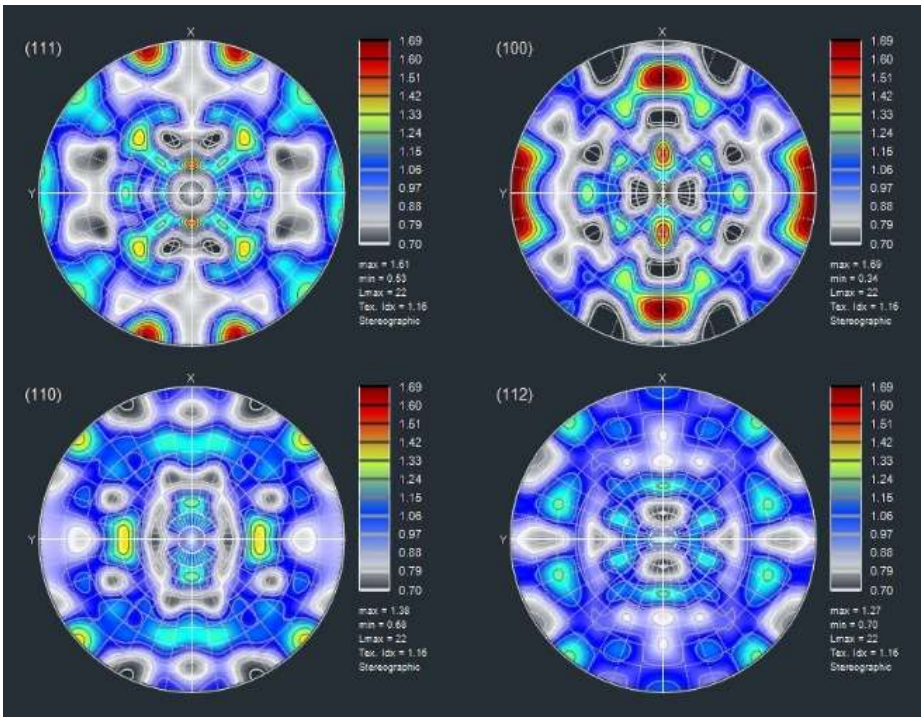

(b) Zone B

Figure 68. Pole figure for Biaxial traction test with M-K approach, α=0.5
(a) Zone A, (b) Zone B

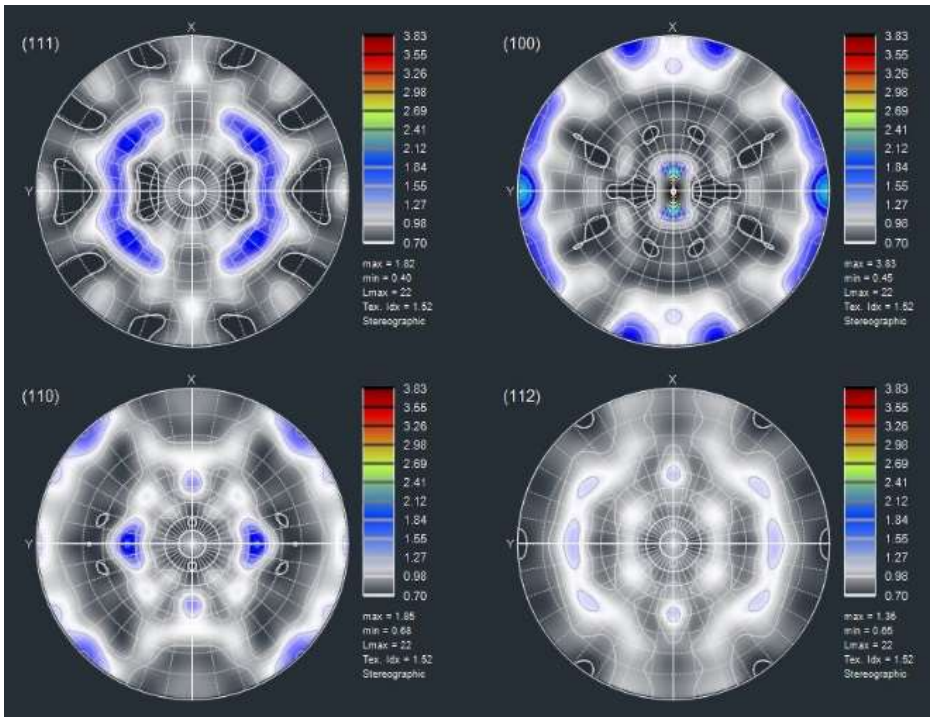

(a) Zone A

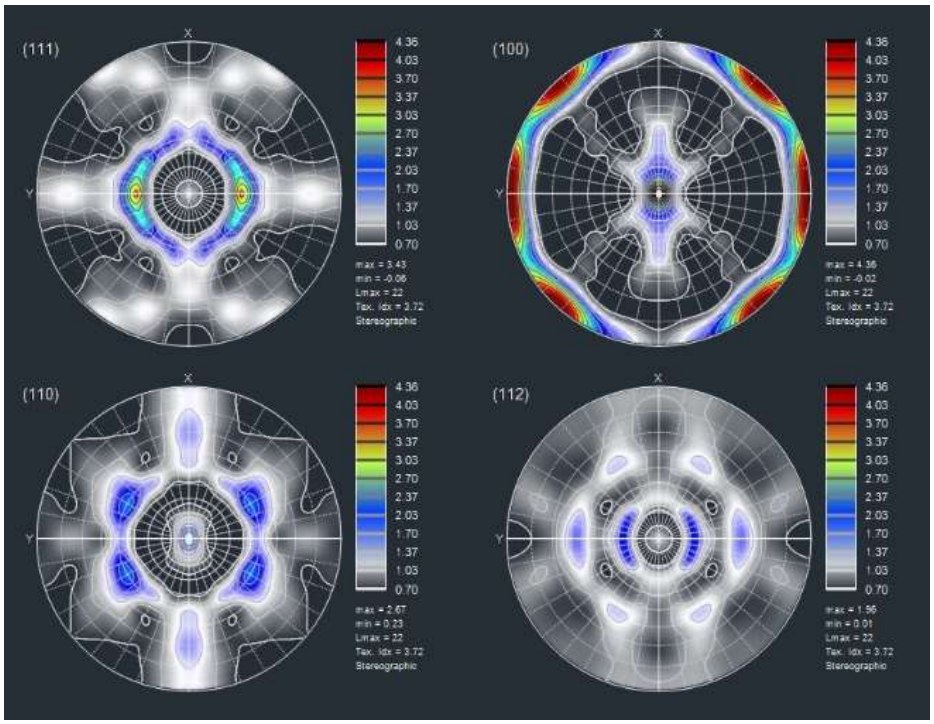

(b) Zone B

Figure 69. Pole figure for Biaxial traction test with M-K approach, α=0.9 (a) Zone A, (b) Zone B

4.3.3 Effect of texture evolution on the FLDs

In this study, the FLD are drawn by changing the loading ratio value α. During this biaxial traction test, the grains are rotated in different orientations. In this M-K model, the necking occurs in zone B at a certain level of critical strain.

The FLD for St-14 and Al6061 with texture and without texture evolution are shown in Figure 70. The results show that the texture evolution has little effect on FLC. The curve without texture is quite close in the left side of FLC but at FLD_0 point the texture evolution curve is lower than the curve without texture and by moving to the right side the FLCs are the same. In the FLD_0 point, the major strain without texture evolution curve is 7.19% higher than FLC with texture but on the left side, this difference decreases to 1.57% and on the right side is equal to 0.52%. In Figure 70(c), Inal (Inal et al., 2005) analysed the influence of textures evolution on FLD for BCC material with the same M-K method. Little differences are observed at FLD_0 point but by moving to the right side of FLC the strains are quite same for both simulations. Our results are thus consistent with literature.

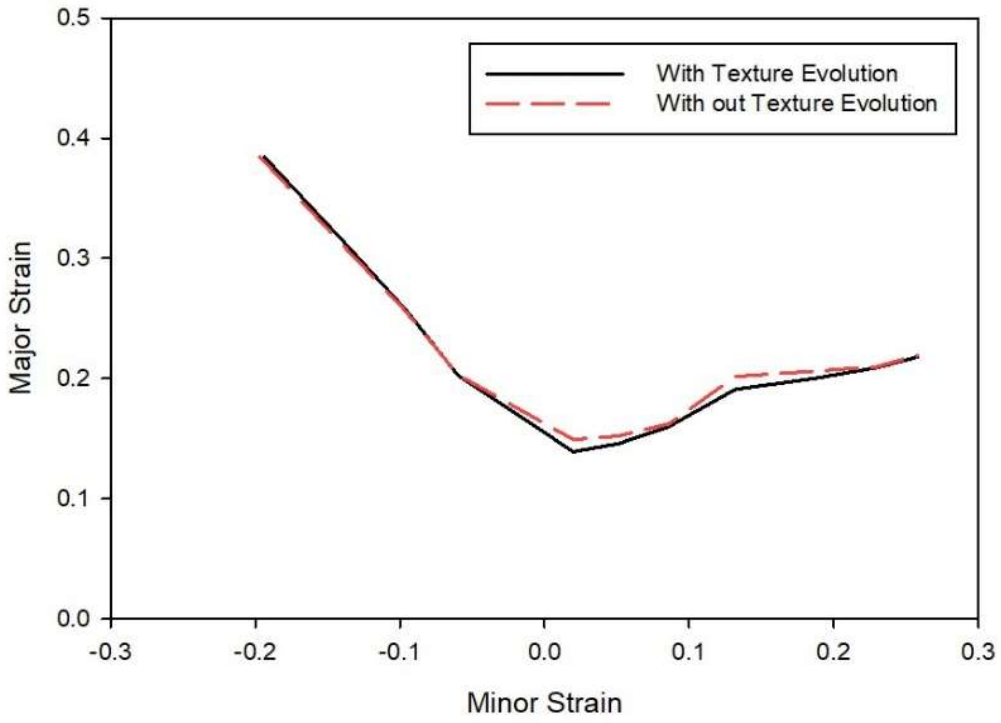

(a) Al6061

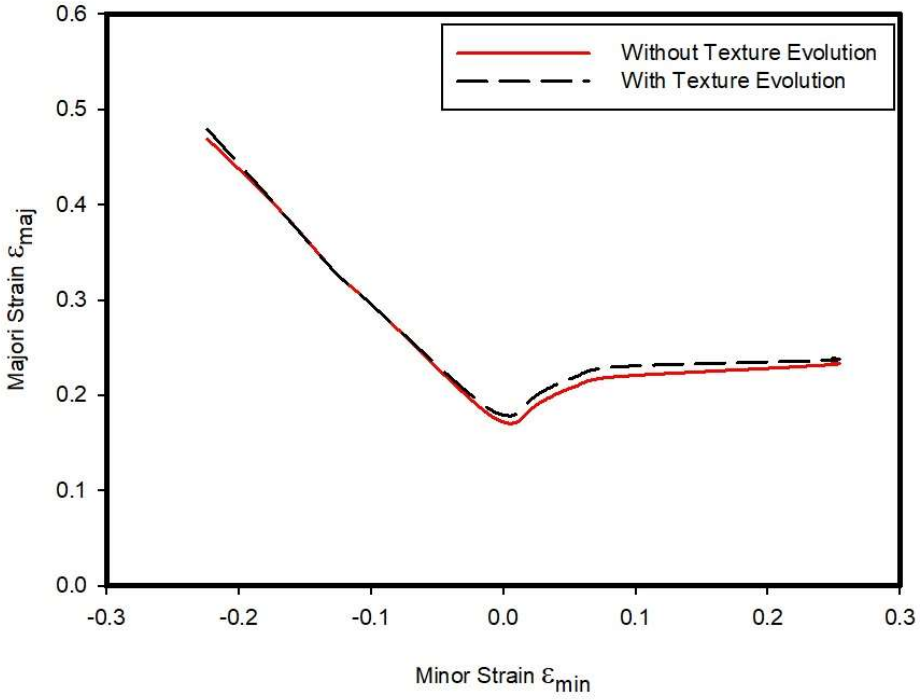

(b) St-14

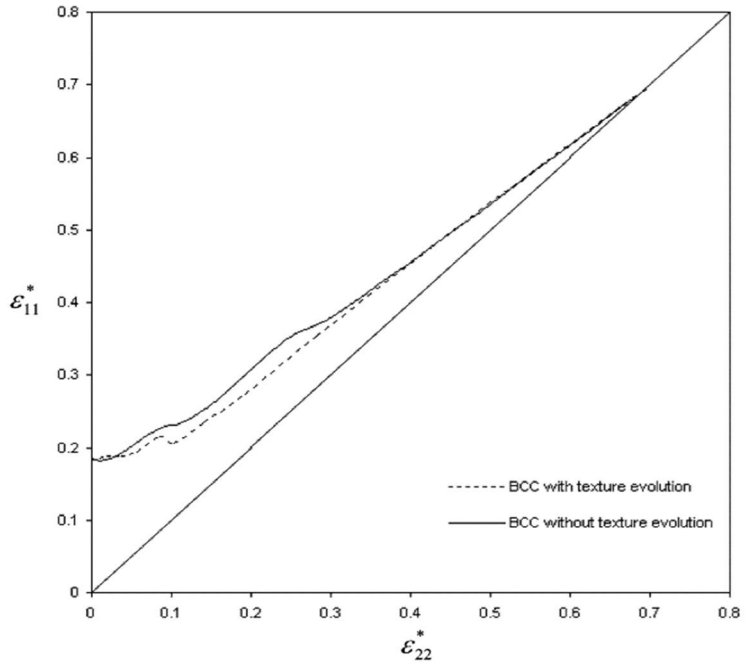

(c) Inal et al., 2005

Figure 70. Effect of texture evolution on FLDs for Al6061

(a) Mianroodi - Al6061 FLD (b) Mianroodi - St-14 FLD (c) Inal FLD (Inal et al., 2005)

4.4 Effect of parallel computing on Abaqus CAE and analysis of CPU time

This simulation procedure needs a large CPU time. So, in order to improve numerical performance (speed of integration point calculation), a Graphics Processing Unit (GPU) parallelization is used. For this purpose, the Nvidia CUDA program is used in this part to make a bridge between CPU and GPU in ABAQUS software. The CUDA user manual shows that ABAQUS has a good compatibility with CUDA software. Two different types of computers are used for these simulations. These computer configurations are shown in Table 5. Generally, direct or iterative methods like Gauss-Sidel, Jacobi, etc are used for solving the parallel program. Also, there are different types of computing structures such as Open Multi-Processing (Open MP) or Message Passing Interface (MPI). Parallel computing is based on MPI in this part. For evaluating parallel computing and the effect of GPU on computing time, the M-K model is simulated for obtaining a FLD with each condition and note a computing time. It means that simulating each node with one computer for 10 different values of the loading ratio, α, and compare the total type in different cases.

	System 1	System 2
CPU	4th Generation Intel®Core™ i7 4790	7th Generation Intel®Core™ i7 7700HQ
GPU	Nvidia Quadro 400	Nvidia Quadro 400
Memory	16 GB DDR3	16 GB DDR4
Hard	1TB SATA 5400RPM	256GB SSD

Table 5. Computers configuration for parallel simulation

Both systems have 1 core to 8 core CPU. A specific GPU is added for the simulation for reducing the CPU time. By investigating these results (see Figure 71), when parallel computing with 8 cores is used, the simulation times are decreased 340.44%. After added GPU to this simulation, the elapsed time is decreased 167.67%. By comparing this result with CUDA white paper results (see Figure 72), benefits of parallelization are shown.

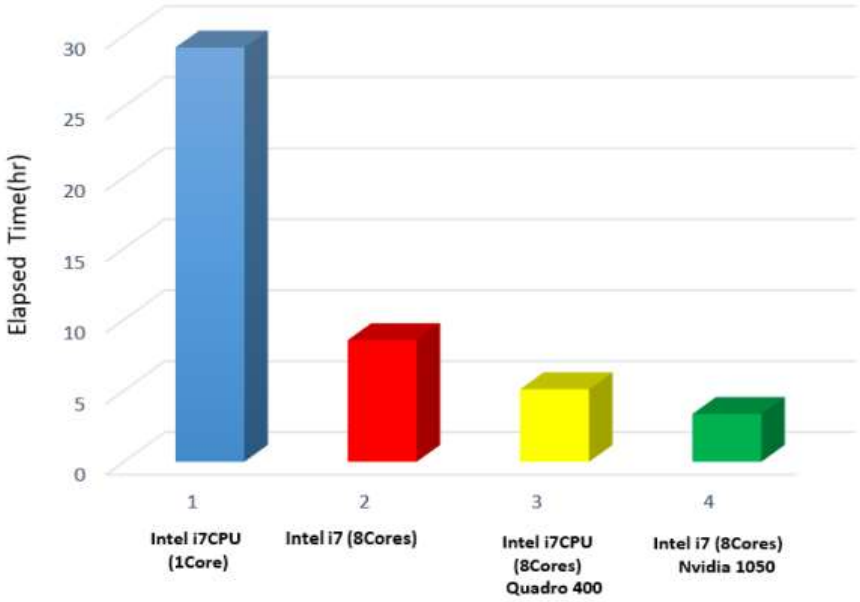

Figure 71. Comparison of simulation times for obtaining FLD

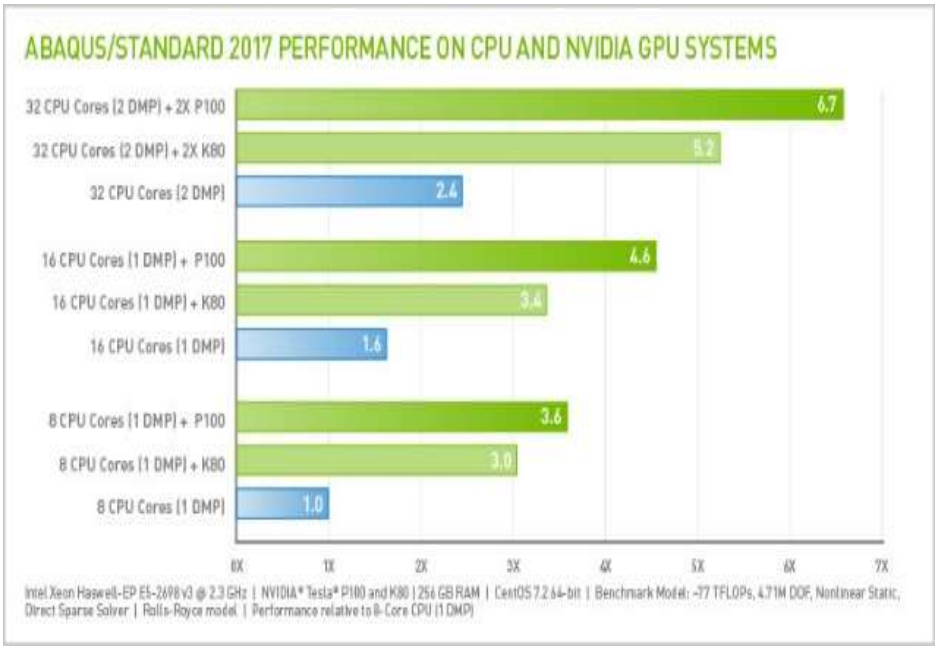

Figure 72. Results from CUDA white paper (Nvidia website)

4.5 Conclusion

In this chapter 4, CPFEM development is used. The crystallographic Taylor model is chosen for its simplicity in this thesis.

The biaxial traction test including the M-K criterion is simulated with CPFEM. The texture evolution for BCC and FCC crystallographic structures are analyzed in safe zone A as well as in the defect zone B for different strain path.

For both crystallographic structures FCC and BCC, the results show that the maximum orientation density is located in zone A. For BCC materials, by increasing the loading ratio parameter, α from 0 to 1, the maximum intensity decreased. On the other hand, for FCC material, the maximum orientation density observed in the perfect zone A increased by increasing α.

The texture evolution did not have a huge effect on FLDs, however, the curve without texture evolution is upper than FLC with texture evolution. The main observable difference between both cases is located at the FLD_0 point.

The time and efficiency of simulations are two important parameters in our study. So, for improving these parameters, parallel computing with GPU is used. Cpu-multi-core and GPU are used to improve the calculation time. In this thesis by using the Cuda Software and Nvidia GPUs the run time is improved. The effects of different CPU and GPU types on the simulation for drawing the FLD are studied in this thesis. The obtained results are quite good and the elapsed time is decreased more than 400%.

References

Barlat, F. (1987). Crystallographic texture, anisotropic yield surfaces and forming limits of sheet metals, Materials Science and Engineering, 91, 55–72. https://doi.org/10.1016/0025-5416(87)90283-7

Barlat, F., Richmond, O. (1987). Prediction of tricomponent plane stress yield surfaces and associated flow and failure behavior of strongly textured f.c.c. polycrystalline sheets, Materials Science and Engineering, 95, 15–29. https://doi.org/10.1016/0025-5416(87)90494

Beaudoin, A., Dawson, P.R., Mathur, K.K., Kocks, F., Korzekwa, D.A. (1994). Application of polycrystal plasticity to sheet forming, Computer Methods in Applied Mechanics and Engineering, 117, 49–70. https://doi.org/10.1016/0045-7825(94)90076-0

Fleck, N. A., Hutchinson, J. W. (1993). A phenomenological theory for strain gradient effects in plasticity, Journal of the Mechanics and Physics of Solids, 41(12), 1825–1857. https://doi.org/10.1016/0022-5096(93)90072-N

Inal, K., Neale, K. W., Aboutajeddine, A. (2005). Forming limit comparisons for FCC and BCC sheets, International Journal of Plasticity, 21, 1255–1266. https://doi.org/10.1016/j.ijplas.2004.08.001

Lorentzen, T., Clausen, B. (1997) A self-consistent model for polycrystal deformation. Description and implementation, 1997. 42 p.

Mashayekhi, M., SHerbaf, H. (2012). Micromechanical modeling of multiphase metals, using a crystal plasticity model, Aerospace mechanics journal, 8(1(27)), 13-27. https://www.sid.ir/en/journal/ViewPaper.aspx?id=270667

Mianroodi, M., Altmeyer, G., Touchal, S. (2019). Experimental and numerical FEM-based determinations of forming limit diagrams of St14 mild steel based on Marciniak-Kuczynski model, Journal of Mechanical Engineering and Sciences, 13(4), 5818–5831. https://doi.org/10.15282/jmes.13.4.2019.08.0464

Nagra, J. S., Brahme, A., Mishra, R., Lebensohn, R. A., Inal, K. (2018). An efficient full-field crystal plasticity-based M-K framework to study the effect of 3D microstructural features on the formability of polycrystalline materials, Modelling and Simulation in Materials Science

and Engineering, 26(7). https://doi.org/10.1088/1361-651X/aadc20

Nix, W. D., Gao, H. (1998). Indentation size effects in crystalline materials: A law for strain gradient plasticity, Journal of Mechanics Physics of Solids, 46(3), 411–425. https://doi.org/10.1016/S0022-5096(97)00086-0

Si, L. Y., Lu, C., Huynh, N. N., Tieu, A. K., Liu, X. H. (2008). Simulation of rolling behaviour of cubic oriented al single crystal with crystal plasticity FEM, Journal of Materials Processing Technology, 201(1–3), 79–84. https://doi.org/10.1016/j.jmatprotec.2007.11.227

Signorelli, J. W., Bertinetti, M. A., Roatta, A. (2019). A review of recent investigations using the Marciniak-Kuczynski technique in conjunction with crystal plasticity models, Journal of Materials Processing Technology. https://doi.org/10.1016/j.jmatprotec.2019.116517

Simulia. (2014). Abaqus User Subroutines Reference Guide, Simulia. http://dsk.ippt.pan.pl/docs/abaqus/v6.13/books/sub/default.htm

Wan, V. V. C., Cuddihy, M. A., Jiang, J., MacLachlan, D. W., Dunne, F. P. E. (2016). An HR-EBSD and computational crystal plasticity investigation of microstructural stress distributions and fatigue hotspots in polycrystalline copper, Acta Materialia, 115, 45–57. https://doi.org/https://doi.org/10.1016/j.actamat.2016.05.033

Wang, F., Sandlöbes, S., Diehl, M., Sharma, L., Roters, F., Raabe, D. (2014). In situ observation of collective grain-scale mechanics in Mg and Mg–rare earth alloys, Acta Materialia, 80, 77–93. https://doi.org/https://doi.org/10.1016/j.actamat.2014.07.048

Chapter 5

Experimental test and validation

5.1 Introduction

To validate the numerical results obtained in previous chapters, several experimental tests have been done. In this chapter 5, the experimental work is divided into 2 different kinds of tests: the biaxial test for flat sheet for BCC materials and the Nakajima test for BCC and FCC materials. The flat sheet is adapted for M-K criteria. The experimental Nakajima test is an out-plane strain test and the biaxial traction test is an in-plane strain test. Aluminum Al6106 is used as FCC material and St14 mild steel is used as BCC material. The specimens manufacturing process and manufacturing machines are explained in this chapter. Digital image correlation cameras are used to obtain the deformation and mechanical properties of specimens. For the biaxial traction test, the deformation is calculated with a dual-lens camera in two directions (ε_{11}, ε_{22}). The experimental FLD is drawn by using these values. The mechanical properties of Al6061 and St14 are calculated with a mono DIC camera in the uniaxial traction test. In this chapter, the crystallographic textures of specimens after each process are investigated by XRD. The experimental textures for the flat sheet with M-K criteria are drawn in two different zones: zone A and zone B. In this part, the textures for two materials Al6160 (FCC) and St-14 mild steel (BCC) are compared. The textures of the Nakajima test for both materials on 3 main points: uniaxial, equibiaxial and plane strain points are calculated and compared together. The micro appearance defects are observed by a digital microscope for flat plat specimens in both zones A and B. The different experimental FLD are compared with numerical FLD in the last part of this chapter and compared with the literature. The objectives of this chapter are obtaining the forming limit diagram for different types of experimental tests for two different material structures (BCC, FCC), micro behavior of metals and comparison of the experimental results with numerical results from chapter 3.

5.2 Strain determination method

In this thesis, two different methods have been used for measuring the deformation. The digital image correlation (DIC) method is used for the determination of displacement field during biaxial tests for flat plate specimens (Rahmatabadi et al., 2019). The second method for the experimental is based on Miller Ruler (Rahmatabadi and Hashemi, 2017) and it is used for the strain calculation during the Nakajima test. This method relies on the grid method (Parks, 1982).

5.2.1 Digital Image Correlation

In recent years, Digital Image Correlation methods have been developed for measuring strain and mechanical properties. Digital images are taken from samples during different loading increments. White and black markings are used to measure the displacement of samples. DIC images have been used to measure the mechanical properties of materials since the beginning of the 1980s (Peters and Ranson, 1982). Peters et al. used a correlation algorithm for a set of pixels between the initial photo and the deformed photos, see figure 73. By improving cameras and other equipment since the early 1990s, this method was also used to measure strain. In recent years, the quality, accuracy and speed of these images have constantly increased, so leading to results that are more accurate.

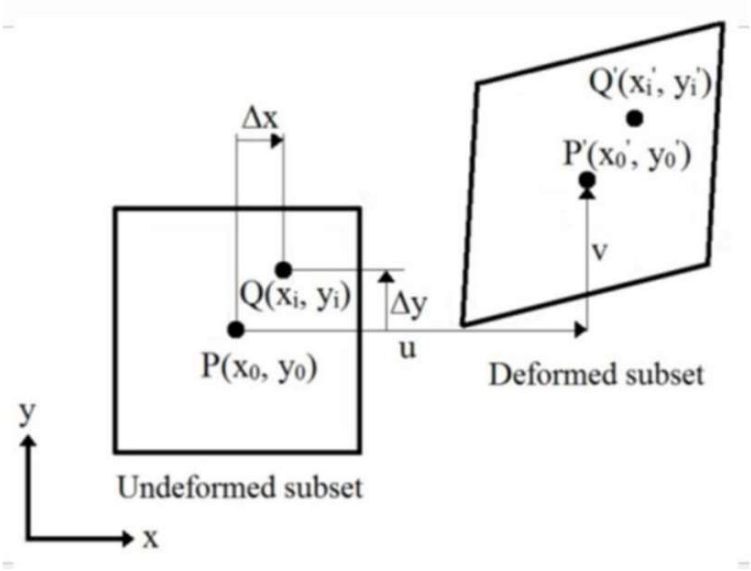

Figure 73. Schematic of the subset in DIC (Rahmatabadi et al., 2019)

Since it is impossible to use a single-pixel to measure the strain value, an area with a large number of pixels is used. The accuracy of this method depends on the number of image pixels in this area. To increase the resolution during the test, the intensity of light must be increased. One of the advantages of this method is the accuracy and high speed in measurement. Also, the system setup is easy to assembly. The displacement of the center of pixels is achieved using the following equations :

$$C(u,v) = \frac{\sum_{i=1}^{m}\sum_{j=1}^{m}[f(x_i,y_i-\bar{f})][g(x_i',y_i'-\bar{g})]}{\sqrt{\sum_{i=1}^{m}\sum_{j=1}^{m}[f(x_i,y_i-\bar{f})]^2}\sqrt{\sum_{i=1}^{m}\sum_{j=1}^{m}[g(x_i',y_i'-\bar{g})]^2}} \quad (5.1)$$

$$x' = x + u_0 + \frac{\partial u}{\partial x}dx + \frac{\partial u}{\partial x}dy \quad (5.2)$$

$$y' = y + v_0 + \frac{\partial v}{\partial x}dx + \frac{\partial v}{\partial x}dy \quad (5.3)$$

In previous equation, $\bar{f}$ represents average reference subset intensity value, $\bar{g}$ is the average intensity value of deformation subsets, u_0 and v_0 are displacement of the subtotal center in x and y directions. Two types of DIC cameras are used in this thesis. The 1D (mono lens) camera is used in the uniaxial traction test for the determination of the mechanical properties of materials. The second type of DIC camera is the 2D (dual-lens) camera. This type of camera is used to determine strain for the biaxial traction test in this study.

5.2.2 Miller ruler

One of the methods for measuring the deformation of specimens uses electrolytic etching. In this method, the positive and negative pole and electrolytic etching chemical dilution are used to create circles on the metal. Two types of grids can be created on the metal surface: 1- Black grids 2- White grids. For marking black grids, the system needs more power than white so the oxide is created on the surface of the metal. The experience shows that the white grid is compatible with aluminum and the black grid is compatible with steel. Figure 74a shows the grids on the specimen. After this step, the specimens are ready for testing. After the test, the circles transformed to ellipses and the diameters of ellipses are measured by using Miller's ruler (Figure 74b) or microscope. The major diameter is called a, minor diameter is called b and the initial diameter is d so the engineering strain is calculated below:

$$\varepsilon_{major} = \frac{a-d}{d} \quad (5.4)$$

$$\varepsilon_{minor} = \frac{b-d}{d} \quad (5.5)$$

so the true strains are calculated below:

$$\varepsilon_{major}^{true} = \ln(1 + \varepsilon_{major}) \quad (5.6)$$

$$\varepsilon_{minor}^{true} = \ln(1 + \varepsilon_{minor}) \quad (5.7)$$

So by drawing each point on the diagram and by fitting a line between these points, the forming limit diagram is achieved.

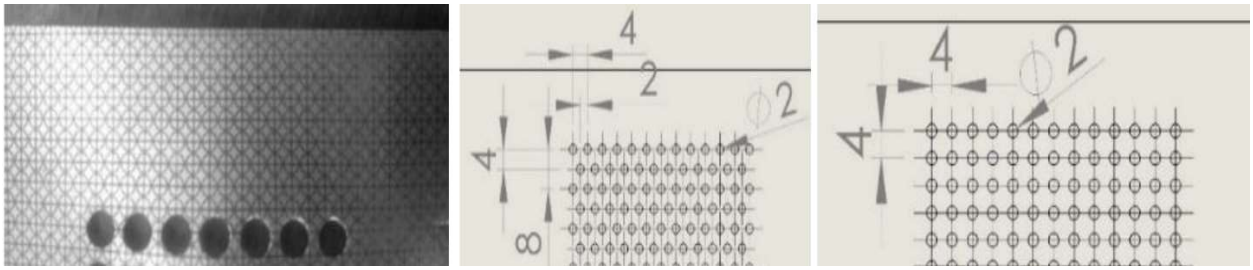

(a)

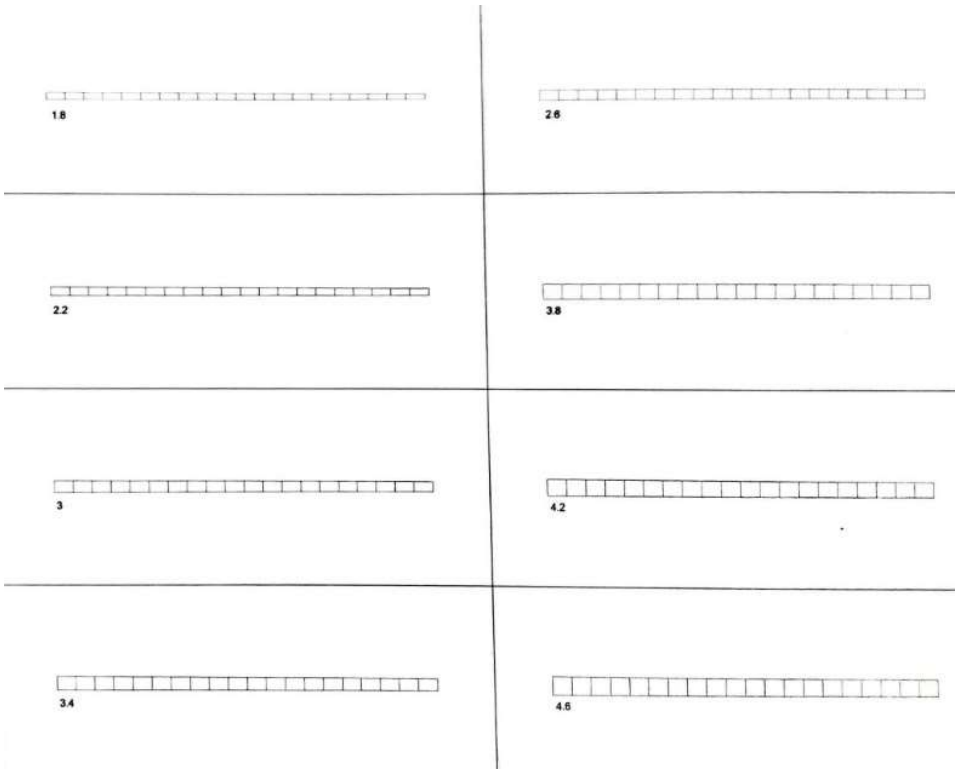

(b)

Figure 74. (a) Circle grids on the specimens (b) Miller's ruler

5.3 Uniaxial traction test

5.3.1 Specimen manufacturing for uniaxial test

In this part, the specimen manufacturing process for the uniaxial traction test is explained. The specimen dimension is shown in Figure 75a (Nguyen et al., 2017; Rahmatabadi et al., 2018). The specimen after laser cutting is shown in Figure 75b. 3D laser cutting is used for cutting these specimens. The important advantages of laser cutting are manufacturing speed and cutting accuracy. The thickness of Al6061 is 0.5 mm and St-14 is 0.7 mm.

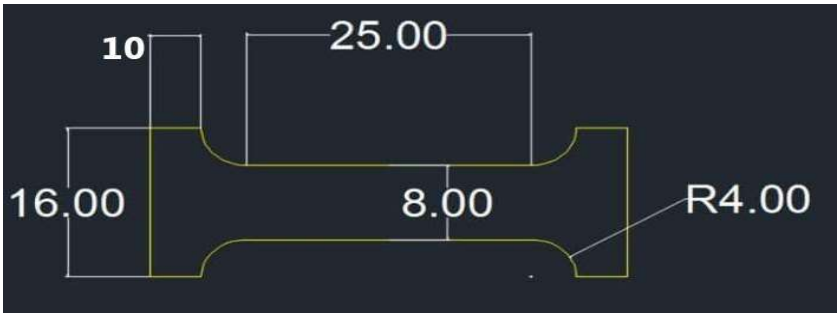

(a)

(b)

Figure 75. (a) Dimension of specimen for DIC test (b) Specimen after laser cutting

5.3.2 Uniaxial traction test mounting

The uniaxial traction test is done at the University of Science and Technology of Iran in Tehran. Santam STM-50 uniaxial traction machine was used for this test. The mono DIC camera is used for determining the mechanical properties of Al6061 and St-14 materials. For each material, 3 different specimens are prepared. The size of these specimens is presented in part 5.3.1. The DIC setup is shown in Figure 76. During this test, the camera takes 60 pictures per minute and the deformation of the specimens during the test is registered on the computer software. After the test, all of the photos are added to the analysis software, the specimen scale is added and all of the displacements and strains are calculated. The speed of this machine during the test is 2 mm/min. The stresses are registered during the test and the stress-strain curve is drawn.

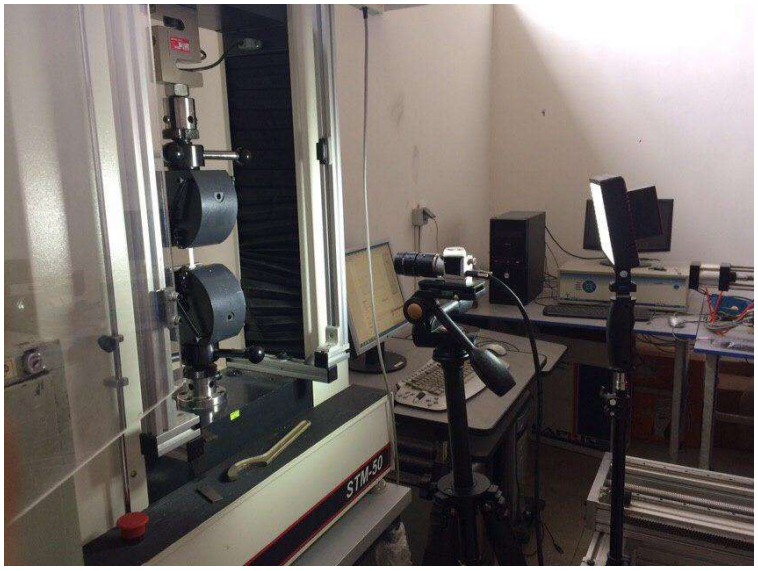

Figure 76. Traction machine STM-50 and DIC setup - University of Science and Technology of Iran in Tehran

The average time until failure for the St-14 specimen is 381 seconds and the average time for the Al6061 specimen is 160 seconds. The failure for the St-14 specimen happened in the middle of the specimen with 45° angle but the Al6061 specimen failed from the upper side with 45° slip. These specimens are shown in Figure 77. The camera can read these changes with a white and black coating. The resolution of the DIC sensor is 2448×2048 pixels.

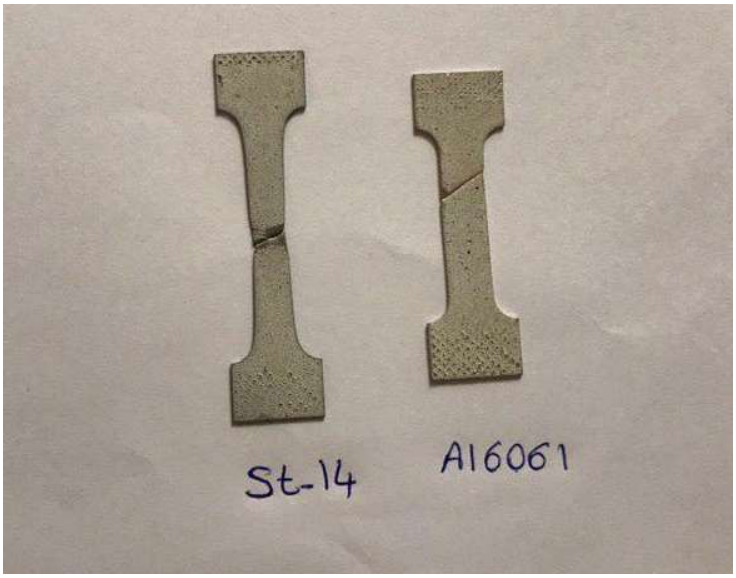

Figure 77. DIC specimens for St-14 and Al6061

5.3.3 Test results for mild steel St-14 and aluminum Al6061

The elastic parameters such as elastic modulus and Poisson ratio are calculated from DIC pictures. The elastic modulus for St-14 is close to 206.2 GPa and the elastic modulus for Al6061 is close to 68.2 GPa. The differences between the test results with data from the company datasheet (St and St, 2008) are due to the manufacturing process. This manufacturing process can increase the elastic modulus (Mesbah et al., 2016). The Poisson ratio for St-14 is closed to 0.32 and for Al6061 is closed to 0.34. Seven pictures from different phases of the test are selected for each material.

The material parameters such as the strength coefficient, yield tensile and ultimate tensile are calculated from the DIC pictures by Mercure X7-2019 software. These parameters can be changed with strain rates but the strain hardening exponent is constant during the test. The strain hardening exponent for FCC materials is higher than BCC materials. The deformation of the specimen for St-14 during the test is presented in Figure 78. The last image is shown at the failure moment.

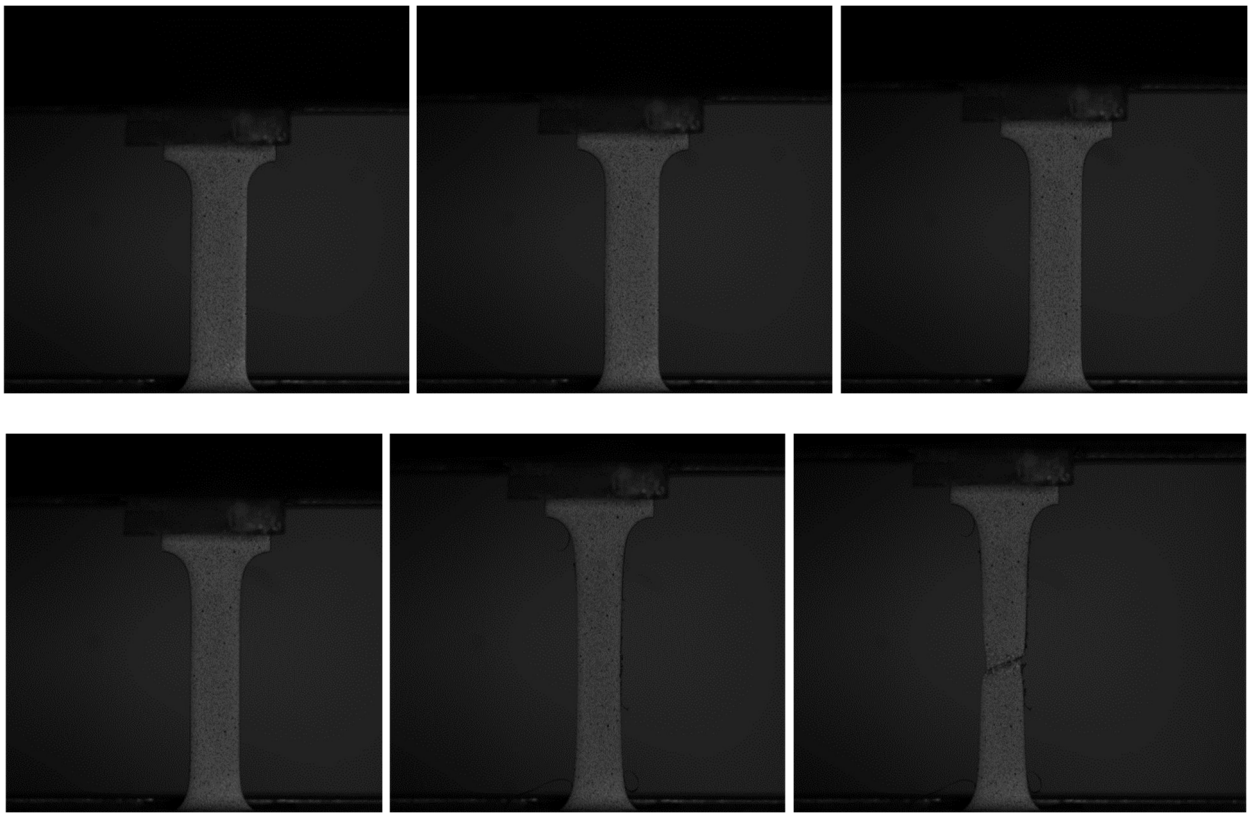

Figure 78. DIC images for St-14 during uniaxial traction test

The DIC photos for Al6061 are presented in Figure 79. We note the necking at the end of the test on the top of the specimen.

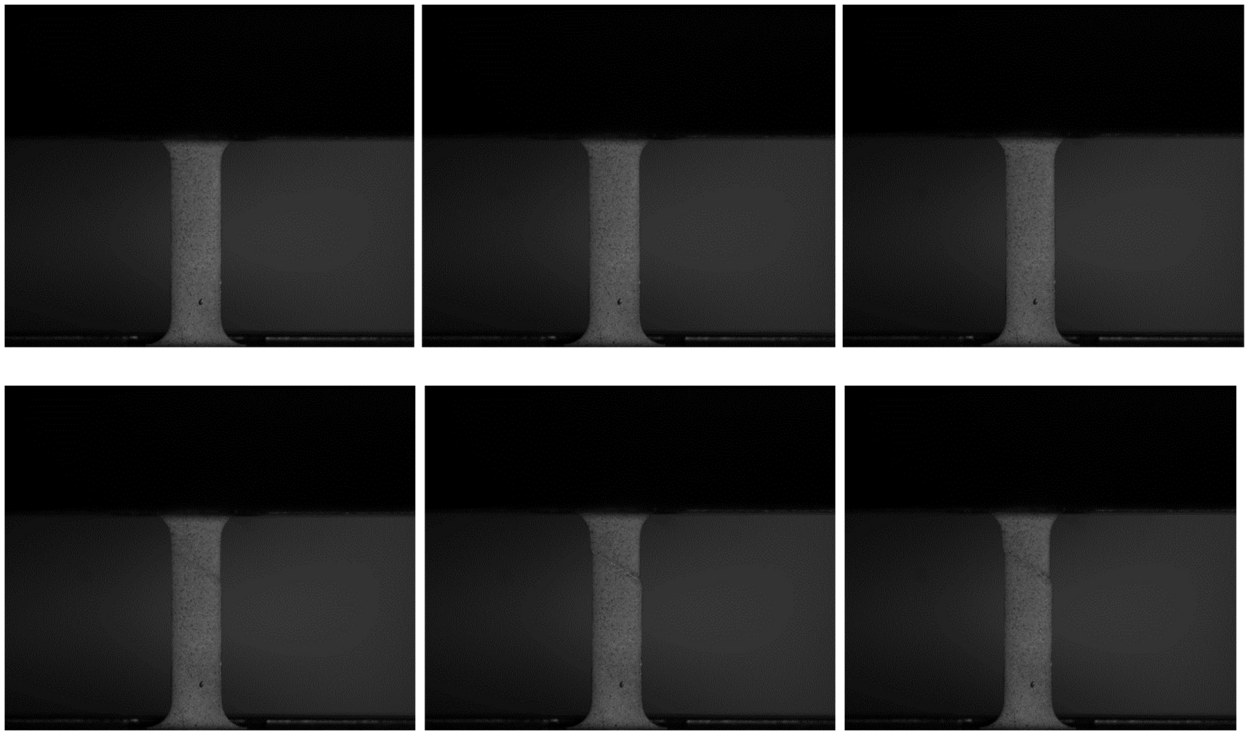

Figure 79. DIC images for Al6061 during uniaxial traction test

The determined mechanical properties of St-14 and Al6061 are presented in table 6. From DIC, the Young modulus and the Poisson coefficient are obtained.

Material	***E***	***ν***	***ρ***	***q***	***n***	h_0
	GPa		***kg/m³***			***GPa***
St-14	206.2	0.32	7860	1	0.21	1.83
Al6061	68.2	0.34	2698	1	0.25	2.02

Table 6. Mechanical properties for St-14 and Al6061

5.4 Biaxial traction test

5.4.1 Specimen manufacturing for biaxial test

The biaxial Marciniak-Kuczynski flat plate test specimen with 180×180 mm dimensions is used (Hashemi et al., 2012). For manufacturing these specimens, a laser cutting machine (3D Max 2009) is used because the control of accurate thickness of the groove zone is important. A classical tool as electrical discharge machine cannot be used because it is not accurate enough.

The laser cutting machine is shown in Figure 80. All of the different parts of manufacturing these specimens were done in CanHood Company (Iran) as a partner of this thesis. Cause of limitation about cutting groove zone, the flat plate experiment test was done for mild steel St-14 only. The thickness of the St-14 sheet is 1 mm in the perfect zone.

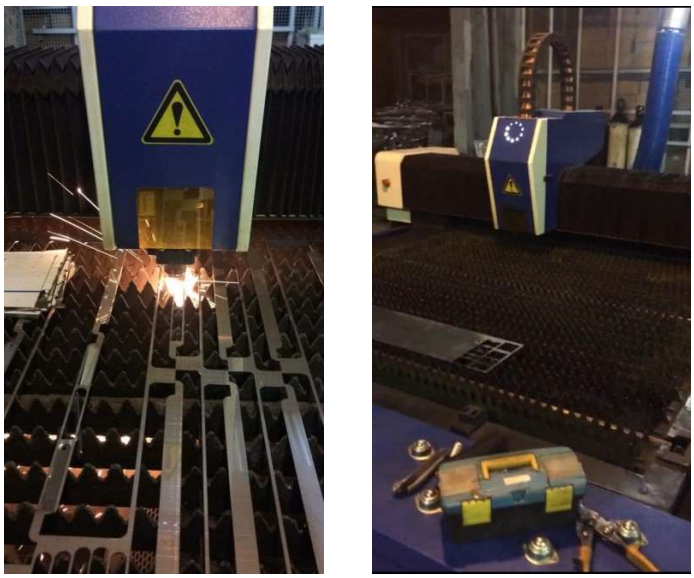

Figure 80. Laser cutting machine in CanHood Company

5.4.2 Biaxial traction test mounting

Biaxial tensile test is used for the prediction of forming limit diagram with Marciniak-Kuczynski approach (Marciniak and Kuczyński, 1967) for St-14 (BCC material). The flat specimens are used in this test. Each tensile specimen with white spray and after that the black spray is used for coating its surface. The digital image correlation method is used to analyze the deformation in this study. The used camera has 2 Lenses (2D camera) and the strains in two different directions can be calculated. The camera model is ARAMIS Camera with 2752×2200 pixel resolution and for analyzing the results, we used GOM software for the biaxial test. The Zwick® biaxial traction test machine was used for these tests (Figure 81). This machine is a 20 kN biaxial machine. The specimen size is 180×180 mm with 1 mm thickness. In each specimen, there is one defect zone B with different thicknesses. In these tests, the initial thickness ratio is equal to 0.95 and 0.99. These specimens are prepared by a Siemens 828D CNC machine.

Figure 81. Zwick biaxial tensile test machine (Zwick, 2018)

For starting the test, 10 N preloaded is applied to the 4 sides of the specimen. On the two opposite sides of the specimen, 400 N are applied. The test is repeated 11 times for 11 different loading ratio α values on the two other opposite sides. This α is changed between 0 and 1 by increments of 0.1. The major and minor strain for each α is one point on the FLD. In this case, a force is applied after the preload step up to 400 N in the longitudinal direction of the sheet during 1.426 s corresponding to a loading ratio α of 0. The force-time curve is shown in Figure 82.

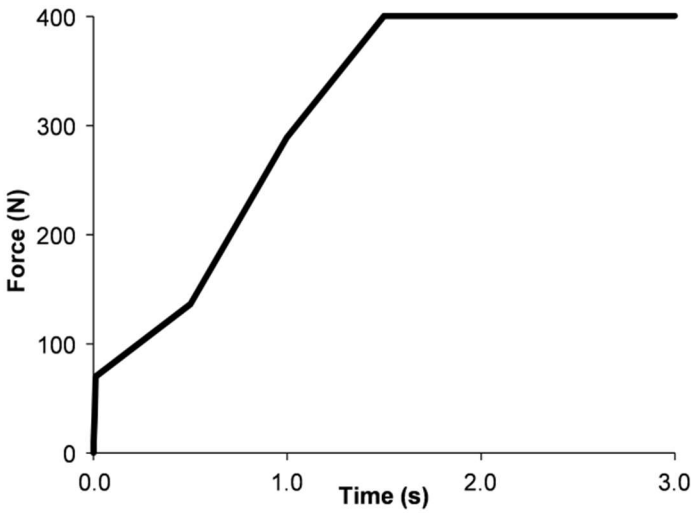

Figure 82. The force-time curve for the experimental test

5.4.3 Determination of experimental FLD

The experimental minor and major strains for different points on the perfect zone A are calculated by GOM software from DIC photos. The biaxial test is continued until the fall point on the force-displacement curve. With this biaxial test, the in-plane strain is calculated using a flat plat specimen. The maximum deformations during the tests occur in defect zone B so the necking is started from this zone.

For BCC, the experimental FLD for different f_0 is shown below, see figure 83. For each experimental test, there are several points on the FLD and by fitting the curve between these points, the FLC is found for each test. These tests show that the FLD are going up by increasing the f_0 values. The FLD_0 (plane strain point) for $f_0 = 0.95$ is closer to 0 on the minor strain axis than f_0=0.99. The formability of St-14 with $f_0 = 0.99$ is higher than with $f_0 = 0.95$.

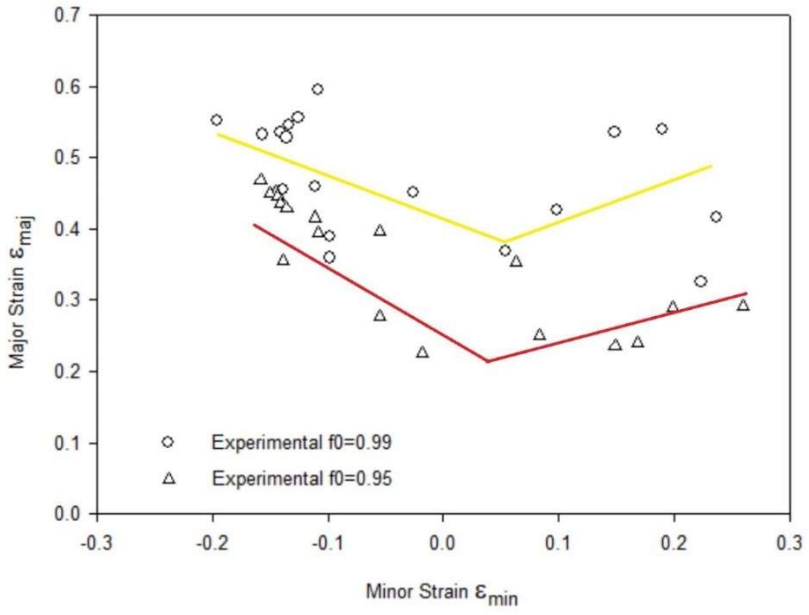

Figure 83. Experimental FLD for St-14 flat-plate specimens under biaxial test

5.4.4 Experimental textures

In the next study, the grain orientations are investigated in zone A and zone B by XRD at the University of Tehran. This XRD evaluation is done for 19 different points on the samples. For defect zone B, the analysis is done in the middle and in the upper zone in order to check the homogeneity of the texture inside the defect zone.

The textures are drawn in (221) plane and represented in figure 84 at the necking strain value. Figure 85 represents the texture intensity for 19 different points for the St-14 specimen.

We note that in zone B, the crystallographic textures are quite heterogeneous and also depend on the location: middle or upper zone. In upper zone B, the boundary condition may perturb the distribution of texture and should be taken into account with care. The textures in zone A are more pronounced than in the middle of zone B. The intensity of texture in zone A is more important than in the middle of zone B. Zone B constitutes a perturbation zone and that may explain the difference of texture with the more stable zone A.

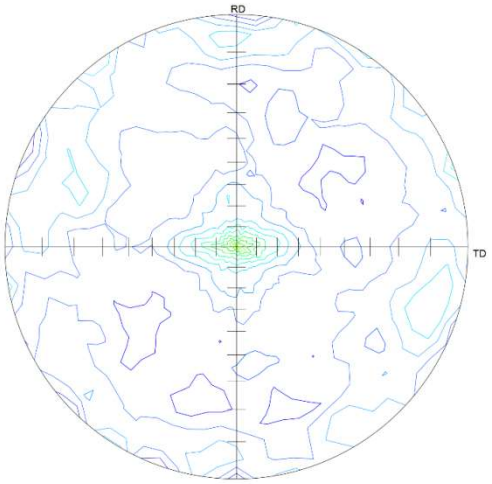

(a) Zone A

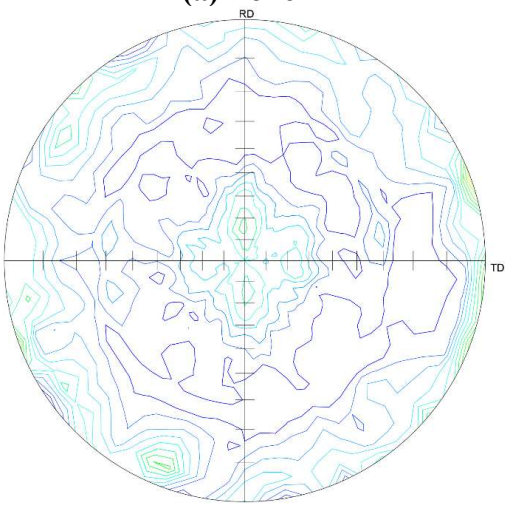

(b) Middle of zone B

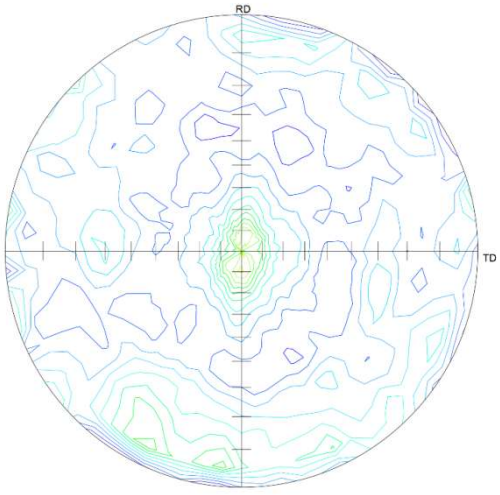

(c) Upper side of zone B

Figure 84. Experimental (221) pole figures for St-14
(a) Zone A (b) middle of zone B (c) upper side of zone B

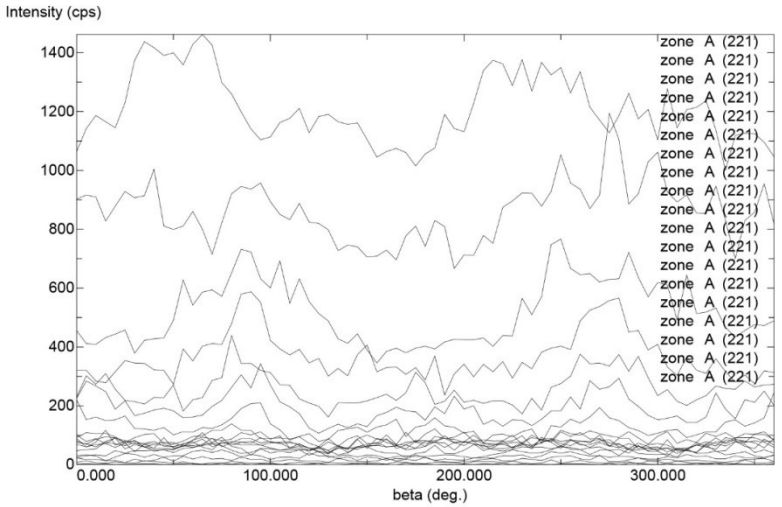

(a) Zone A

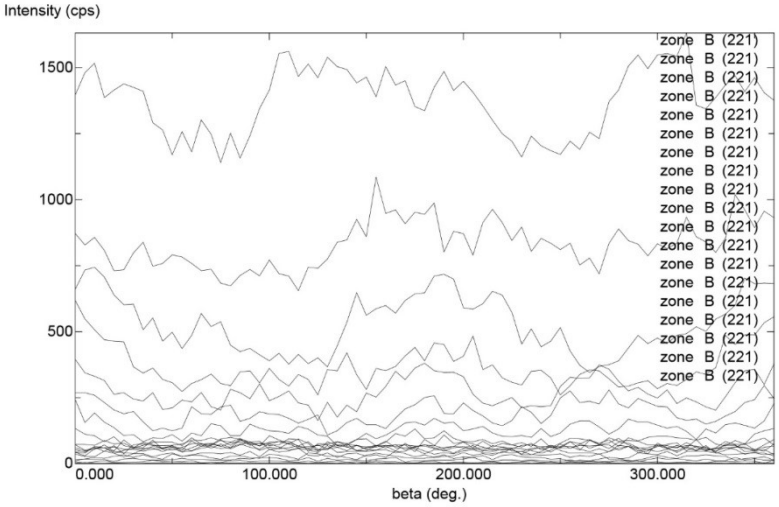

(b) Middle of zone B

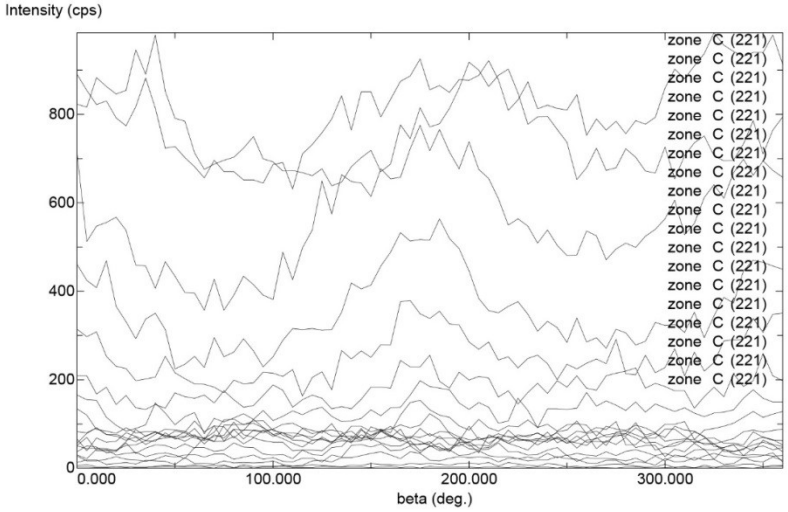

(c) Upper side of zone B

Figure 85. Texture intensity for 19 different points for St-14
(a) Zone A, (b) Middle of zone B, (c) Upper side of zone B

5.4.5 Microscopic surface defect

In this part, the surface of specimens is show in different zones. Each specimen has 2 different parts, first zone is the perfect zone A and the second zone B is the defect zone. In this thesis, Splaks 1000x High Power USB Digital Microscope is used for investigating the effect of cracks on the surface of the specimens. The cracks appeared in defect zone B. The surfaces of the specimens are shown in Figure 86 for zone A and zone B after the failure of the specimen.

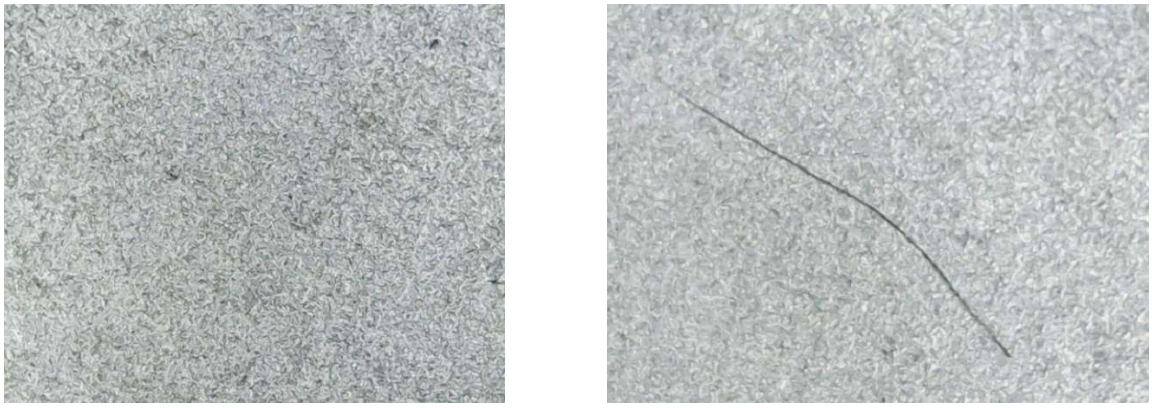

(a) zone A **b) zone B**

Figure 86. Surface zones under the microscope (x 500) for St-14 B

(a) zone A (b) zone B

The initial thickness of the specimen is 1 mm in the perfect zone A but in the imperfect zone B, the initial thickness is 0.99 mm. During the test, the thickness is decreased. The equation below shows the stop criteria (Evangelista et al., 2002) during the numerical study in this thesis :

$$S_{MK} = \frac{\epsilon_{33}^{A}}{\epsilon_{33}^{B}} \tag{5.8}$$

The numerical simulation is stopped when S_{MK} is less than 0.8. The thicknesses are measured in perfect zone A and in imperfection Zone B. The measured S_{MK} varied between 0.758 to 0.846. S_{MK} in experimental tests and numerical values are closed.

5.5 Nakajima Test

5.5.1 Specimen manufacturing for Nakajima test

The Nakajima test specimens are manufactured in eight different shapes from Al6061 and St-14 materials (ISO 12004-2, 2008). The different sizes of these specimens are shown in Figure 87. The thickness of Al6061 is 0.5 mm and for St-14 is 0.7 mm.

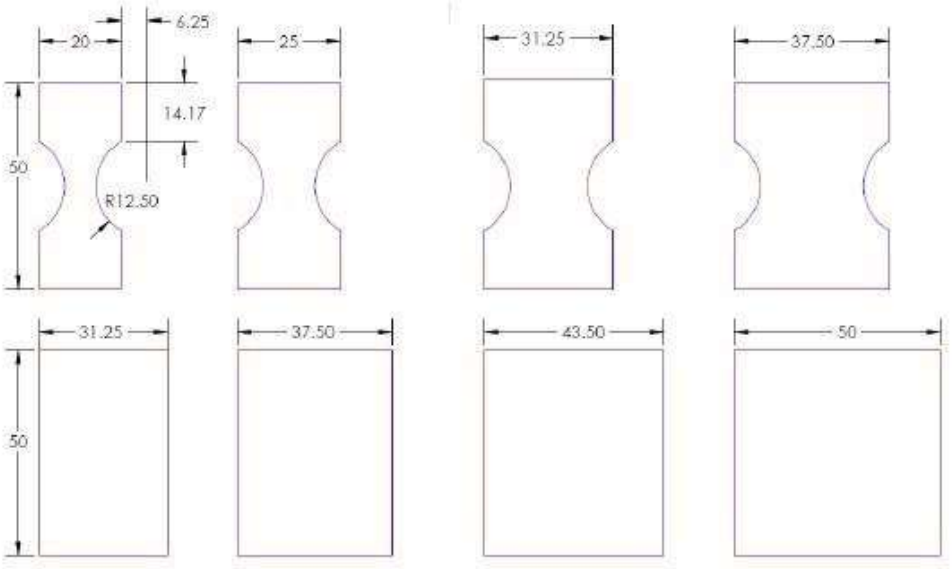

(a)

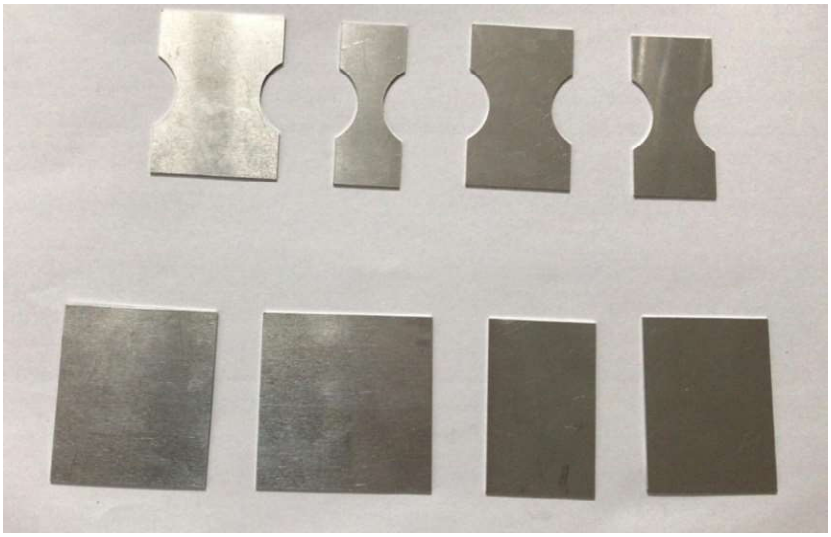

(b)

Figure 87. (a) Nakajima specimen dimension (Hashemi et al., 2012) (b) Al6061 Nakajima specimen after laser cutting

5.5.2 Nakajima test mounting

Nakajima test is a type of deep drawing test to determine the out-plane strain. One of the best way to determine the experimental forming limit diagram is the Nakajima test. The schematic of the Nakajima test is shown in Figure 88a. In this thesis, forming limit diagrams for St-14 and Al6061

are drawn by the Nakajima test. The test is done at 25°C. This test is done at Iran University of Science and Technology, by respecting to ISO 12004 Standard (Motamedi and Hashemi, 2019). For applying the forces on the specimens, Santam STM-50 (Figure 88b) uniaxial machine is used.

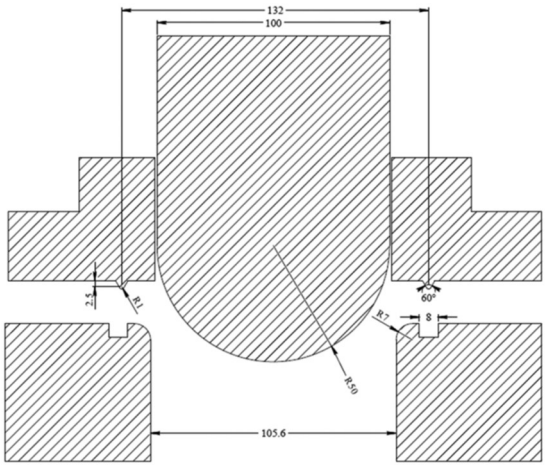

(a)

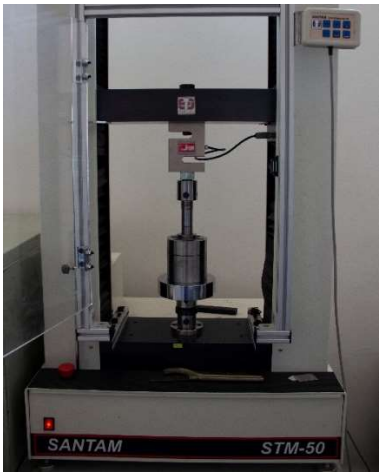

(b)

(c)

Figure 88. (a) Schematic of Nakajima punch and die (b) Santam STM-50

(c) Nakajima punch and die model

The advantages of this machine are accurate load cell (class 0.5), capacity of 5000 kg, constant speed control at the range 0.001-1000 mm/min, real-time and advanced speed control through the methods and repeatability of results. A punch with a 50 mm diameter is used for this test. The

lower and upper dies are fixed by six M6 screws (Figure 88c). The data from this test is registered on the computer with Santam software.

This test is done with 8 different specimen sizes so each specimen is one point on the forming limit diagram. The test will continue until necking. The necking is determined from the force-displacement curve. When the curve decrease from the maximum force value it means that the necking occurred and the force is decreased and the test is stopped.

5.5.3 Determination of experimental FLD for mild steel St-14 and aluminum Al6061

- Results for mild steel St St-14

The result of the Nakajima test is registered on the Santam software which exports the stress, time and force, see Figure 89. By calculating minor and major strains near to necking zone (see Figure 90), the forming limit is drawn. The results are shown below:

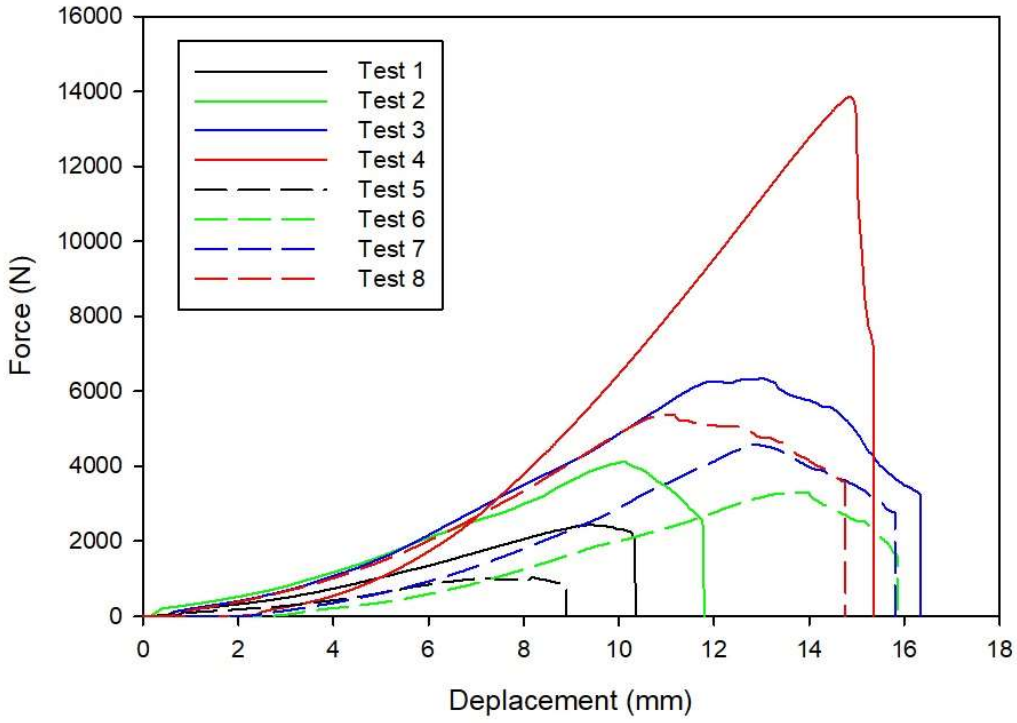

Figure 89. Force-Displacement curve for mild steel St St-14

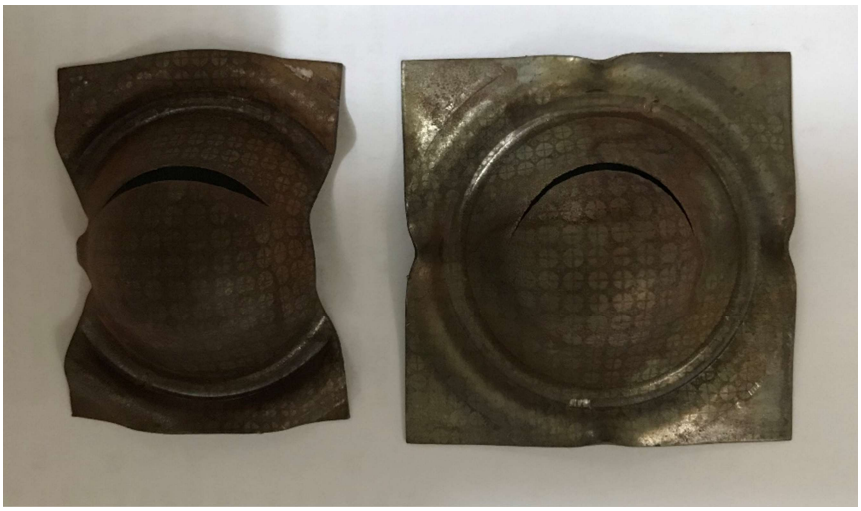

Figure 90. St-14 specimens after the test for mild steel St St-14

The forming limit diagram is shown in Figure 91. The maximum time is 14.9 minutes for test number 6. The major strain in the uniaxial point is very high so the strain in this part of FLD in the X direction is the highest value for St-14. On figure 91, we note that the plane strain point (FLD_0) is moved to the right side of the figure. This is due to the fact that the specimen slips during the test.

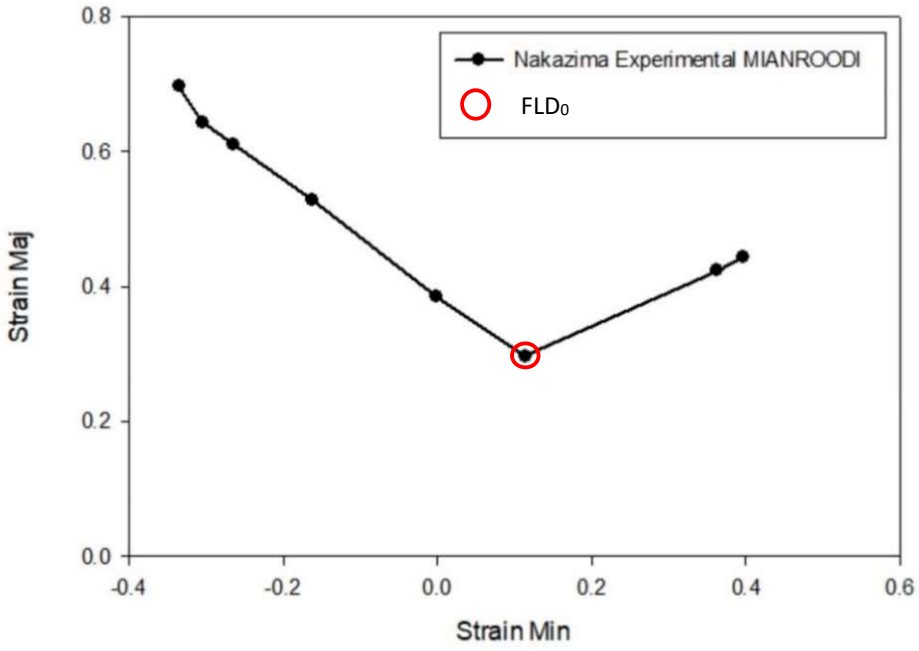

Figure 91. Experimental FLD for St-14 using Nakajima test

- Results for aluminum Al6061

Figure 92 shows the force-displacement curve for aluminum Al6061. We note that maximum force for St-14 is 6.2 times more than the maximum force for Al6160. It means that the St-14 can carry force more than Al6061. So the time for achieving the necking for St-14 is more than Al6061. The maximum time is 4.6 minutes for test number 8 (last point in FLD). The maximum test time for St-14 is 3.23 more than Al6061.

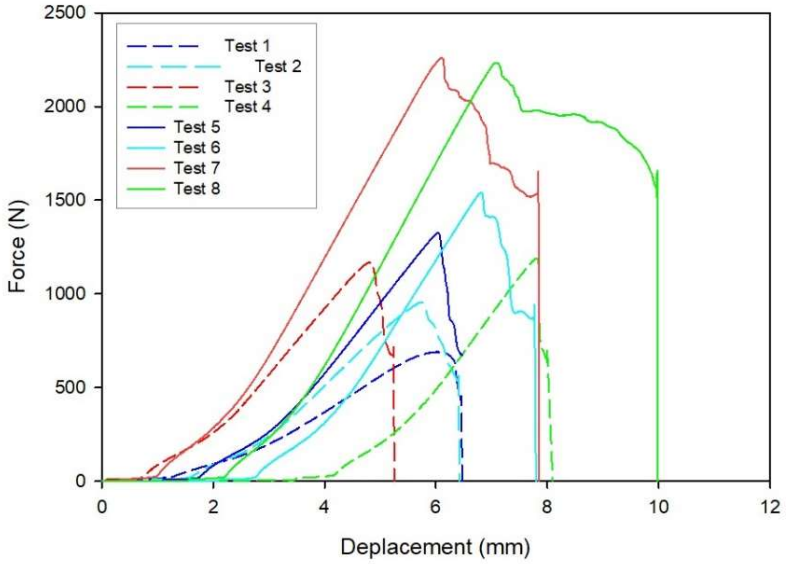

Figure 92. Force-displacement curve for aluminum Al6061

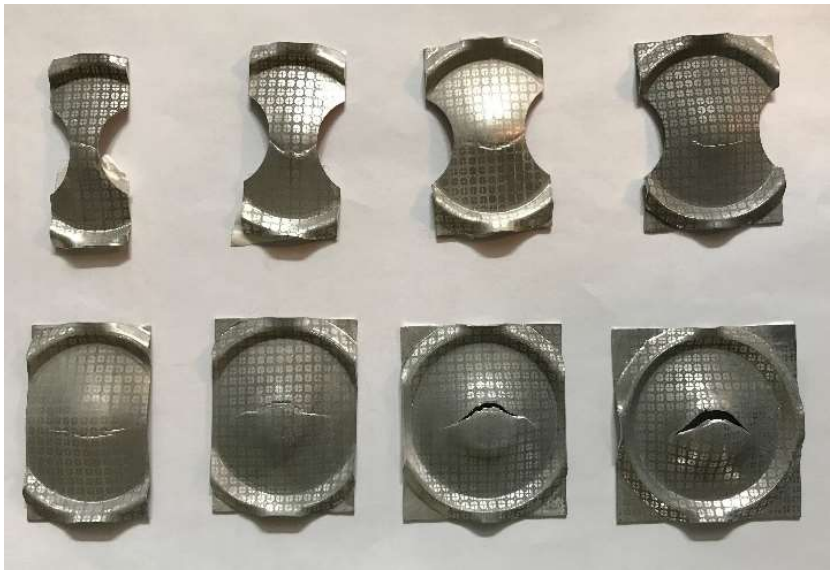

Figure 93. Specimens after the test for aluminum Al6061

The Al6061 specimens after the Nakajima test are shown in Figure 93. In the next step, the FLD is drawn for Al6061 in Figure 94. The FLD_0 for Al6061 is close to 0. The necking occurred sooner than St-14 so the model needs less force and the specimen does not move during the test. By comparing FLD_0 for Al6061 and St-14 understood that FLD_0 for Al6061 is 89.3% closer to 0 than FLD_0 on St-14 forming diagram.

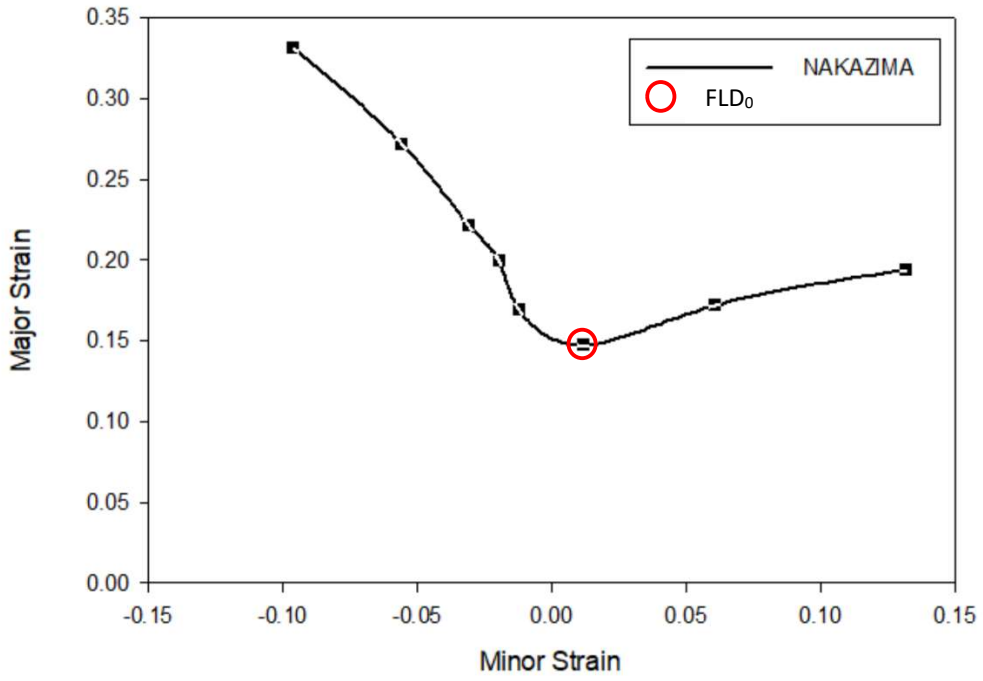

Figure 94. Experimental FLD for Al6061 using Nakajima test

5.5.4 Experimental textures for mild steel St-14 and aluminum Al6061

This part of the thesis investigated the textures of St-14 and Al6061 for different strain states of the Nakajima test. The textures are characterized by XRD (X-ray Diffraction) method. Three different points on the FLD are chosen to study the textures: uniaxial, equibiaxial and plane strain points. All of the measurement of textures is done at the University of Tehran with Philips X'PertX-ray Diffractometer system. The radiation angle is 0.02 degrees with the first time step.

Schulz's reflection method (Chateigner et al., 1992) is used for XRD texture analysis. The XRD analysis with Cu radiation is used. The X-ray worked on 40 kV with 2θ equal to 65.1974 degrees. The average crystalline size for these specimens is measured around 152.68 nm.

- Results for aluminum Al6061

The Al6061 textures are presented in figure 95 and the corresponding intensities are plotted in figure 96 for 19 different points on the samples. The textures for Al6061 are drawn in (220) plane on the RD-TD transverse plane. As expected, differences in textured are noted as function of strain path which is a predictable results since textures are dependent on strain path.

The maximum picks for the uniaxial point (Figure 96a) occur at 2 points. After 100 degrees and close to 300 degrees are picks of the curve. In-plane strain point (Figure 96b), one major pick occurs. This point is close to 100 degrees. In the equibiaxial point, two picks occur.

- Results for mild steel St-14

The next part is texture investigation for St-14. As in the previous part, three points are chosen on the FLD and 3 specimens are used for XRD.

The textures for St-14 are shown in Figure 97. The first figure 97a is the texture for the uniaxial point, the second figure 97b is the plane strain point and the third figure 97c is the equibiaxial point. These textures are drawn in (220) plane. The intensity of the grains orientations is shown in figure 98. As for Al6016, differences in textures and intensities are noticed as function of strain path.

- Comparison between mild steel St-14 and aluminum Al6061

The main aim of this comparison is the difference between the grain orientations during Nakajima tests for BCC and FCC material structures. We note that textures are more diffuse for St-14 (BCC) than for Al6016 (FCC). The intensity is greater for Al6016 (FCC) than for St-14 (BCC). However, we note two or three picks for both materials but at different intensity level and different angles location.

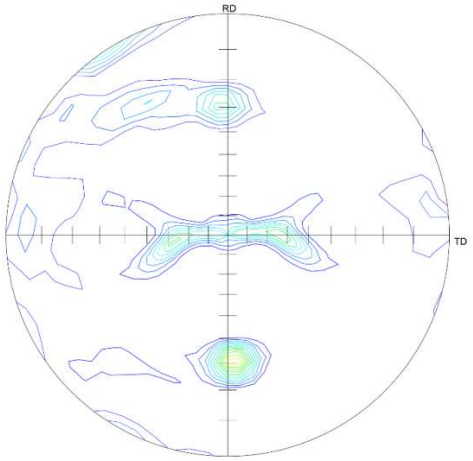

(a) Uniaxial point

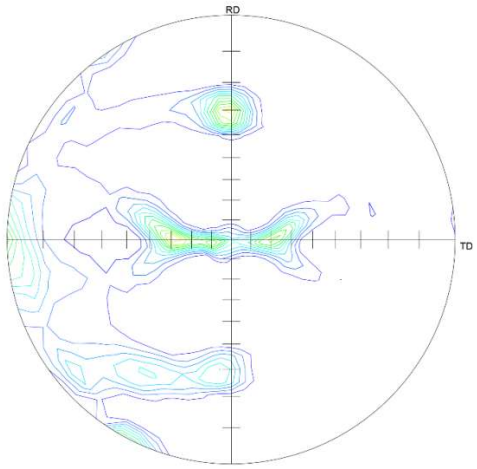

(b) Plane strain point

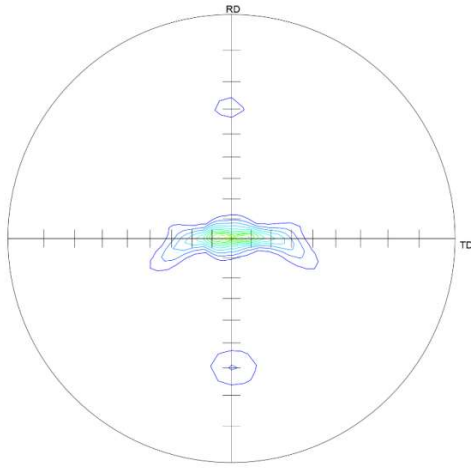

(c) Equibiaxial point

Figure 95. Experimental (220) pole figures for Al6061
(a) Uniaxial point (b) Plane strain point (c) Equibiaxial point

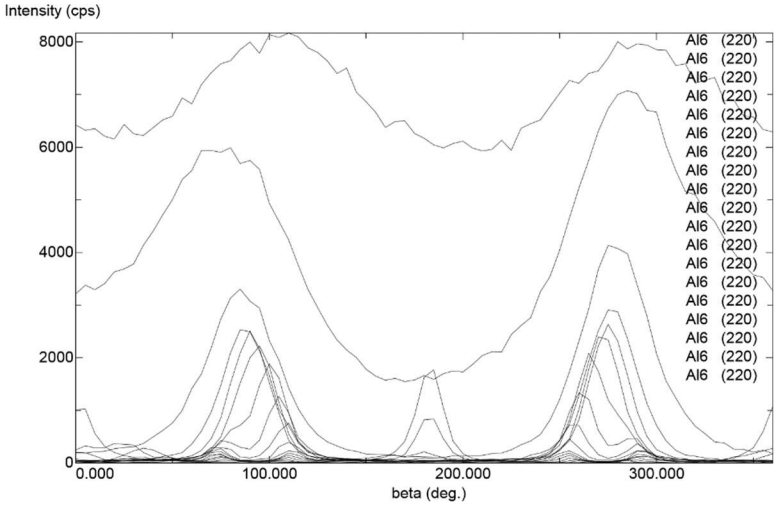

(a) Uniaxial point

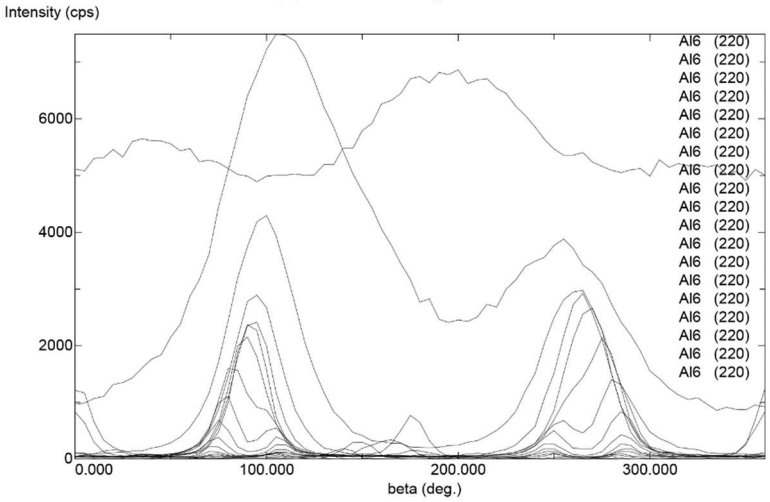

(b) Plane strain point

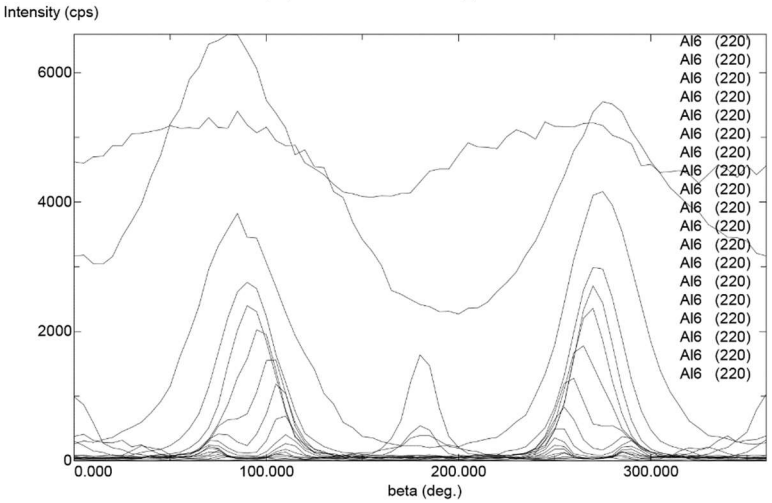

(c) Equibiaxial point

Figure 96. Texture intensity for 19 different points for Al6061 (a) Uniaxial point (b) Plane strain point (c) Equibiaxial point

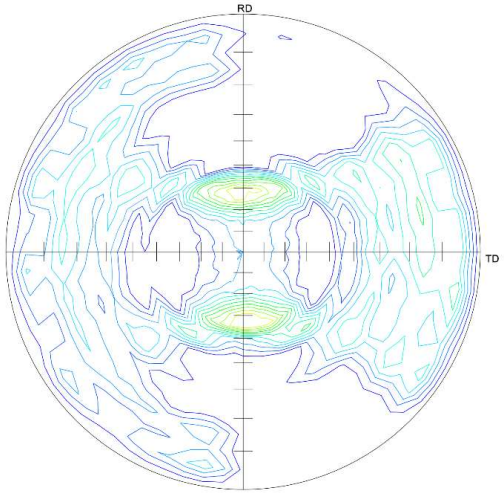

(a) Uniaxial point

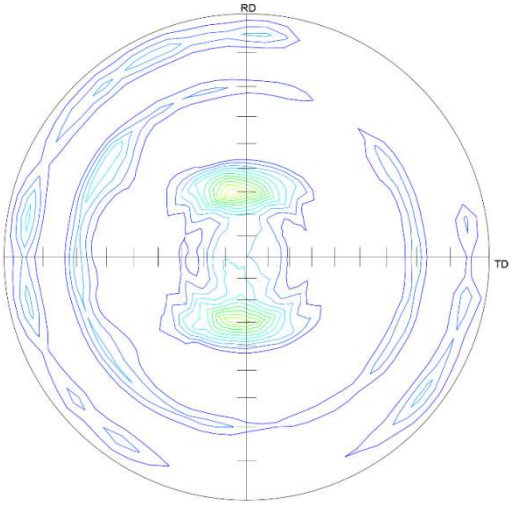

(b) Plane strain point

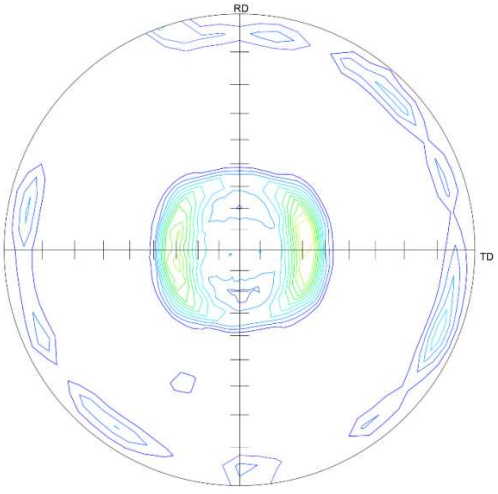

(c) Equibiaxial point

Figure 97. Experimental pole figures (220) for St-14
(a) Uniaxial point (b) Plane strain point (c) Equibiaxial point

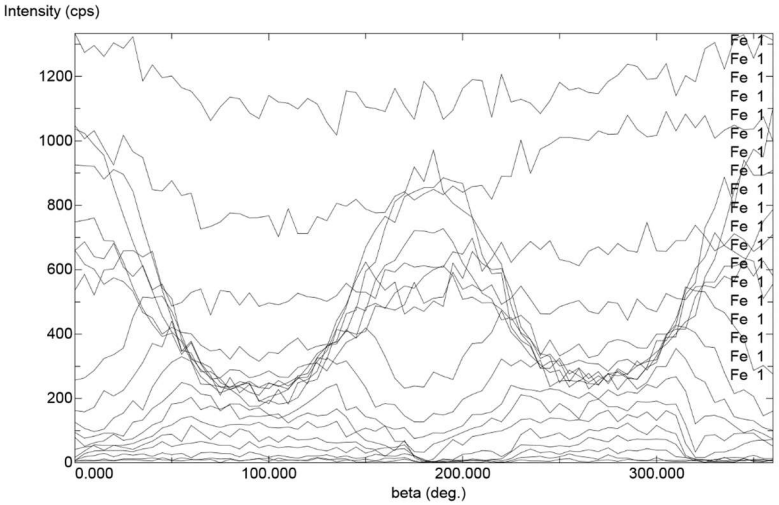

(a) Uniaxial point

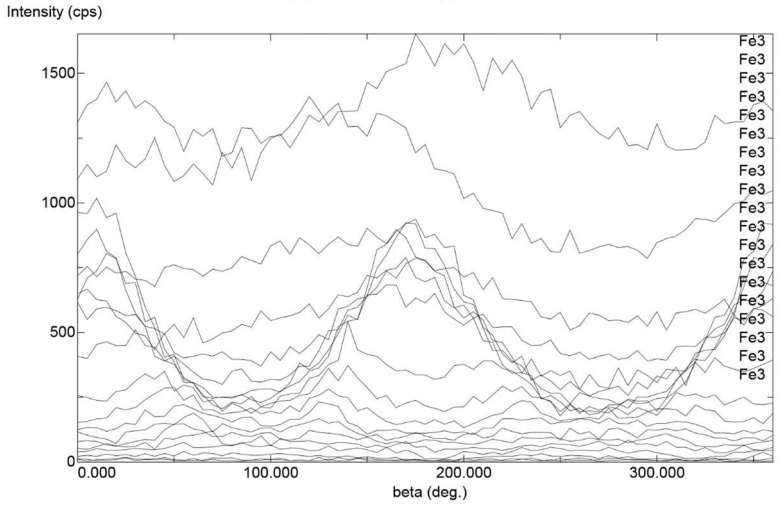

(b) Plane strain point

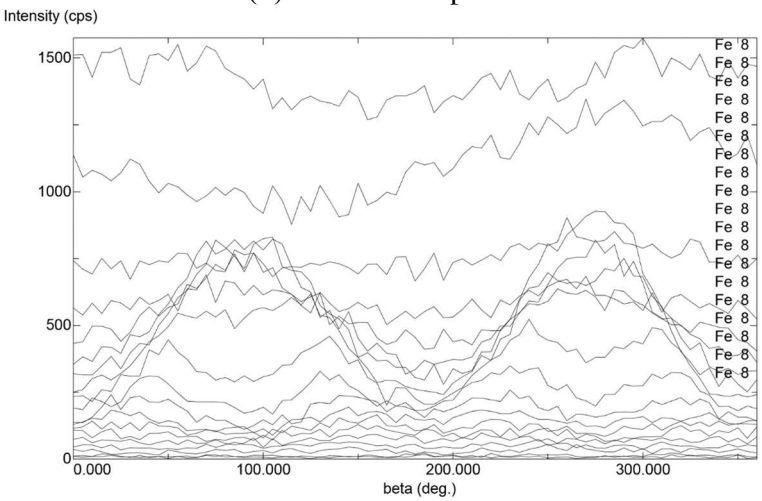

(c) Equibiaxial point

Figure 98. Texture intensity for 19 different points for St-14 (a) Uniaxial point (b) Plane strain point (c) Equibiaxial point

5.6 Comparison between numerical and experimental FLD for mild steel St-14

In this chapter 5, two types of tests are done for St14 a BCC material. Figure 99 represents different experimental and numerical FLDs for St-14. The fitting line for a flat plate of experimental FLD is upper than the numerical results.

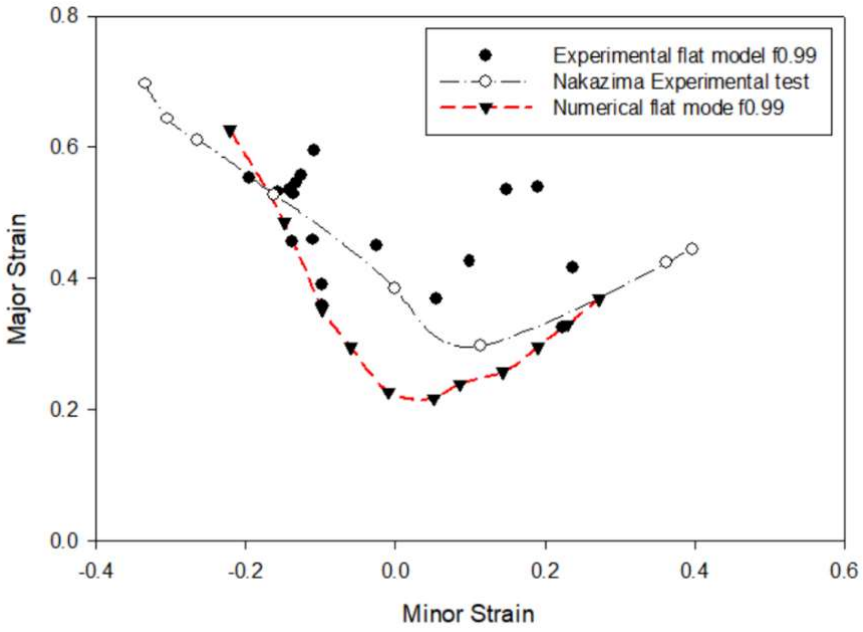

Figure 99. FLD for St-14 numerical and experimental flat model and Nakazima experimental test

Figure 99 shows that the FLD_0 for numerical simulation occurs close to 0 on the minor strain axis but for Nakajima and the experimental flat model this point move to the right side of FLD. The major strain on the FLD_0 point for the numerical flat plat is lower than the Nakajima test. All the experimental points are upper of numerical FLD.

The experimental and numerical results from this research are compared with Ghazanfari's and Habibi results (Ghazanfari et al., 2016; Habibi.et al., 2017). Figure 100 shows that our numerical results have a good correlation with article results.

The uniaxial point (UT) in both simulations is quite close. The Habibi UT point is 2.01% bigger than our simulation results on the minor strain axis.

The Habibi FLD_0 point (PT) is 11.49 % higher than our result. The article FLD_0 point is closer to 0 than our results. Higher f_0 = 0.991 value in Habibi simulation is the main reason for the difference. The f_0 in the Habibi simulation is 0.2% higher.

The article minor strain at Equibiaxial point (EE) is 20.16% higher than our results but the article major strain at Equibiaxial point (EE) is 1.76% smaller than our simulation.

The experimental results for both studies show that the formability of St-14 on the experimental test is higher than the numerical simulation. Habibi result shows at a uniaxial point, the result is not quite closed with our numerical and experimental test. The reason for this difference is how the experiment was performed (Habibi et al., 2017).

All of our numerical modeling results are in the safe area of the experimental forming limit diagram.

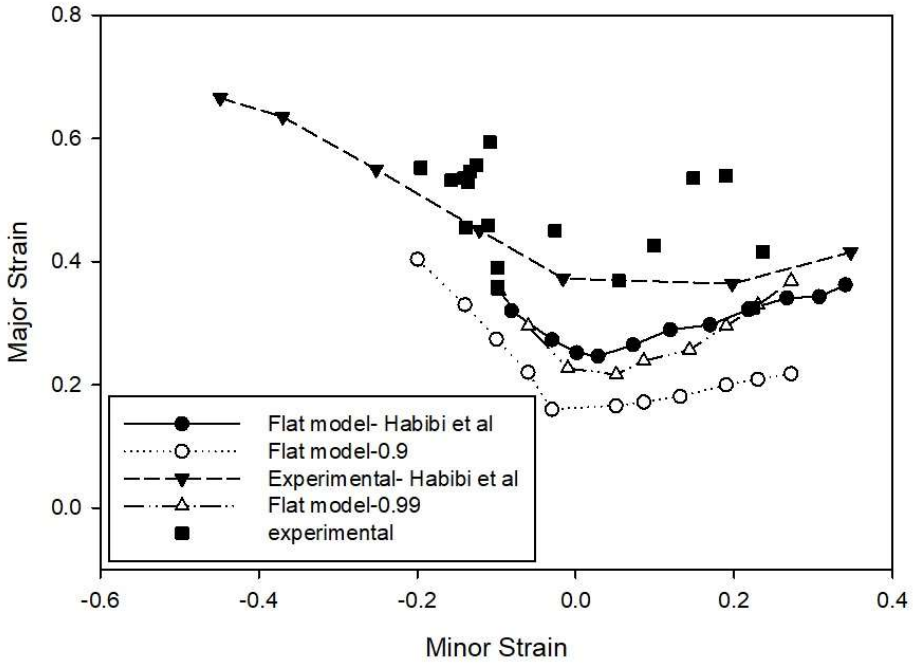

Figure 100. Mianroodi and Habibi FLD for St-14 numerical and experimental (Ghazanfari et al., 2016; Habibi.et al., 2017, Mianroodi et al., 2019)

5.7 Conclusions

In this chapter 5, several experimental tests have been done in order to validate the numerical results of previous chapter 3. The biaxial test and Nakajima test are used to obtain FLD. Classical uniaxial test is used to obtain materials parameters for mild steel St-14 and aluminum Al6061. Using DIC or Miller ruler, strain are determined. In this chapter, an analysis of crystallographic textures for FCC and BCC is also done using XRD method.

The results in this chapter show a quite good correlation between the numerical and experimental tests for FCC and BCC materials. The FLD results from the Nakajima test show that the formability of BCC materials is higher than FCC materials on the out-plain strain and that the texture intensity of the grains for BCC materials is lower than FCC materials.

The main discrepancies between results are due to different methods of determination and experimental setup. As example, the differences for FLD_0 between the Nakajima test and experimental and numerical flat model is due to the problem of specimen fixing between the die and sheet holder for the Nakajima test. St-14 specimens move during the test because of the high punch force. These differences in FLD_0 for BCC materials are more visible than FCC materials because of the high formability value.

References

Chateigner, D., Germi, P., Pernet, M. (1992). Texture analysis by the Schulz reflection method, Defocalization corrections for thin films. Journal of Applied Crystallography, 25(pt 6), 766–769. https://doi.org/10.1107/S0021889892006265

Evangelista, S. H., Lirani, J., Al-Qureshi, H. A. (2002). Implementing a modified Marciniak-Kuczynski model using the finite element method for the simulation of sheet metal deep drawing, Journal of Materials Processing Technology, 130–131, 135–144. https://doi.org/10.1016/S0924-0136(02)00729-X

Ghazanfari, A., Assempuor, A., Habibi, M., Hashemi, R. (2016). Investigation on the effective range of the through thickness shear stress on forming limit diagram using a modified Marciniak – Kuczynski model, 16(1), 137–143.

Habibi, M., Ghazanfari, A., Assempour, A., Naghdabadi, R., and Hashemi, R. (2017). Determination of Forming Limit Diagram Using Two Modified Finite Element Models, 48(4), 379–388.

Habibi, M., Ghazanfari, A., Assempour, A., Naghdabadi, R., Hashemi, R. (2017). Determination of Forming Limit Diagram Using Two Modified Finite Element Models, Asjr-Me, 48(4), 141–143.

Hashemi, R., Ghazanfari, A., Abrinia, K., Assempour, A. (2012). Forming limit diagrams of ground St14 steel sheets with different thicknesses, SAE International Journal of Materials and Manufacturing, 5(2012-01–0018), 60–64. https://doi.org/10.4271/2012-01-0018

International standard ISO 12004-2 metalic materials sheet and strip determination of forming limit curves. (2008). Geneva, Swizerland: International organization for standardization.

Marciniak, Z., and Kuczyński, K. (1967). Limit strains in the processes of stretch-forming sheet metal, International Journal of Mechanical Sciences, 9(9), 609–620. https://doi.org/10.1016/0020-7403(67)90066-5

Mesbah, M., Fadaeifard, F., Karimzadeh, A., Nasiri-Tabrizi, B., Rafieerad, A., Faraji, G., Bushroa, A. R. (2016). Nano-mechanical properties and microstructure of UFG brass tubes processed by parallel tubular channel angular pressing, Metals and Materials International,

22(6), 1098–1107. https://doi.org/10.1007/s12540-016-6152-0

Mianroodi, M., Altmeyer, G., Touchal, S. (2019). Experimental and numerical FEM-based determinations of forming limit diagrams of St14 mild steel based on Marciniak-Kuczynski model, Journal of Mechanical Engineering and Sciences, 13(4), 5818–5831. https://doi.org/10.15282/jmes.13.4.2019.08.0464

Nguyen, V. T., Kwon, S. J., Kwon, O. H., and Kim, Y. S. (2017). Mechanical Properties Identification of Sheet Metals by 2D-Digital Image Correlation Method, Procedia Engineering, 184(Dic), 381–389. https://doi.org/10.1016/j.proeng.2017.04.108

Parks, V. J. (1982). Strain Measurement Using Grids, Optical Engineering, 21(4), 633–639. https://doi.org/10.1117/12.7972958

Peters, W. H., Ranson, W. F. (1982). Digital imaging techniques in experimental stress analysis, Optical Engineering, 21(3), 213427.

Rahmatabadi, D, Shahmirzaloo, A., Hashemi, R., and Farahani, M. (2019). Using digital image correlation for characterizing the elastic and plastic parameters of ultrafine-grained Al 1050 strips fabricated via accumulative roll bonding process, Materials Research Express, 6(8), 086542. https://doi.org/10.1088/2053-1591/ab18c3

Rahmatabadi, Davood, and Hashemi, R. (2017). Experimental investigation of formability of aluminum sheets produced by cold roll bonding process used by Nakazima test, Modares Mechanical Engineering, 17(3), 451–454. Retrieved from https://mme.modares.ac.ir/article-15-11509-en.html

Rahmatabadi, Davood, Tayyebi, M., Sheikhi, A., Hashemi, R. (2018). Fracture toughness investigation of Al1050/Cu/MgAZ31ZB multi-layered composite produced by accumulative roll bonding process, Materials Science and Engineering A, 734(August), 427–436. https://doi.org/10.1016/j.msea.2018.08.017

St-14 Robert Company datasheet, (2008)., 1–2.

Zwick. (2018). Materials testing Product Information Horizontally oriented cruciform testing machine with electro- mechanical testing actuators for tests up to 2 kN Zwick Materials testing Product Information Horizontally oriented cruciform testing machine.

https://www.zwick.com/en/biaxial-testing-machines/cruciform-testing-machine

Chapter 6

General conclusion

This thesis deals with the numerical and experimental investigation of strain localization and the determination of Forming Limit Diagram (FLD).

Forming limit diagram for BCC and FCC materials are drawn using both numerical and experimental procedures.

In order to numerically predict localized necking, two approaches have been used. The first one is based on the Marciniak-Kuczynski (M-K) model implemented in a FEM modeling of biaxial test including an initial band with reduced thickness.

The results show that the formability of sheet metal is increased by increasing the value of the initial thickness ratio, f_0. The formability of sheet metals is changed by changing the orientation bands θ. In this study, the orientation band changes from 0° to 40°. By increasing the value of θ the formability of sheet metal is decreased.

CPFEM simulations for the M-K biaxial traction test were performed. An UMAT subroutine was developed and implemented in the commercial code Abaqus. The crystal plasticity Taylor model is used for its simplicity. The texture evolution for BCC and FCC crystallographic structures are analyzed in the safe zone as well as in the defect zone for different strain path. We show that the texture evolution did not have a strong effect on formability and FLD.

The second numerical approach is based on a FEM simulation of the Nakajima test.

In this thesis, several experimental tests were conducted in order to validate the predicted numerical results. Thus, the biaxial test for flat sheet for BCC materials and the Nakajima test for FCC (Aluminum Al6106) and BCC (St14 mild steel) is done. The DIC technique is used for strain measurement. The development of crystallographic texture evolution during the tests is captured thanks to the XRD technique.

A relative good correlation between the numerical and experimental tests for FCC and BCC materials is obtained.

The industrial and scientific perspectives of this study are :

- Produce new material by accumulative roll bonding (ARB) of Al6061 and St-14 mild steel.
- Obtaining the new metal forming limit diagram by Nakazima experimental test.
- Optimization of punching force to prevent tearing and wrinkling of metal sheets.
- Texture evolution for Nakajima numerical simulation.
- Using other polycrystalline plasticity models to obtain crystallographic textures (φ model).